

University of Nottingham
UK | CHINA | MALAYSIA

Molecular Spectroscopy of Nano- and Bio-Systems Using Quantum Chemistry

Aleksandra Foerster
Supervisors: Prof. Elena Besley and Prof. Nicholas Besley

September 2023

This thesis is submitted for the degree of
Doctor of Philosophy.

Abstract

Computational molecular spectroscopy, as a sub-field of quantum chemistry, allows one to obtain a comprehensive picture of investigated molecules and systems in terms of their structure and properties. It not only helps in the interpretation and understanding of the experimental spectra or predicting spectroscopic properties of molecular systems but can also be a great tool in the development of new materials. Various theoretical and computational methods have been successfully applied to solve different problems in many branches of science, however applying them to the investigation of larger and more complex systems remains a challenge. This work focuses on using Density Functional Theory (DFT) and Time-Dependent Density Functional Theory (TDDFT) methods to investigate the quantum chemical and spectroscopic properties of larger-sized systems. Four different types of molecules were studied, quantum dot (QD) clusters, endohedral fullerenes with an encapsulated metal atom, endohedral fullerenes with diatomic molecules, and the secondary structures of proteins. Methods to accurately and efficiently simulate X-ray and UV-Vis spectroscopy to reproduce experimental data and provide insights into the underlying chemical and physical processes associated with these techniques and the systems studied are provided.

Using quantum chemical calculations, it has been possible to gain more understanding of the photophysical process underpinning the operation of QD-based fluorescent probes, and to support the design of QD-based optical sensors for the detection of biomolecules. Theoretical methods have been also successfully applied to achieve a better picture of super atomic molecular or-

bitals (SAMOs) within the endohedral fullerenes and to provide insights into the potential for design of novel advanced materials for molecular electronics. The non-resonant X-ray emission spectroscopy of amino acids and a dipeptide have been studied using TDDFT calculations at the nitrogen and oxygen K-edges. Calculations for the model α-helix and β-sheet structures showed the spectra to be relatively insensitive to the structure of peptide bond, with the greatest variation observed at the oxygen K-edge. Combining TDDFT with Franck–Condon simulations has allowed to simulate vibrationally resolved X-ray absorption spectra of nitrogen encapsulated within C_{60} ($N_2@C_{60}$). The studies have showed sensitivity of the spectra and spectroscopic properties of N_2 to the presence of the C_{60} cage.

Contents

Abstract i

Acknowledgements vii

List of Publications ix

List of Tables xi

List of Figures xv

List of Abbreviations xxi

1 Introduction 1

1.1 Overview of Molecular Spectroscopy 1

1.1.1 UV-Vis Spectroscopy 5

1.1.2 X-Ray Absorption Spectroscopy 8

1.1.3 X-Ray Emission Spectroscopy 11

1.2 Overview of Computational Methods 12

1.2.1 Concepts of Quantum Mechanics in Chemistry 12

1.2.2 The Born–Oppenheimer Approximation 15

1.2.3 Self-Consistent-Field Hartree–Fock Theory 16

1.2.4 Density Functional Theory 24

1.2.5 Time-Dependent Density Functional Theory 29

1.2.6 Maximum Overlap Method (MOM) 32

1.2.7 Vibrationally Resolved Electronic Spectra 33

2 Design of QDs for Sensing Applications 37

2.1 Introduction . . . 37
2.2 Computational Methods . . . 40
2.3 Characterisation of QDs and Dopamine . . . 45
2.3.1 Dopamine Characterisation . . . 45
2.3.2 QD Characterisation . . . 46
2.3.3 Dopamine Attachment to QDs . . . 49
2.4 QD-Based Fluorescent Probes . . . 51
2.4.1 Molecular Orbital Energy Analysis . . . 51
2.4.2 Analysis Based on Excited States of QD-Dopamine Systems . . . 53
2.5 Solvent Inclusion . . . 56
2.6 Conclusion . . . 58

3 Super Atomic Molecular Orbitals of Endohedral Fullerenes 63
3.1 Introduction . . . 63
3.2 Evaluation of Computational Methods . . . 66
3.3 Characterisation of $Li@C_{60}$ and $Ca@C_{60}$ . . . 70
3.4 Effect of Hydrogenation on Endohedral C_{60} . . . 75
3.5 SAMO States of Endohedral Fullerenes Calculated using TDDFT 79
3.6 Conclusion . . . 82

4 Vibrationally Resolved Spectra for N_2 and $N_2@C_{60}$ 85
4.1 Introduction . . . 85
4.2 Computational Methods . . . 87
4.2.1 Electronic Calculations . . . 87
4.2.2 Calculation of the Vibronic Spectra . . . 88
4.3 Characterisation of N_2 . . . 88
4.3.1 Evaluation of Computational Methods . . . 88
4.3.2 Bond Length and Vibrational Frequency of N_2 . . . 90
4.4 Vibrationally Resolved XAS of N_2 . . . 94
4.5 Characterisation of $N_2@C_{60}$ . . . 95

4.6 Vibrationally Resolved XAS of $N_2@C_{60}$ 100
4.7 Conclusion 103

5 TD-DFT study of the XES of amino acids and proteins 107
5.1 Introduction 107
5.2 Computational Methods 109
5.3 XES of Amino Acids 112
5.4 XES of Di-Amino Acids 121
5.5 XES of Proteins 124
5.6 Conclusions 127

6 Conclusions 131

Acknowledgements

I would like to thank my two exceptional supervisors, Nick Besley and Elena Besley for giving me the opportunity of working with them and their enormous support during the time of this PhD. There are no words to describe how grateful I am, for everything.

I would also like to express my deepest gratitude to Bang for his invaluable help, sharing his extensive knowledge, offering advices, and showing endless patience. I am grateful beyond the words.

Furthermore, I would like to thank all the members of comp-chem group for great times, interesting discussions, laughing, dancing, and making this experience even more enjoyable. You are all extraordinary. Thank you.

List of Publications

1. "Quantum Chemical Characterization and Design of Quantum Dots for Sensing Applications" Foerster, A.; Besley, N. A. *J. Phys. Chem. A* **2022**, 126, 19, 2899-2908 [**Chapter 2**]

2. "Time-dependent density functional theory study of the X-ray emission spectroscopy of amino acids and proteins" Foerster, A.; Besley, N. A. *J. Chem. Phys. Lett.* **2020**, 757, 137860 [**Chapter 5**]

3. "Computational Evidence of Super Atomic Molecular Orbitals in Endohedral Fullerenes", Foerster, A.; Huynh, B.; Stace A.; Besley E. (manuscript in preparation, **2023**) [**Chapter 3**]

4. "Vibrationally Resilved Spectra for N_2 and N_2C_{60}" Foerster, A.; Huynh, B.; Fields, C.; Kiraly, B.; Besley E.; Moriarty P. (manuscript in preparation, **2023**) [**Chapter 4**]

List of Tables

2.1 Lowest four singlet transition energies for $C_{35}H_{36}$, $Si_{35}H_{36}$, and $Ge_{35}H_{36}$ quantum dots calculated using TDDFT/CAM-B3LYP with a range of basis sets. 42

2.2 Computed lowest four singlet transition energies for $C_{35}H_{36}$, $Si_{35}H_{36}$, and $Ge_{35}H_{36}$ for a range of computational methods, using the TDA approach. 43

2.3 Calculated transition energies for the lowest four singlet states for functionalised $X_{35}H_{36}$ QDs with attached oxidised and reduced forms of dopamine for a range of computational methods. 44

2.4 Calculated transition energies for the lowest 10 singlet states for oxidised and reduced forms of dopamine with and without the linking group using TDDFT and TDDFT/TDA methods 47

2.5 HOMO-LUMO gap, the excitation energy for the lowest singlet state, and excitation energy for the most intense transition calculated using TDDFT CAM-B3LYP with SRLC basis set for Si- and Ge-based QDs and 6-31+G* basis set for C-containing QDs. 48

2.6 Calculated energies for functionalised $X_{35}H_{36}$ QDs with attached oxidised and reduced forms of dopamine using DFT and 6-31G, 6-31G*, and def2-SVP basis sets level of theory. 51

2.7 Binding energies (in Hartree) in a dopamine functionalised $Ge_{84}H_{64}$ QD, calculated at B3LYP/def2-SVP level of theory. 52

2.8 Transition energies and assignments for the dopamine functionalised $Ge_{84}H_{64}$ QD calculated at CAM-B3LYP/SRLC level of theory. 55

2.9 Transition energies and assignments for the dopamine functionalised $Ge_{84}H_{64}$ QD with the PCM solvent model calculated at CAM-B3LYP/SRLC level of theory. 59

3.1 The HOMO-LUMO and LUMO-SAMO gaps and total energies for C_{60} calculated using various functionals and basis sets. . . . 69

3.2 Bond length and the distance of the encapsulated atom from a cage for studied fullerenes. 71

3.3 HOMO-LUMO and LUMO-SAMO gaps for C_{60}, $Ca@C_{60}$ and $Li@C_{60}$. 73

3.4 HOMO-LUMO and LUMO-SAMO gaps for $C_{60}H_{60}$, $Ca@C_{60}H_{60}$ and $Li@C_{60}H_{60}$. 78

3.5 Lowdin charges calculated for the HOMO in hydrogenated and non-hydrogenated $Li@C_{60}$ and $Ca@C_{60}$. 78

3.6 Transition energies, assignments, and oscillator strength (f) for the pure and hydrogenated C_{60}, $Li@C_{60}$, and $Ca@C_{60}$ calculated using TDDFT/B3LYP/6-31++G** 80

4.1 Energy transitions and corresponding oscillator strengths for N_2 using five different functionals (B3LYP, CAM-B3LYP, PBE0, SCR1R1, BLYP) and three different basis sets (6-31G, 6-31++G**), 6-311(2+,2+)G**. 89

4.2 Comparison of bond lengths in the optimized ground and excited states of N_2 calculated using DFT with different functionals and basis sets. 92

4.3 Comparison of vibrational frequencies (cm^{-1}) in the optimized ground and excited states of N_2 calculated using DFT with different functionals and basis sets. 93

4.4 Calculated energies for the vibrational transitions of N_2 using various functionals and basis sets. 96

4.5 Transition energies, assignments and oscillator strength for the N_2 and $N_2@C_{60}$ calculated at the B3LYP/ 6-31++G** for N and 6-31G for C level of theory. 97

4.6 The bond length, frequency, and force constant of $N_2@C_{60}$ and N_2 in the ground and excited states predicted using B3LYP/6-31++G** level of theory. 99

4.7 Vibrational transitions in $N_2@C_{60}$ and corresponding energies calculated using the parallel normal modes approximation. . . . 102

List of Figures

1.1 Vibrational levels of a diatomic molecule in a Morse potential well. 3

1.2 Examples of electronic transitions. 5

1.3 Jablonski diagram showing the excitation of a molecule to its singlet excited state and relaxing to the ground state via different mechanisms. 7

1.4 X-ray absorption edge spectrum defining various energy regions 9

1.5 Schematic of transitions involved in XAS and XES 11

2.1 Structures for QDs with various sizes. 41

2.2 Absorption spectra for oxidised and reduced form of dopamine with the linking group, and the orbitals associated with the lowest energy transitions. 45

2.3 The oxidised and reduced forms of dopamine with and without the linking group and corresponding absorption spectra. 46

2.4 Molecular orbitals associated with intense transitions for $X_{84}H_{64}$ QDs. 50

2.5 The $X_{84}H_{64}$ system with atom coloured based on their symmetry-equivalent groups. 51

2.6 Schematic of the PET mechanism 52

2.7 Molecular orbital diagrams based upon ground state CAM-B3LYP/SRLC calculations for the $Ge_{84}H_{64}$ and $Si_{165}H_{100}$ QDs and the reduced and oxidised forms of dopamine. 54

2.8 Optimised structures of the two forms of dopamine on a $Ge_{84}H_{64}$ QD and computed CAM-B3LYP/SRLC spectra for $Ge_{84}H_{64}$-DOPred (red line) and $Ge_{84}H_{64}$-DOPox (black line). 56

2.9 Molecular orbitals involved in the transition for functionalised $Ge_{84}H_{64}$-DOP in vacuum. 57

2.10 Molecular orbitals involved in the transition for functionalised $Ge_{84}H_{64}$ in solvent. 60

3.1 Optimised structures of C_{60} with and without Ca and Li atoms inside the cage, compared with hydrogenated C_{60} with and without Ca and Li atoms, calculated using B3LYP/6-31++G** level of theory. 70

3.2 Molecular orbitals for C_{60} calculated using the B3LYP/6-31++G** level of theory. 73

3.3 Molecular orbitals for $Ca@C_{60}$ calculated using the B3LYP/6-31++G** level of theory. 74

3.4 Molecular orbitals for $Li@C_{60}$ calculated using the B3LYP/6-31++G** level of theory. 74

3.5 Molecular orbitals for $C_{60}H_{60}$ calculated using the B3LYP/6-31++G** level of theory. 76

3.6 Molecular orbitals for $Li@C_{60}H_{60}$ calculated using the B3LYP/6-31++G** level of theory. 77

3.7 Molecular orbitals for $Ca@C_{60}H_{60}$ calculated using the B3LYP/6-31++G** level of theory. 77

3.8 Molecular orbitals associated with the intense transition for $Li@C_{60}H_{60}$. 81

3.9 Molecular orbitals associated with the intense transition for $Ca@C_{60}H_{60}$. 82

4.1 Vibrationally resolved N 1*s* XAS of N_2 simulated using TDDFT with B3LYP (a), CAM-B3LYP (b), PBE0 (c), and BLYP (d) and different basis sets. 94

4.2 Optimised ground state structure of $N_2@C_{60}$ using the B3LYP/6-31++G** level of theory. 97

4.3 MO diagram and 3D visualization of the ground-state and excited-state MOs involved in the transition corresponding to the first excited state for N_2 and $N_2@C_{60}$. 98

4.4 Vibrationally resolved N 1*s* XAS of $N_2@C_{60}$ simulated using TDDFT with the B3LYP functional and various basis sets. . . . 101

4.5 Vibrationally resolved N 1*s* XAS of N_2 and $N_2@C_{60}$ simulated using TDDFT with the B3LYP functional and 6-31++G** basis set. 103

4.6 Vibrationally resolved N 1s XAS of $N_2@C_{60}$ simulated using TDDFT with the B3LYP functional and 6-31++G** basis set, compared to experimental results. 104

5.1 Calculated non-resonant X-ray emission spectra of the zwitterionic form of glycine at the nitrogen K-edge (left) and oxygen K-edge (right). 113

5.2 Calculated non-resonant X-ray emission spectra of the neutral form of glycine at the nitrogen K-edge (left) and oxygen K-edge (right). 114

5.3 Calculated TDDFT/CAM-B3LYP non-resonant X-ray emission spectra of the zwitterionic forms of (a) proline, (b) cysteine, (c) alanine and (d) glycine at the nitrogen K-edge (left) and oxygen K-edge (right). 116

5.4 Experimental and calculated TDDFT/CAM-B3LYP non-resonant X-ray emission spectra for the zwitterionic forms of (a) nitrogen K-edge glycine, (b) oxygen K-edge glycine, (c) nitrogen K-edge proline and (d) oxygen K-edge proline. 118

5.5 Molecular orbitals associated with the observed bands in the nitrogen K-edge X-ray emission spectrum of the zwitterionic form of glycine calculated using TDDFT/CAM-B3LYP level of theory. 119

5.6 Molecular orbitals associated with the observed bands in the oxygen K-edge X-ray emission spectrum of the zwitterionic form of glycine calculated using TDDFT/CAM-B3LYP level of theory. 119

5.7 Molecular orbitals associated with the observed bands in the nitrogen K-edge X-ray emission spectrum of the zwitterionic form of proline calculated using TDDFT/CAM-B3LYP level of theory. 120

5.8 Molecular orbitals associated with the observed bands in the oxygen K-edge X-ray emission spectrum of the zwitterionic form of proline calculated using TDDFT/CAM-B3LYP level of theory. 120

5.9 Experimental and non-resonant X-ray emission spectra of the zwitterionic form diglycine calculated using TDDFT/CAM-B3LYP level of theory. 122

5.10 Molecular orbitals associated with the observed bands in the nitrogen K-edge X-ray emission spectrum of the zwitterionic form of di-glycine calculated using TDDFT/CAM-B3LYP level of theory. 123

5.11 Molecular orbitals associated with the observed bands in the oxygen K-edge X-ray emission spectrum of the zwitterionic form of di-glycine calculated using TDDFT/CAM-B3LYP level of theory. 123

5.12 Calculated non-resonant X-ray emission spectra for a model α-helix at the (a) nitrogen K-edge and (b) oxygen K-edge. 124

5.13 Calculated non-resonant X-ray emission spectra for a β-sheet at the (a) nitrogen K-edge and (b) oxygen K-edge. 125

5.14 Calculated nitrogen K-edge spectra for the initial core-hole located at different nitrogen atoms for the α-helix. 126

5.15 Calculated oxygen K-edge spectra for the initial core-hole located at different oxygen atoms for the α-helix. 126

5.16 Calculated nitrogen K-edge spectra for the initial core-hole located at different nitrogen atoms for the β-sheet. 127

5.17 Calculated oxygen K-edge spectra for the initial core-hole located at different oxygen atoms for the β-sheet. 128

5.18 Comparison of the calculated non-resonant X-ray emission spectra for the α-helix and β-sheet at the (a) nitrogen K-edge and (b) oxygen K-edge. 128

List of Abbreviations

XAS	X-ray absorption spectroscopy
XANES	X-ray absorption near edge structure
EXAFS	Extended X-ray absorption fine structure
XES	X-ray emission spectroscopy
IR	Infrared
CCSD	Coupled Cluster Singles Doubles
CI	Configuration Interaction
DFT	Density Functional Theory
ECP	Effective Core Potential
HF	Hartree–Fock
MOM	Maximum Overlap Method
LSDA	Local spin density approximation
PES	Potential energy surface
SCF	Self consistent field
HOMO	Highest Occupied Molecular Orbital
LUMO	Lowest Unoccupied Molecular Orbital
SAMO	Super Atomic Molecular Orbital
QDs	Quantum Dots
PET	Photo Electron Transfer

Chapter 1

Introduction

1.1 Overview of Molecular Spectroscopy

Molecules interact with the oscillating electric and magnetic fields of radiation. They can then absorb an amount of energy carried by the electromagnetic waves that is equivalent to the energy that allows a molecule to be promoted from one discrete energy level to another. Transitions between those discrete energy levels can be measured by molecular spectroscopy.[1] Increasing sophistication of spectroscopic techniques makes interpreting spectroscopic results (spectra) extremely difficult, if not impossible.[2] Computational molecular spectroscopy helps to elucidate information included in the spectra of molecules by using quantum mechanics. Experimental molecular spectroscopy measures transitions between the various energy states (rotational, vibrational, and electronic) of a molecule, and molecular spectra are produced as a result of those transitions. In computational molecular spectroscopy the allowed energy states of molecules can be determined by solving the Schrodinger equation.

Molecules occupy specific energy levels, and a molecule's energy is stored in different types of motion. The translational kinetic energy, electronic energy,

vibrational energy, and rotational energy contributes to the total energy of a molecule. Molecular spectroscopy is concerned only with the electronic, vibrational and rotational energy levels of a molecule. Vibrational spectra can be measured using Infrared (IR) or Raman spectroscopy.[3,4] In IR, radiation with different frequencies is passed through the sample and the intensity of transmitted light is measured, while in Raman spectroscopy, a laser beam is passed through the sample and the scattered part of light is measured. For a molecule to interact with the radiation in the IR range (780nm -1mm) and absorb the energy from it, the molecule must have a permanent or induced dipole moment which oscillates with the same frequency as the radiation. The vibrations of a molecule and the frequencies of the radiation have to be the same for the resonance energy transfer to take place. The harmonic oscillator can be used as a model for the vibration of a normal mode. However, a normal mode has an asymmetric potential and therefore Morse potential is often used to create a better representation of the potential energy surface. The Morse potential has the form

$$V = D_e \left(1 - e^{-\beta q}\right)^2, \tag{1.1}$$

where D_e is the depth of the potential well and represents the dissociation energy; β is the curvature at the bottom of the potential well, and q is vibrational coordinate. The allowed energy levels of the system are then given by

$$\bar{E}_\nu = \bar{\omega}_e \left(\nu + \frac{1}{2}\right) - \bar{\omega}_e x_e \left(\nu + \frac{1}{2}\right)^2, \tag{1.2}$$

where $\bar{\omega}_e$ is the vibrational frequency, ν is the vibrational quantum number, x_e is the first anharmonicity constant. The vibrational energy levels of the electronic ground state of diatomic molecules can be represented by horizontal lines in a Morse potential well (Figure 1.1). Using radiation of infrared frequency, molecules are promoted from one vibrational energy level to another. Depending on a molecule's electronic structure, various energy vibrational transitions can be observed. For instance, transition from lowest energy level (ground

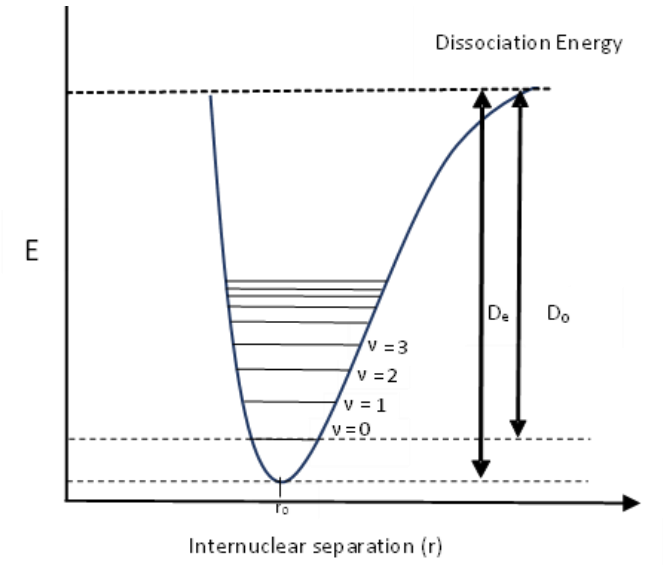


Figure 1.1: *Vibrational levels of a diatomic molecule in a Morse potential well. Where, ν is vibrational level, D_e is dissociation energy, and D_0 the true energy required for dissociation due to the zero point energy of the lowest ($\nu = 0$) vibrational level.*

state) to higher energy level (designated as $\nu = 0$ and $\nu = 1$ in Figure 1.1 respectively) can take place, and the resulting state of a molecule from this transition would be then called state 1. Diatomic molecules have only one kind of vibration (normal mode), while polyatomic molecules can have many possible vibrations as the numbers of vibrational degrees of freedom for polyatomic molecules with M atoms is given by $3M - 6$ (or $3M - 5$ for linear molecules). Therefore, to describe each vibration normal mode in a polyatomic molecule, a separate potential well with its own parameters is required.

The spacing between vibrational energy levels in the Morse potential well decreases with increasing value of ν. From the analysis of experimental spectra it is possible to calculate the anharmonic force constant of the vibrational normal mode, and the dissociation energy of a molecule for diatomic molecule. Vibrational spectroscopy is a valuable tool for finding out information about the presence or absence of specific functional groups in a sample. Also, by analyzing the infrared (IR) molecular fingerprint, one can effectively identify different substances.[5] It is a useful technique for polar molecules.[6–8]

Much more energetic radiations, like UV-Visible light (100 to 780 nm wavelength), and X-ray radiation (0.01 to 10 nm wavelength) can promote transitions between a molecule's electronic states of different quantum numbers.[9–11] When this happens, the molecule is excited from the ground state to the higher excited states, and the vibrational and rotational transitions can also be simultaneously involved. In the previously described vibrational spectroscopy, the transitions between vibrational energy levels take place within a single electronic potential well. In electronic spectroscopy, transitions of molecules take place between different electronic potential wells (Figure 1.2). During the interaction of molecular system with radiation, a transition from vibrational state, ν_0 in the electronic ground state to the vibrational state ν_0' in the electronic excited state can occur. This transition involves no quanta of vibrational energy. Another possible transition could be from ν_0 to ν_1' (represented by the dashed arrow in Figure 1.2) which involves one quantum of electronic energy and one quantum of vibrational energy.

In molecular orbital (MO) theory, electronic transitions occur when electrons are promoted from orbitals of lower energy to orbitals of higher energy. MO theory provides a framework for understanding these transitions and predicting their effects on molecular properties. To measure the transitions between electronic states in a molecule, electronic spectroscopy is used. When the electrons are removed from the valence orbitals the Photoelectron spectroscopy (PES) technique is used, while when the electron are removed from core orbitals X-ray photoelectron spectroscopy can be used.[12,13] For exciting electrons from valence orbitals into virtual unoccupied orbitals and studying the resulting transitions, UV-Vis spectroscopy or fluorescence spectroscopy (emission) are used.[14] Exciting electrons from core orbitals into virtual unoccupied orbitals is facilitated by X-ray absorption spectroscopy (XAS) or near edge X-ray absorption spectroscopy (NEXAS). Electronic spectroscopy helps to determine the binding energy, HOMO-LUMO gap and structure of molecules.[15,16] X-ray

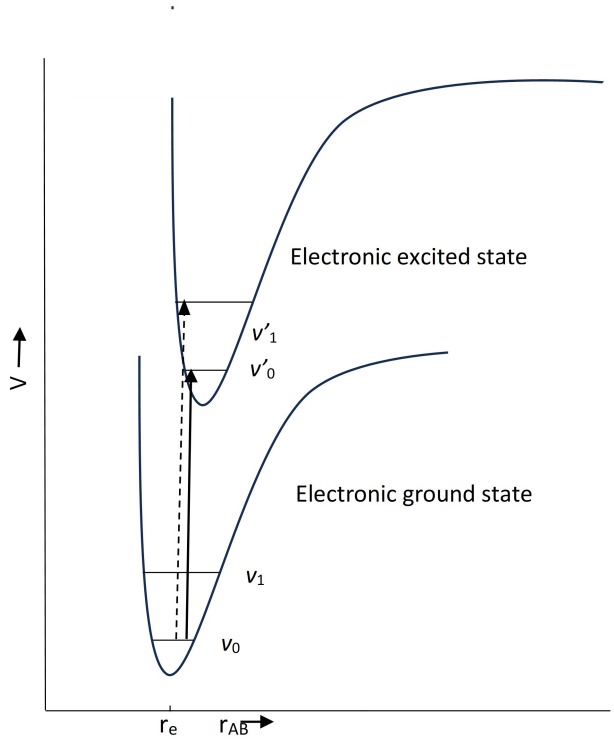


Figure 1.2: *Examples of electronic transitions. The 0-0 transition is represented by a vertical arrow, 0-1 transition is represented by the dashed arrow.*

based electronic spectroscopy provides information on the oxidation state of elements and chemical bonding.[17,18] Some of the spectroscopic techniques and detailed description of computational methods and quantum chemistry used for molecular spectroscopy are described in following subchapters.

1.1.1 UV-Vis Spectroscopy

UV-Vis spectroscopy studies the interaction of matter with radiation of a wavelength between approximately 200 – 780 nm.[19] In this energy range, the photon of radiation is absorbed by electrons located in highest occupied molecular orbitals of an atom and transferred to virtual orbitals. Following the excitation of a molecule, various processes occur within its electronic structure which are well represented by the Jablonski diagram (Figure 1.3). One of these paths involve the return of a molecule to its ground state accompanied by the

emission of light and can be further distinguished into fluorescence and phosphorescence. In fluorescence an excited molecule transfers from a higher to a lower level with the emission of a photon, without changing the multiplicity in a transition which is allowed by the selection rule. If the time between the absorption of energy and its emission is much longer than 10^{-8} seconds, the radiation process is called phosphorescence. Phosphorescence occurs when an excited molecule transfers from a higher to a lower level with the emission of a photon and a change in multiplicity. Occupancy of the triplet level (of a different multiplicity) directly from the ground state is prohibited. Therefore, the molecule is usually excited to the first singlet state (S_1) and from there, under certain conditions, it can transfer to the triplet state (T_1). Because the transition between the T_1 and S_0 states is prohibited (different multiplicity), the molecule remains in the excited electronic state for a relatively long time before emitting a photon and returning to the electronic ground state. Apart from fluorescence and phosphorescence, there are other possible pathways via which excited molecules return to their lower energy states. The first one, Internal conversion (IC) involves a molecule undergoing a permitted transition from excited states to states occurring without changing the multiplicity, for example, type $S_2 \rightarrow S_1$ or $T_2 \rightarrow T_1$. Intersystem Crossing (IC) path where the radiationless crossing between singlet and triplet states takes place. This process is forbidden because it involves change of multiplicity; for example, type $S_1 \rightarrow T_1$ or $T_1 \rightarrow S_0$ (Figure 1.3).

For an absorption to occur, the transition must meet some rules known as selection rules.[20] For electron absorption spectroscopy they are as follows:

1. The radiation energy must be matched to the difference between energy levels of a molecule between which the transition takes place,

$$\Delta E = h\nu \tag{1.3}$$

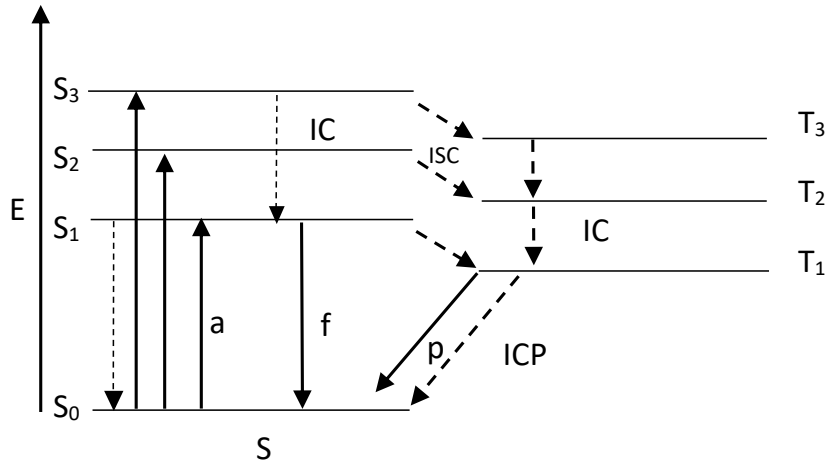


Figure 1.3: *Jablonski diagram showing the excitation of a molecule to its singlet excited state and relaxing to the ground state via different mechanisms. IC – internal conversion, ISC – intersystem crossing, a –radiation absorption, f – fluorescence, p – phosphorescence.*

where h is the Planck's constant and ν is radiation frequency.

2. The transition probability space, W between the initial ψ_i and the excited state ψ_f must be non-zero. This requires the following condition to be met:

$$W = B_{\mathrm{f}\leftarrow\mathrm{i}}\rho \neq 0 \tag{1.4}$$

where ρ is radiation density and $B_{\mathrm{f}\leftarrow\mathrm{i}}$ is Einstein's coefficient:

$$B_{\mathrm{f}\leftarrow\mathrm{i}} = \frac{8\pi^3}{3h^2}\left|\boldsymbol{\mu}_{\mathrm{f}\leftarrow\mathrm{i}}\right|^2 \tag{1.5}$$

Here $\boldsymbol{\mu}_{\mathrm{f}\leftarrow\mathrm{i}}$ is a transition dipole moment, $\boldsymbol{\mu}_{\mathrm{f}\leftarrow\mathrm{i}} = \langle\psi_f|\hat{\boldsymbol{\mu}}|\psi_i\rangle$, where $\hat{\boldsymbol{\mu}}_{\mathrm{f}\leftarrow\mathrm{i}}$ is the electric dipole moment operator of a molecule that undergoes absorption. Therefore, for a transition to occur, where $\rho \neq 0$, the dipole moment of the transition must be non-zero. Since $\boldsymbol{\mu}_{\mathrm{f}\leftarrow\mathrm{i}}$ is a vector quantity, it is sufficient that at least one of its components is non-zero for the transition to be allowed. The orbital is designated g (for *gerade*, even) if the phase is the same, and u (for *ungerade*, odd) if the phase changes sign. Based on group theory, there is a Laporte's rule which states that for a centrosymmetric molecule, transitions

must occur between states of different parities under inversion ($u \leftarrow g$ and $g \leftarrow u$) are allowed, while those between states of the same parities ($g \leftarrow g$ and $u \leftarrow u$) are forbidden.

3. Transitions between electronic states with the same multiplicity are allowed, *e.g.* singlet-singlet ($\Delta S = 0$), while transitions between states of different multiplicity are prohibited.

1.1.2 X-Ray Absorption Spectroscopy

X-ray absorption spectroscopy (XAS) uses X-rays, in the range of about 100 eV to 500 keV, typically from synchrotron light sources to investigate sample properties.[21–23] In this energy range, the photon of radiation is absorbed by the core level electrons of an atom and can be excited to un unoccupied stated near the ionisation threshold or ionised to the continuum. Figure 1.4 shows a typical X-ray absorption spectrum where depending on the region of the spectrum, different information can be obtained about the studied chemical system. The 'pre-edge region' where core electron are excited to a higher unoccupied orbital can provide information on the excited electronic state and the local symmetry of the atom. In the edge region, where the photon energy is between the ionisation energy (E_i) and $E_i + 10\,\text{eV}$ 'X-ray absorption near edge structure' (XANES)[24] is observed which provides information about the oxidation state of the atom and its coordination surrounding. The region between $E_i + 10\,\text{eV}$ and $E_i + 50\,\text{eV}$ is called 'near edge X-ray absorption fine structure' (NEXAFS), from which the bond distances and information about the orientation of the molecules adsorbed on the substrate can be obtained. The region lying at the energy grater than $E_i + 50\,\text{eV}$ which is called 'extended X-ray absorption fine structure' (EXAFS)[25] allows to gain information about the number of coordinating atoms and the species of atoms surrounding the atom which is interacting with the X-ray radiation. The combination of XANES and EXAFS

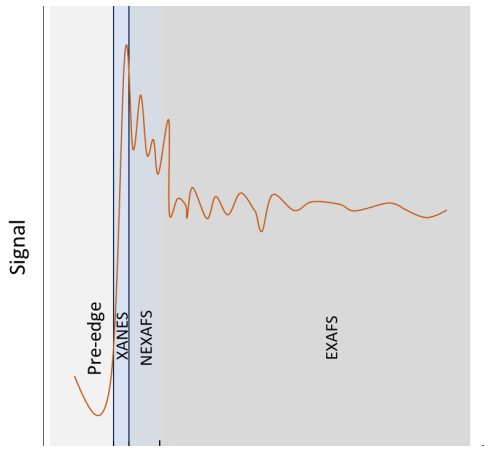


Figure 1.4: *X-ray absorption edge spectrum defining various energy regions*

techniques is called 'X-ray absorption fine structure' (XAFS).[26] Techniques based on the absorption of X-rays can be used for the study of both crystalline and amorphous compounds.[27] The main advantages of the techniques are: high selectivity due to the type of element tested; sensitivity (between 10 and 100 particles per mole); and relatively short measurement time (recording the experimental spectrum takes from milliseconds up to tens of minutes).[28]

The probability that a core electron will absorb an incident X-ray via the photoelectron effect is governed by the Bouguer-Lambert's Law:

$$I = I_0 e^{-\mu t} \tag{1.6}$$

where μ is the absorption coefficient, which determines the probability of the incident X-rays absorption, I_0 is the intensity of the X-ray, I is the intensity of transmitted light through the sample, and t is the thickness of the sample. In the XAS method, the change in the absorption coefficient μ as a function of energy E is examined and the absorption coefficient can be estimated by

$$\mu \approx \frac{\rho Z^4}{AE^3}, \tag{1.7}$$

where ρ is the sample density, Z the atomic number, A the atomic mass, and E the X-ray energy. The absorption coefficient μ of a particular atom will change

with the presence of neighbouring atoms. The study of the local surrounding of the given atom is possible by adjusting the energy of X-rays to a given absorption edge, which makes X-ray spectroscopy highly atom selective. In these cases, when the X-ray has an energy corresponding to the binding energy of core electron, there will be a rapid increase (a spike) in the absorption edge. As mentioned above, XANES and EXAFS look at the energy dependence on μ just before and just after the absorption edge respectively.[29] The names of the absorption edges are analogous to the names of the atomic shells and are labelled with respect to the angular momentum of the absorbing core orbital. The K-edge corresponds to absorption from the s-shell; L-edge to p-shell and the M-edge to the d-shell. In this work all core hole spectroscopy will be considered at the K-edge.

The lifetime of the excited electron is only few femtoseconds, after which the core-hole decay process begins. There are two different mechanisms by which the core-hole decay can take place. The first mechanism is X-ray fluorescence, where electrons from the orbitals higher in energy than the core hole orbital collapse, and as a result an X-ray of exact energy is emitted. The second mechanism is the Auger decay de-excitation process where a second electron is ejected as a result of an electron falling from a higher orbital to the core hole. The absorption coefficient can either be measured by transmission:

$$\mu\left(E\right) = \ln\left(\frac{I_0}{I}\right), \tag{1.8}$$

or by de-excitation (Auger and fluorescence):

$$\mu\left(E\right) \propto \frac{I_\mathrm{f}}{I_0}, \tag{1.9}$$

where I_f is the measured fluorescence or intensity of electron emission after absorption of the X-ray radiation.

1.1.3 X-Ray Emission Spectroscopy

X-ray absorption, as described above is used to study the unoccupied orbitals, whereas X-ray emission spectroscopy (XES), probes the occupied orbitals (Figure 1.4). Similar to XAS, XES first requires the creation of an excited state

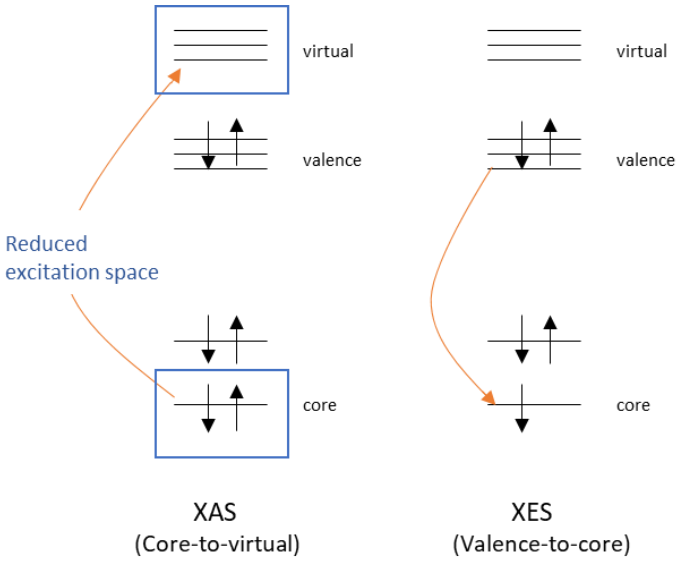


Figure 1.5: *Schematic of transitions involved in XAS and XES*

through the interaction of a photon with a core electron, but then it measures the photons that are emitted when the core hole decays via fluorescence. Depending on the choice of excitation energy, the XES technique can be split into two different categories; non-resonant and resonant XES. Non-resonant X-ray emission spectroscopy involves using energy sufficient to completely remove the core electron to the continuum. On the other hand, resonant excitation involves using an excitation energy corresponding to an absorption resonance, which promotes the electron to a bound state. XES has found applications in studying the structure of liquids, transition metal complexes, metal-ligands complexes, and the adsorption of molecules on surfaces.[30–32] XES can also be a good complementary technique to XAS, which together can provide an extended picture of the studied system.[33]

1.2 Overview of Computational Methods

Computational molecular spectroscopy investigates electronic transitions in molecules, provides useful information about the systems and helps to interpret experimental data. As spectroscopy probes the core, bonding, and non-bonding orbitals of molecular systems and materials, they must be treated quantum mechanically rather than classically, in computational simulations. This section introduces the principles of quantum mechanics and their application to chemistry, followed by an overview of the quantum chemical techniques used in this work.

1.2.1 Concepts of Quantum Mechanics in Chemistry

Light can be described as both particles and waves. When describing light as particles, they are referred to as photons, which have an energy of $E = h\nu$, where h is Planck's constant, and ν is the frequency of the photon. This quantization of energy together with the quantization of molecular energy levels in molecules forms the basis of the spectroscopic techniques used in chemistry. Electrons themselves also have wave-like nature, which is observed in molecules through the superposition of atomic orbitals to form molecular orbitals. As introduced by de Broglie[34] both light and matter behave as both particles and waves, this is known as 'wave-particle duality', and this can be expressed as

$$\lambda = \frac{h}{p} \tag{1.10}$$

where λ is the wavelength, p the momentum, and $h = 6.626 \times 10^{-34}$ Js is Planck's constant. The wave nature of matter is quantitatively expressed via a wavefunction which can be described using quantum mechanics. Quantum mechanics is an important theory that underpins our understanding of chemistry and is based upon three postulates. The first postulate asserts that a

system is described by a wavefunction ψ, which contains all information about the system. The wavefunction is a mathematical function that describes the quantum state of a particle or a system of particles at all points in space. The acceptable wavefunctions should be single valued, finite everywhere and normalizable by the condition

$$\int \psi^* \psi \mathrm{d}\mathbf{r} = 1. \tag{1.11}$$

The Born interpretation[35] indicates that the square modulus of a wavefunction $|\psi|^2$ gives the probability density of finding the particle at a given position. The second postulate asserts that observables are represented by operators. All observable quantities of a quantum system will have a corresponding quantum mechanical operator. And the third postulate asserts that the values that arise from a physical measurement correspond to the eigenvalues ω of the corresponding operator according to

$$\hat{\Omega}\psi = \omega\psi, \tag{1.12}$$

where $\hat{\Omega}$ represents an operator, ψ a wavefunction, and ω an eigenvalue of the operator $\hat{\Omega}$.

The Schrödinger equation[36] is arguably the most important equation in chemistry for finding the wavefunction of a system and calculating its properties. How a quantum system, hence a system's wave function, changes with time is described by the time-dependent Schrödinger equation:

$$i\hbar\frac{\partial}{\partial t}\psi = \hat{H}\psi, \tag{1.13}$$

where i is the imaginary unit, $\hbar = \hbar/2\pi$ the reduced Planck's constant, ψ the system's wave function, $\hat{H}$ the Hamiltonian operator, and t time. The stationary states of the system can be found by solving the time-independent

Schrödinger equation:

$$\hat{H}\psi(\mathbf{r}) = E\psi(\mathbf{r}), \tag{1.14}$$

where $\mathbf{r}$ denotes the coordinates describing the system and E is the total energy of the system in state $\psi(\mathbf{r})$. The solutions to the time-independent Schrödinger equation (Eq. 1.14) for a given system provide many functions $\psi_n(\mathbf{r})$, the stationary states of the system and the corresponding energies of these states E_n. The lowest energy solution to Eq. 1.14 is recognised as the ground state, and higher energy solutions are excited states. In case that the same energy corresponds to different states, the states are said to be degenerate.

The Hamiltonian operator in Eq. 1.14 contains both kinetic energy ($\hat{T}$) and potential energy ($\hat{V}$) terms, and for atoms and molecules, it can be written as

$$\begin{aligned}\hat{H} = &-\sum_{i=1}^{N}\frac{1}{2}\nabla_i^2 - \sum_{A=1}^{M}\frac{1}{2M_A}\nabla_A^2 - \sum_{i=1}^{N}\sum_{A=1}^{M}\frac{Z_A}{r_{iA}} \\ &+\sum_{i=1}^{N}\sum_{j>i}^{N}\frac{1}{r_{ij}} + \sum_{A=1}^{M}\sum_{B>A}^{M}\frac{Z_A Z_B}{R_{AB}},\end{aligned} \tag{1.15}$$

$$\nabla = \left(\frac{\partial}{\partial_x}, \frac{\partial}{\partial_y}, \frac{\partial}{\partial_z}\right), \tag{1.16}$$

where r_{iA}, r_{ij} and R_{AB} represent the electron-nuclear, electron-electron and nuclear-nuclear distances respectively. These are the distances between particles position vectors, $r_{iA} = |\mathbf{r}_i - \mathbf{R_A}|$, and $\mathbf{R_A} = (R_{Ax}, R_{Ay}, R_{Az})$. The sums take into account the N electrons and M nuclei the system, where Z_A are the nuclear charges and M_A are the nuclear masses, and ∇^2 is the Laplace operator defined in Cartesian coordinates. The first term represents the kinetic energy operator of the electrons; the second term the kinetic energy operator of the nuclei; the third term corresponds to the Coulomb attraction between the electrons and nuclei; and the fourth term and fifth term are the repulsion of the electrons and nuclei. In this equation, relativistic effects are often neglected, as they are insignificant for lighter elements of the periodic table.

1.2.2 The Born–Oppenheimer Approximation

The Born–Oppenheimer (BO) approximation[37] assumes that electrons being much lighter than nuclei move fast enough to be assumed to adapt instantaneously to the location of the nuclei. This results in the assumption that electrons stay in one of the possible stationary states determined by the electronic function determined for fixed positions of the nuclei. The consequence of this assumption is the possibility to generate a Hamiltonian containing both electron and nuclear degrees of freedom which can be uncoupled. Using the BO approximation allows us to decouple the nuclear and electronic motions, thus enabling us to write an electronic Hamiltonian operator where terms corresponding to the kinetic energy and repulsion of the nuclei can be omitted and the motion of N electrons in the presence of M nuclear point charges can be described as

$$\hat{H}_{\text{elec}} = -\sum_{i=1}^{N} \frac{1}{2}\nabla_i^2 - \sum_{i=1}^{N}\sum_{A=1}^{M} \frac{Z_A}{r_{iA}} + \sum_{i=1}^{N}\sum_{j>i}^{N} \frac{1}{r_{ij}} \tag{1.17}$$

Thus, the electronic Schrödinger equation is

$$\hat{H}_{\text{elec}}\psi_{\text{elec}} = E_{\text{elec}}\psi_{\text{elec}} \tag{1.18}$$

where the eigenfunction ψ_{elec} is the electronic wavefunction and the eigenvalue E_{elec} is the electronic energy at $\{\mathbf{R}_A\}$ (a set of multiple nuclear positions), *i.e.*

$$E_{\text{elec}} = E_{\text{elec}}\left(\{\mathbf{R}_A\}\right), \tag{1.19}$$

and the total energy for a fixed nuclear coordinate can be obtained by adding in the nuclear repulsion term:

$$E_{\text{total}} = E_{\text{elec}}\left(\{\mathbf{R}_A\}\right) + \sum_{A=1}^{M}\sum_{B>A}^{M} \frac{Z_A Z_B}{R_{AB}}. \tag{1.20}$$

The electronic energy depends parametrically on the positions of the nuclei and varying $\{\mathbf{R}_A\}$ will give the total energy as a function of the nuclear coordinates, creating what is known as a potential energy surface (PES). The knowledge of this function and its two successive gradients in relation to geometrical parameters become crucial when studying the properties of the atomic or molecular systems in many areas of chemistry. Knowledge of the energy minima along the PES correspond to nuclear positions allow us to find stable structures of a system, whereas low energy pathways between minima can allow study of chemical reactions.

To solve the time-independent electronic Schrödinger equation more approximations have been developed. One of them, Hartree–Fock theory that includes the application to excited state wavefunctions, will be discussed in subsection (1.2.2). Even though Hartree–Fock theory is not very often applied to spectroscopy – due to its omission of electron correlation – it forms a basis for the rest of the developed and widely implemented theories, such as Kohn–Sham density functional theory (KSDFT) and time-dependent density-functional theory (TDDFT) discussed in subsections 1.2.3 and 1.2.4.

1.2.3 Self-Consistent-Field Hartree–Fock Theory

The Hartree–Fock (HF) method, based on the HF theory[38,39] is an approximate method for solving Schrödinger equations for multi-particle systems. It is the basis of most *ab initio* methods which are used to find energy and electronic structure of the ground state of a molecular systems. The HF method can be used to calculate the wavefunctions and energies for closed-shell, ground state molecular systems, where electrons of different spins, α and β are restricted to the same set of spatial orbitals. This is known as restricted HF (RHF). In the case where separate spatial orbitals for electrons with different spins are used, the method is called unrestricted HF (UHF). UHF is commonly used to study

ground states of open-shell systems, and electronically excited states.

In the HF method, each electron in the system is assigned a one-electron wave function dependent on spatial coordinates and the spin of the electron.[40] These functions are called spin orbitals $\chi(\mathbf{x})$ and can be expressed as the product of a spatial part, $\varphi\ (\mathbf{r})$ and a spin part, $\omega(s)$:

$$\chi(\mathbf{x})\ = \varphi\ (\mathbf{r})\omega(s), \tag{1.21}$$

where $\mathbf{r}$ corresponds to the spatial coordinates and s represents the spin coordinate. The spin part, $\omega(s)$, can be either α or β for spin states with $m_s = +\frac{1}{2}$ or $-\frac{1}{2}$, respectively.

Most systems of interest will have more than one electron, which will require the consideration of many one electron spin orbitals. Therefore, a possible form for the N-electron wavefunction is as a product of spin orbitals:

$$\psi^{\mathrm{HP}}(\mathbf{x}_1,\ \mathbf{x}_2, \ldots \mathbf{x}_N) = \chi_i(\mathbf{x}_1)\chi_j(\mathbf{x}_2)\ldots\chi_N(\mathbf{x}_N). \tag{1.22}$$

This many-electron wavefunction, known as the Hartree product (HP), is uncorrelated, meaning that the position of electron $\mathbf{x}_i$ is only affected by an averaged mean field representation of its repulsion interaction with the other $N-1$ electrons in the system.

The wavefunction described by the Hartree product does not satisfy the Pauli anti-symmetry principle, which states that electronic wavefunctions must be antisymmetric with respect to the exchange of electrons. Representing the N-electron wavefunction as a Slater determinant rather than the simple Hartree product, the antisymmetry principle can be satisfied. An N-electron

Slater determinant has the following form:

$$\psi^{\mathrm{HF}}(\mathbf{x}_1, \mathbf{x}_2, \ldots \mathbf{x}_N) = \frac{1}{\sqrt{N!}} \begin{vmatrix} \chi_1(\mathbf{x}_1) & \ldots & \chi_N(\mathbf{x}_1) \\ \vdots & \ddots & \vdots \\ \chi_1(\mathbf{x}_N) & \ldots & \chi_N(\mathbf{x}_N) \end{vmatrix}. \tag{1.23}$$

This form of the wavefunction gives us the expression for energy as

$$E_{\mathrm{HF}} = \langle \psi_{\mathrm{HF}} | \hat{H} | \psi_{\mathrm{HF}} \rangle = \sum_{i=1}^{N} h_{ii} + \sum_{i>j}^{N} [(ii|jj) - (ij|ji)] + V_{nn}, \tag{1.24}$$

where V_{nn} is the nuclear repulsion energy, h_{ii} represents the one-electron part:

$$h_{ii} = \langle \chi_i | \hat{h} | \chi_i \rangle = \int \chi_i^*(\mathbf{x}) \left(-\frac{1}{2}\nabla_i^2 - \sum_{A_i} \frac{Z_A}{r_{Ai}} \right) \chi_i(\mathbf{x}) \, d\mathbf{x}, \tag{1.25}$$

and $(ii \,|\, jj)$ and $(ij \,|\, ji)$ denote two-electron contributions:

$$(ii \,|\, jj) = \iint \frac{\chi_i^*(\mathbf{x}_1)\chi_i(\mathbf{x}_1)\chi_j^*(\mathbf{x}_2)\chi_j(\mathbf{x}_2)}{r_{12}} \, d\mathbf{x}_1 d\mathbf{x}_2, \tag{1.26}$$

$$(ij \,|\, ji) = \iint \frac{\chi_i^*(\mathbf{x}_1)\chi_j(\mathbf{x}_1)\chi_j^*(\mathbf{x}_2)\chi_i(\mathbf{x}_2)}{r_{12}} \, d\mathbf{x}_1 d\mathbf{x}_2. \tag{1.27}$$

The contribution $(ii \,|\, jj)$ is a Coulomb integral and represents a positive contribution of energy (destabilisation) of a system due to electron-electron Coulombic repulsion, while the $(ij \,|\, ji)$ contribution is an exchange integral that does not have a classical interpretation. By defining the Coulomb operator $\hat{J}$ and exchange operator $\hat{K}$ as

$$\hat{J}\chi_i(\mathbf{x}_1) = \sum_j \int \frac{\chi_j^*(\mathbf{x}_2)\chi_j(\mathbf{x}_2)}{r_{12}} \, d\mathbf{x}_2 \chi_i(\mathbf{x}_1) \tag{1.28}$$

$$\hat{K}\chi_i(\mathbf{x}_1) = \sum_j \int \frac{\chi_j^*(\mathbf{x}_2)\chi_i(\mathbf{x}_2)}{r_{12}} \, d\mathbf{x}_2 \chi_j(\mathbf{x}_1) \tag{1.29}$$

The HF energy can now be rewritten in a succinct form:

$$E = \sum_{i}^{N} h_{ii} + \frac{1}{2} \sum_{i}^{N} \langle \chi_i | \hat{J} - \hat{K} | \chi_i \rangle \,. \tag{1.30}$$

The Fock operator $\hat{f}$ was introduced by Hartree and Fock in order to find orbitals to approximate a multi-electron wavefunction expressed as Slater determinants. The mean value of the operator for the i^{th} energy level is equal to the orbital energy corresponding to this level. Considering the variational principle, the Hartree–Fock method searches for such orthonormal orbitals, so that the total energy of the system is greater than or equal to the true energy of the molecule. The lower the calculated energy, the more accurate the description of the wavefunction that can be obtained.

When the HF energy (Eq. 1.30) is optimised, the spin-orbitals satisfy a set of equations:

$$\hat{f} \chi_i (\mathbf{x}) = \varepsilon_i \chi_i (\mathbf{x}) \,, \tag{1.31}$$

where ε_i are the orbital energies and $\hat{f}$ is the Fock operator. These are known as the HF equations. $\hat{f}$ is a one-electron operator that takes the following form:

$$\hat{f}(\mathbf{x}) = \hat{h}(\mathbf{r}_1) + \hat{J} - \hat{K}. \tag{1.32}$$

In the HF equations (Eq. 1.31), the Fock operator depends on its own eigenfunctions χ_i, therefore solving the HF equations must be done in a self-consistent manner.

To calculate the coefficients, molecular orbitals, and energy levels of a system to obtain the information about the whole chemical system, the self-consistent field (SCF) method is used.[41] It is an iterative approach which involves obtaining an initial guess of the orbitals, calculating Coulomb and exchange integrals, solving the Roothaan-HF equations, and testing for con-

vergence. If convergence criteria are not met, the process is repeated until the lowest energy is reached.

In HF theory the electron-electron repulsion, which plays a significant role in determining the electronic structure of molecules, is not accurately calculated. The electron-electron repulsion is expressed by having each electron move in an average electronic field due to the other electrons. Such a description leads to overestimated ground-state energies. This error is known as the correlation energy and can be written as

$$E_{\mathrm{c}} = E_{\mathrm{exact}} - E_{\mathrm{HF}} \tag{1.33}$$

where E_{c} is the correlation energy, E_{exact} is the exact energy of the system within the basis set and E_{HF} is the calculated Hartree–Fock energy for a given basis set. E_{c} is always negative.

The correlation energy is an important part of the calculations and should not be neglected. To increase the accuracy of the HF method, a number of post-HF methods have been developed including configuration interaction (CI), coupled cluster singles and doubles (CCSD), coupled cluster singles and doubles with perturbative triples (CCSD(T)), or second-order Møller–Plesset perturbation theory (MP2). However, in this thesis none of these methods is employed and therefore they will not be described in more detail.

Linear Combination of Atomic Orbitals

The drawback of the HF equations (Eq. 1.31) is that the wavefunction calculated based on the 'guess' orbitals is too complicated when molecular orbitals are considered, and it also lacks the qualitative understanding of the electron distribution. To solve that problem, Roothaan[42] and Hall[43] suggested to calculate close approximations of the molecular orbitals of a system by representing

them as a linear combination of functions known as basis functions, where each basis function is used to represent the atomic orbitals, hence the name for the method — linear combination of atomic orbitals (LCAO), where each nuclear orbital is written as

$$\varphi_i = \sum_{\mu}^{N_b} \varphi_{\mu}^{\mathrm{AO}} C_{\mu i}, \tag{1.34}$$

where i indexes the i^{th} MO, $C_{\mu i}$ is the coefficient of the μ^{th} basis function of the i^{th} MO and $\varphi_{\mu}^{\mathrm{AO}}$ is the μ^{th} basis function with N_b as the number of basis functions, which depends on the collection of specific basis functions being used, known as a basis set. Basis sets will be discussed later in the text.

The Roothaan–Hall version of the HF equations can be written in matrix notation as

$$\mathbf{FC} = \mathbf{SC}\boldsymbol{\epsilon}, \tag{1.35}$$

where $\mathbf{C}$ is the matrix containing the coefficients $C_{\mu i}$, $\boldsymbol{\epsilon}$ is a diagonal matrix of the orbital energies, and $\mathbf{S}$ is the overlap matrix between AO functions:

$$S_{\mu\nu} = \langle \varphi_{\mu}^{\mathrm{AO}} | \varphi_{\nu}^{\mathrm{AO}} \rangle \,, \tag{1.36}$$

and $\mathbf{F}$ is the Fock operator in its matrix representation:

$$F_{\mu\nu} = \langle \varphi_{\mu}^{\mathrm{AO}} | \hat{F} | \varphi_{\nu}^{\mathrm{AO}} \rangle \,. \tag{1.37}$$

Basis sets

An important factor to consider in HF theory is a choice of basis functions. The number of basis functions used in calculations affects the computational cost, and the choice of the basis set should be appropriate to the required calculations. A basis set is a set of mathematical functions (basis functions) which is used for LCAO to represent MOs, as shown in Eq. 1.34. The selection

of an appropriate basis set is an important prior step when performing quantum chemical calculations. On one hand, the basis set must be large enough in order to get the correct results, as the accuracy of the description of the given system improves with the size of the basis set. On the other hand its size must not exceed the computational capacity of the computer on which the calculations are performed. The most widely used functions that can be used to represent the electron distribution around an atom are Slater and Gaussian functions. While Slater functions provide better description at the nucleus and the correct radial distribution,[44] Gaussian functions are easier to integrate and thus are frequently used in computer calculations but, compared to the Slater functions, they describe the orbitals in a less precise way. To combine the advantages of both approaches, the idea of contracted basis functions has been proposed. Contracted basis functions are is composed of several Gaussian functions and used to approximate a Slater function. A linear combination of Gaussians provides a better approximation to a Slater function than just a single Gaussian. As an example, STO-3G is a contracted Gaussian basis set with three Gausians contracted in each basis function.

Another type of basis set, developed by John Pople, is called the split-valence basis set,[45] where core orbitals can be considered separately from the valence orbitals due to the fact that they are less likely to change in a molecular environment. The description of valence orbitals is split into two (or more) basis functions: in double-ζ basis sets two functions are used for each orbital; in triple-ζ basis sets three functions are used for each orbital. For example, in the 3-21G basis set, the core orbitals are described by one basis function as a contraction of three Gaussian functions, while the valence orbitals are split to an inner shell and an outer shell, which are described by linear combinations of two Gaussian functions, and one single Gaussian function, respectively. This operation allows the function to fall off more slowly, which then allows the valence orbitals to be more diffuse and have a longer spatial range. For mod-

eling most chemical properties, it is necessary to take into account additional polarization functions (*i.e.* functions with a greater quantum number l than in the HOMO orbital of a given atom). In contrast to previously described basis sets, the polarization functions are usually added in a non-contracted form. They are denoted by an asterisk, *e.g.* 3-21G*. To expand the basis set further, diffuse functions can be added (denoted by a plus, *e.g.* 3-21+G*), which are characterized by a small exponent, and thus a large radial range. This is particularly important in the case of lone-pair electrons that are far away from the nuclei and thus loosely bind to the molecular system.

Another type of basis set is the Dunning basis sets,[46] so called correlation-consistent basis sets. The popular basis sets belonging to this group include cc-pVDZ and cc-pVTZ. The 'cc-p' stands for correlation-consistent polarisation, the 'V' stands for valence only, 'D' represents double, and 'T' triple.

Most of the time all-electron basis sets are a natural choice for all calculations, but there are two problems with using them for certain systems, including large molecular systems. The first one to consider is the computational cost, high number of atoms within the systems can significantly increase the cost of the calculations. Another aspect to consider is that the all-electron basis sets do not take relativistic effects into account. This is relevant for our work which focuses on QDs based on heavier atoms (Si and Ge).

An alternative to all-electron basis sets is the use of effective core potentials (ECPs). In the ECP basis set, the innermost electrons are replaced by a potential that models the effect of these electrons on the valence electrons. An example of this are Stuttgart Relativistic Small Core (SRSC) ECP basis sets,[47] which have only a small number of electrons confined to the 'core' part of the ECP, or Los Alamos Lab (LANL) ECPs basis sets which uses combination of ECP and valence besis set. For instance, LANL2DZ is a double zeta basis with an ECP and has a large core ECP and therefore a relatively small basis set.

Both ECP basis sets, SRSC and LANL provide accurate results, or lower cost especially for molecules containing heavy atoms.

1.2.4 Density Functional Theory

Hohenberg–Kohn Theorems

The Hartree–Fock method described in previous sections does not consider electron correlation, whereas post-HF wavefunction methods are computationally expensive, due to the increased number of configurations present in the methods for big systems. The competitive approach to describe multi-electron systems is Density Functional Theory (DFT). In this method, a chemical system is described by its density, rather than wavefunction. The main advantage of this method is the highly reduced number of quantities thus allowing for more cost-effective computation, and consequently enabling computation of more advanced systems.

The electron density $\rho(\mathbf{r})$ is a function which describes the probability of finding electrons within the volume $d\mathbf{r}$. For a system with N electrons, its electron density must satisfy

$$\int \rho(\mathbf{r})\ d\mathbf{r} = N. \tag{1.38}$$

The ground-state density provides the number of electrons, the position and the charge of nuclei, and hence it contains all the information about the system. It is in principle possible to obtain the Hamiltonian from the density, therefore solve the Schrodinger equation and provide a wavefunction for the ground state system. Theoretical justification for electron density is provided by the Hohenberg and Kohn theorems:[48]

1. A ground-state energy functional exists and it is uniquely determined by

the electron density: $E[\rho]$.

2. The energy functional in Theorem 1 is variational:

$$E\left[\rho'\right] \geq E_{\text{exact}} \tag{1.39}$$

Hohenberg and Kohn showed that the electronic Hamiltonian, and therefore also the ground state wavefunction, energy, and other molecular properties, are uniquely determined by the ground state electron density. The expression for the energy can be split into two parts:

$$E[\rho] = E_{\text{HK}}[\rho] + \int \rho(\mathbf{r}) v_{\text{nuc}}(\mathbf{r})\, d\mathbf{r}. \tag{1.40}$$

The first term, $E_{\text{HK}}[\rho]$, is called the universal functional which is unknown and has the following general form:

$$E_{\text{HK}}\left[\rho\right] = T\left[\rho\right] + J\left[\rho\right] + E_{\text{xc}}\left[\rho\right] \tag{1.41}$$

where $T[\rho]$ is the kinetic energy functional which is unknown, $J\left[\rho\right]$ is the Coulomb energy functional which is known, and $E_{\text{xc}}\left[\rho\right]$ is the exchange and correlation functional and is unknown. The second term in Eq. 1.40 gives the interaction energy of the density ρ with the external potential v_{nuc} due to the nuclei.

Kohn–Sham DFT

Kohn–Sham DFT (KS-DFT) provides a practical approach to DFT.[49] This method introduces a fictitious reference system of non-interacting electrons moving in an effective external potential chosen such that the density of the reference system is the same as that of the ground state of the real system.

In the fictitious system, the electrons can be described by KS MOs (χ)

such that the density can be written as

$$\rho(\mathbf{r}) = \sum_{i}^{N} |\chi_i(\mathbf{r})|^2 . \tag{1.42}$$

The KS MOs also allow the kinetic energy functional to be split into the non-interacting part ($T_\mathrm{s}[\rho]$) and the correlated part ($T_\mathrm{c}[\rho]$). The non-interacting part can be written as

$$T_\mathrm{s}[\rho] = \sum_{i}^{N} \left\langle \chi_i \left| -\frac{1}{2}\nabla^2 \right| \chi_i \right\rangle , \tag{1.43}$$

whereas the correlated part does not have a known form and is therefore often subsumed under $E_\mathrm{xc}[\rho]$. The new expression for the energy can be written as

$$E[\rho] = T_\mathrm{s}\left[\rho\right] + J\left[\rho\right] + E_\mathrm{xc}\left[\rho\right] + \int \rho(\mathbf{r}) v_\mathrm{nuc}(\mathbf{r})\ d\mathbf{r}. \tag{1.44}$$

By optimising the energy functional $E[\rho]$ with respect to variations of the KS MOs, a set of Kohn–Sham equations is obtained:

$$\hat{f}_\mathrm{KS}\chi_i = \epsilon_i \chi_i, \tag{1.45}$$

where $\hat{f}_\mathrm{KS}$ is the KS operator derived from the functional derivative of $E[\rho]$ with respect to electron density:

$$\hat{f}_\mathrm{KS} = -\frac{1}{2}\nabla^2 + v_\mathrm{j} + v_\mathrm{xc} + v_\mathrm{nuc} \tag{1.46}$$

The term v_xc is the exchange-correlation potential which can be expressed as

$$v_\mathrm{xc}(\mathbf{r}) = \frac{\partial E_\mathrm{xc}[\rho]}{\partial \rho(\mathbf{r})}. \tag{1.47}$$

Knowledge of the exact form of the exchange-correlation functional E_xc would allow the calculation of the exact energy value, *i.e.* correct eigenvalues of the $\hat{H}_\mathrm{elec}$ operator from the electronic Schrödinger equation. The only approxi-

mation in the KS-DFT method to be made relates to finding the v_{xc}. This approximation and finding the exchange-correlation functional is the main task of DFT. This decides how accurate results will be. Nonetheless, DFT energy will always be slightly different to the true energy of a system as the E_{xc} consists of of terms and so prevents the calculation to be exact. The difference between the calculated and real energy will depends on both the size of the basis set and the choice of the exchange-correlation functional.

Exchange and Correlation Functionals

In order to calculate the exchange correlation energy, several types of approaches are used. Local functionals including LDA (local density approximation) and LSDA (local-spin density approximation), and non-local, which can be then divided into gradient methods (GGA approximation, a gradient corrected or generalized gradient approximation, (*e.g.*, PW91) and hybrid methods (*e.g.*, B3LYP potential). The approximation of the LDA[50] is based on the approximation of the correlation-exchange energy functional through the energies of homogeneous electron gas. In addition, it assumes that the density in the molecule is local, which means that in a small volume the density is homogeneous. It is the simplest approximation of the correlation-exchange energy functional in which both exchange and correlation are local. For an uniform electron gas (UEG), an LDA exchange-correlation functional, and its derivative can be accurately calculated according to

$$E_{xc}^{LDA} = \int e_{xc}^{UEG}[\rho(\mathbf{r})]\ d\mathbf{r}, \tag{1.48}$$

where $e_{xc}^{UEG}[\rho(\mathbf{r})]$ is the exchange-correlation energy per unit volume of a uniform electron gas having the local value $\rho(\mathbf{r})$ of the density.

Although LDA supports calculations for molecular properties such as bond length, dissociation and ionization energies, its accuracy is poor where electron-

electron interactions are dominant. A method to improve the results of LDA or LSDA is based on using two main quantities, the density and information about the gradient at **r**. The functionals that utilise both the electron density at a point as well as the gradient at **r** are called generalised-gradient approximation functionals (GGA). One of the example that uses a GGA functional is the Becke exchange functional with the Lee–Yang–Parr correlation functional (BLYP). However, Becke found that including some Hartree–Fock exchange into the BLYP functional can partially correct the lack of accuracy of BLYP for some molecular properties. The resulting functional is called B3LYP and it is a hybrid exchange-correlation functional,[51] which includes a component of exact HF exchange, LDA exchange, and GGA exchange functionals along with correlation functionals. It is described by

$$\begin{aligned} &E_{\mathrm{xc}}^{\mathrm{B3LYP}}[\rho] \\ &\quad = (1-a-b)E_{\mathrm{x}}^{\mathrm{LDA}}[\rho] + aE_{\mathrm{x}}^{\mathrm{HF}} + bE_{\mathrm{x}}^{\mathrm{B88}}[\rho] + cE_{\mathrm{c}}^{\mathrm{LYP}}[\rho] + (1-c)E_{\mathrm{c}}^{\mathrm{VWN}}[\rho], \end{aligned} \tag{1.49}$$

where

$$a = 0.20, b = 0.72, c = 0.81,$$

and is one of the most frequently used exchange-corelation functionals in quantum chemistry. However, B3LYP is not always accurate at simulating electron excitations, especially those involving charge transfer (CT). This failure is assigned to the CT states which require full (100%) HF exchange, whereas standard functionals typically only contain around 20% HF exchange. The excitation energy for a CT transition in the TDDFT method (described in subsection 1.2.4) is essentially the energy difference between the orbital energies. Due to the approximate exchange in the functional, this excitation is often underestimated. To address the problem, long-range corrected functionals have been developed such as Coulomb-attenuated method B3LYP (CAM-B3LYP).[52] These functionals include an increasing amount of HF exchange as

the distance between electrons increases, and partition the electron electron Coulomb potential into short- and long-range terms,

$$\frac{1}{r_{12}} = \frac{1 - [\alpha + \beta \cdot \mathrm{erf}(\mu r_{12})]}{r_{12}} + \frac{\alpha + \beta \cdot \mathrm{erf}(\mu r_{12})}{r_{12}}. \tag{1.50}$$

The first term describes short-range interactions and the second the long-range interactions. The amount of HF exchange is represented by α and DFT exchange by β. This exchange-correlation functional is popular when the transfer of electron density is involved during calculations of the excited states, for instance using TDDFT method described in subsection 1.2.5. In X-ray spectroscopy, where the accurate description of core hole is required, the short-range electron-electron interactions are must be well described. The short-range corrected analogues of CAM-B3LYP are SRC,[53,54] specifically designed for XAS calculations, and have following form:

$$\begin{aligned}\frac{1}{r_{12}} = C_{\mathrm{SHF}} \frac{1 - \mathrm{erf}(\mu_{\mathrm{SR}} r_{12})}{r_{12}} + C_{\mathrm{LHF}} \frac{1 - \mathrm{erf}(\mu_{\mathrm{LR}} r_{12})}{r_{12}} \\ - C_{\mathrm{SHF}} \frac{1 - \mathrm{erf}(\mu_{\mathrm{SR}} r_{12})}{r_{12}} + C_{LHF} \frac{1 - \mathrm{erf}(\mu_{LR} r_{12})}{r_{12}} + \frac{1}{r_{12}},\end{aligned} \tag{1.51}$$

where C_{SHF} and C_{LHF} are quantities related to the HF exchange portion in the long- and short-range interactions, and μ_{SR} and μ_{LR} are the long- and short-range quantities enabling control over the range separation.

1.2.5 Time-Dependent Density Functional Theory

The transition of the system to the excited state occurs as a result of interactions with an external disturbance, *e.g.* an electromagnetic wave. This interaction is expressed through a change in the external potential of the system. Time-dependent DFT (TDDFT) is an extension of ground-state DFT methods that has been proposed for the calculation of excited states and has been

shown to be successful in prediction of electronic transitions.[53,55,56] The ground-state Hohenberg–Kohn theorems state that, based on the ground-state electron density, it is possible to describe ground-state properties of a molecule, with a ground-state property being a functional of the electron density, and that the energy is variational. The Runge-Gross theorem,[57] extends the Hohenberg–Kohn theorem to a time-dependent framework and states that all properties can be calculated with the knowledge of the one-body density and that all these properties are functionals of the density. It proves the existence of a one-to-one mapping between the time-dependent external potential and time-dependent electron density.

Introducing an external electric potential and solving the time-dependent Schrödinger equation via a functional of density leads to the time-dependent KS equations:

$$\hat{f}_{\mathrm{KS}}(\mathbf{r},t)\chi(\mathbf{r},t) = i\hbar\frac{\partial\chi(\mathbf{r},t)}{\partial t}, \tag{1.52}$$

where the time-dependent Fock operator has the form

$$\hat{f}_{\mathrm{KS}}(\mathbf{r},t) = -\frac{1}{2}\nabla^2 \; + v_{\mathrm{ext}}(\mathbf{r},t) + \int \frac{\rho(\mathbf{r},t)}{r_{12}}\, d\mathbf{r}_2 + \frac{E_{\mathrm{xc}}[\rho(\mathbf{r},t)]}{\rho(\mathbf{r})}. \tag{1.53}$$

In Eq. 1.53, the exchange-correlation energy term is a functional of $\rho(\mathbf{r},t)$. Typical implementations of TDDFT use the linear response (LR) of the dynamic polarizability $\alpha(\omega)$ in which the ground state equations for the molecule are solved first, and then a time-dependent perturbation in the dynamic polarizability is applied to the molecule. The response of the system to an applied electric field generates an absorption spectrum by the following equations:

$$\alpha(\omega) = \sum_I \frac{f_I}{\omega_I^2 - \omega^2}, \tag{1.54}$$

$$f_I = \frac{2}{3}\left\langle\chi_0|\hat{\mu}|\chi_I\right\rangle^2, \tag{1.55}$$

$$\omega_I = E_I - E_0. \tag{1.56}$$

The excitation energies are determined by the poles of the dynamic polarizability $\alpha(\omega_I)$ and the corresponding oscillator strengths of the spectrum are described by f_I.

Casida[58] formalised TDDFT by considering linear response to the external potential. In this approach, the excitation energy relates to poles which can be calculated from the response to a time varying applied external field using equations of the form:

$$\begin{pmatrix} \mathbf{A} & \mathbf{B} \\ \mathbf{B} & \mathbf{A} \end{pmatrix} \begin{pmatrix} \mathbf{X} \\ \mathbf{Y} \end{pmatrix} = \omega \begin{pmatrix} -\mathbf{1} & \mathbf{0} \\ \mathbf{0} & \mathbf{1} \end{pmatrix} \begin{pmatrix} \mathbf{X} \\ \mathbf{Y} \end{pmatrix}, \tag{1.57}$$

where ω are the excitation energies, $\mathbf{X}$ and $\mathbf{Y}$ are the associated eigenvectors which contain information about the density response function, and the elements of matrices $\mathbf{A}$ and $\mathbf{B}$ are defined as

$$A_{ia,jb} = \delta_{ij}\delta_{ab}(\epsilon_a - \epsilon_i) + (ia \,|\, jb) + (ia \,|f_{\mathrm{xc}}|\, jb), \tag{1.58}$$

$$B_{ia,jb} = (ia \,|\, bj) + (ia \,|f_{\mathrm{xc}}|\, bj), \tag{1.59}$$

with the integrals defined as

$$(ia \,|\, jb) = \iint \frac{\chi_i^*(\mathbf{r}_1)\chi_a(\mathbf{r}_1)\chi_j^*(\mathbf{r}_2)\chi_b(\mathbf{r}_2)}{r_{12}}\, d\mathbf{r}_1 d\mathbf{r}_2, \tag{1.60}$$

$$(ia \,|f_{\mathrm{xc}}|\, jb) = \iint \chi_i^*(\mathbf{r}_1)\chi_a(\mathbf{r}_1)\frac{\partial^2 E_{\mathrm{xc}}}{\partial \mathbf{r}_1 \partial \mathbf{r}_2}\chi_j^*(\mathbf{r}_2)\chi_b(\mathbf{r}_2)\, d\mathbf{r}_1 d\mathbf{r}_2. \tag{1.61}$$

The solution to this equation gives eigenvalues corresponding to excitation energies, and eigenvectors that can be used to obtain the transition oscillator strengths.

Another approximation, which is computationally cheaper and commonly used with TDDFT, is the Tamm–Dancoff approximation.[59] In this approximation, $\mathbf{B}$ from Eq. 1.57 is assumed to be zero and the excitation energies of the

system satisfy a simpler eigenvalue equation:

$$\mathbf{AX} = \omega\mathbf{X}. \tag{1.62}$$

1.2.6 Maximum Overlap Method (MOM)

The Maximum Overlap Method (MOM) is an alternative to TDDFT for obtaining low-cost excited states. It modifies the orbital selection step in the SCF procedure to obtain excited SCF determinants. It selects orbitals that resemble those from the previous cycle rather than those with lowest eigenvalues. It is a very helpful method for modelling charge-transfer and Rydberg transitions, as well as for modelling very high lying states, such as those involving excitation of core electrons. To optimise the coefficients of an excited state wavefunction, MOM proposes maximizing the overlap of occupied orbitals between consecutive cycles of the SCF procedure.[60] The SCF procedure in MOM adds an extra constraint to maximize the overlap with the orbitals of the previous cycle. This enables the convergence to electronic configurations higher in energy than the ground state. Furthermore, the optimized ground state can be used to promote an electron to an unoccupied orbital at the start of the SCF cycle, which prevents variational collapse during the procedure. MOM can generate core-ionised and core-excited wavefunctions (useful for X-ray spectroscopy) and HOMO-excited wavefunctions (useful for UV-Vis spectroscopy), which can be then used to calculate spectra by the energy difference between the ground and excited (or ionised) state. The following equations are used for the transition energy and oscillator strengths between initial and final states respectively,

$$\Delta E = E_{\mathrm{f}} - E_{\mathrm{i}}, \tag{1.63}$$

$$f_{\mathrm{f}\leftarrow\mathrm{i}} \propto \left|\langle\psi_{\mathrm{f}}|\hat{\boldsymbol{\mu}}|\psi_{\mathrm{i}}\rangle\right|^2, \tag{1.64}$$

where ψ_{i} and ψ_{f} are the initial and final electronic states involved in the electronic transitions, respectively.

1.2.7 Vibrationally Resolved Electronic Spectra

The Harmonic Approximation

The nuclear vibrational states of a molecule correspond to bands observed in IR and Raman spectroscopy. Using quantum mechanics, it is possible to simulate a vibrational spectrum for a known molecular geometry, and to find out the correct structure of a molecule when only the spectrum is available.As a first approximation for the description of basic vibrational information of molecules, the quantum harmonic oscillator model is used. The potential energy curve of each vibrational mode can be approximated by a harmonic potential close to the stationary point that represent the equilibrium geometry.

For example, in a diatomic molecule, the lowest energy of the potential energy curve occurs at its optimal bond length. If the two atoms in the molecule are forced closer together or pulled further apart, the energy increases. Consequently, in the first case, the two atoms repel each other back to the lowest energy state, whereas in the second case, the energy increases to the point where the molecule dissociates. The quantum harmonic oscillator model is based on the simplification of the Taylor series expansion of the full vibrational potential energy curve:

$$V(q) = V(q_0) + \left.\frac{dV(q)}{dq}\right|_{q=q_0} (q-q_0) + \frac{1}{2!}\left.\frac{d^2V(q)}{dq^2}\right|_{q=q_0} (q-q_0)^2 + \ldots + \frac{1}{n!}\left.\frac{d^nV(q)}{dq^n}\right|_{q=q_0} (q-q_0)^n, \quad (1.65)$$

where q is a vibrational coordinate and q_0 its value at the equilibrium geometry.

By retaining terms up to second order, the above series can be simplified to

$$V(q) = V(q_0) + \left.\frac{dV(q)}{dq}\right|_{q=q_0} (q - q_0) + \frac{1}{2!} \left.\frac{d^2V(q)}{dq^2}\right|_{q=q_0} (q - q_0)^2. \tag{1.66}$$

Furthermore, at an equilibrium structure, $V(q_0)$ is stationary and $\left.\frac{dV(q)}{dq}\right|_{q=q_0}$ vanishes. The potential energy curve then becomes

$$V(q) = V(q_0) + \frac{1}{2!} \left.\frac{d^2V(q)}{dq^2}\right|_{q=q_0} (q - q_0)^2 \tag{1.67}$$

When $V(q_0)$ has been set to be zero for convenience and the displacement q redefined to be $q = q - q_0$, then

$$V(q) = \frac{1}{2}kq^2, \tag{1.68}$$

where $k = \left.\frac{d^2V(q)}{dq^2}\right|_{q=q_0}$.

The nuclear Schrodinger equation can then be solved using the Born–Oppenheimer approximation by

$$\left[-\frac{1}{2\mu}\frac{d^2}{dq^2} + \frac{1}{2}kq^2\right]\psi(q) = E\psi(q), \tag{1.69}$$

where μ is the reduced mass of the diatomic. The above equation can be generalised for larger polyatomic molecules consisting of M nuclei as[61]

$$\left[-\frac{1}{2}\sum_{\alpha}^{3M}\frac{\partial^2}{\partial {q_\alpha}^2} + \frac{1}{2}(\mathbf{q} - \mathbf{q}_0)^{\mathsf{T}}\ \mathbf{h}(\mathbf{q}_0)\ (\mathbf{q} - \mathbf{q}_0)\right]\psi(\mathbf{q}) \ = \ E\psi(\mathbf{q}), \tag{1.70}$$

where $\mathbf{q}$ is a column vector of $3M$ mass-weighted atomic coordinates, $\mathbf{q}_0$ is its value at an equilibrium geometry, and $\mathbf{h}(\mathbf{q}_0)$ is the mass-weighted Hessian matrix evaluated at $(\mathbf{q}_0)$. The model is solved by diagonalization to obtain eigenvalues corresponding to the frequencies of the normal modes and eigenvectors corresponding to the normal mode displacements.

Vibrational frequencies are often overestimated by computational methods, so it is common to scale these harmonic modes. Scaling factors have been determined for various computational methods based on comparison to experimental results. This scaling accounts for the neglect of anharmonicity in the calculation of the vibrational modes and the errors in the method used to calculate the frequencies.

Additionally, the probability that vibrational transitions will occur can be calculated and compared to experimental data. The infrared intensity for a particular vibrational mode with normal coordinate Q_i is given by the change in the electric dipole moment $\boldsymbol{\mu}$ during molecular vibration, which can be calculated within the harmonic approximation from the proportionality:

$$I_i \propto \left| \frac{\partial \boldsymbol{\mu}}{\partial Q_i} \right|^2 . \tag{1.71}$$

The Franck–Condon Principle

The Franck–Condon Principle is a rule which uses the Born–Oppenheimer approximation to describe the intensities of vibronic transitions, and the absorption or emission of a photon.[62,63] This principle states that the nuclear configuration of a molecule does not change when an electronic transition occurs, resulting in vertical transitions on electronic potential energy curves. This is due to the difference in mass between nuclei and electron, with nuclei being much heavier than the electron and therefore cannot respond as quickly during the electronic transition. Once the nuclei realign to the new electronic configuration, the excited molecule relaxes by vibration.

The probability of vibrational transition occurring is given by

$$P_{\mathrm{f}\leftarrow\mathrm{i}} = |\langle \psi_\mathrm{f} | \hat{\boldsymbol{\mu}} | \psi_\mathrm{i} \rangle|^2 = \left| \int \psi_\mathrm{f}^* \hat{\boldsymbol{\mu}} \psi_\mathrm{i} d\mathbf{r} \right|^2 , \tag{1.72}$$

where $\hat{\boldsymbol{\mu}}$ is the electric dipole operator. In the Born–Oppenheimer approximation, the total wavefunction can be written as

$$\psi_{\text{total}}(\{\mathbf{x}_i\}, \{\mathbf{R}_A\}) = \psi_{\text{nuc}}(\{\mathbf{R}_A\})\ \psi_{\text{el}}(\{\mathbf{x}_i\}; \{\mathbf{R}_A\}) \tag{1.73}$$

where ψ_{nuc} is the nuclear wavefunction that depends on the nuclear coordinates $\{\mathbf{R}_A\}$, and ψ_{el} is the electronic wavefunction that depends on the electronic coordinates $\{\mathbf{x}_i\}$ and also on the nuclear coordinates $\{\mathbf{R}_A\}$ parametrically. This allows the wavefunctions in Eq. 1.72 to be separated into electronic and nuclear components, yielding

$$P_{\text{f}\leftarrow\text{i}} = \left|\langle\psi_{\text{total,f}}|\hat{\boldsymbol{\mu}}|\psi_{\text{total,i}}\rangle\right|^2 = \left|\langle\psi_{\text{nuc,f}}|\psi_{\text{nuc,i}}\rangle\right|^2 \left|\langle\psi_{\text{el,f}}|\boldsymbol{\mu}|\psi_{\text{el,i}}\rangle\right|^2 . \tag{1.74}$$

If the nuclear overlap $\langle\psi_{\text{nuc,f}}|\psi_{\text{nuc,i}}\rangle$ is zero for this transition, then the transition will not be observed. In fact, the Franck–Condon principle states that the intensity of a vibronic transition relates to the overlap of the vibrational wave functions for the ground and excited states. Using this method, it is possible to calculate intensities which are analogous to the absorbance in experimental spectra.

Chapter 2

Quantum Chemical Characterisation and Design of Quantum Dots for Sensing Applications

2.1 Introduction

Biosensors play a vital role in medicine, where for example, early detection of cancer biomarkers can significantly reduce morbidity and mortality worldwide.[64,65] Optical biosensors form one class of biosensor and can be applied to the detection of disease biomarkers and other biomolecules.[66–68] An optical biosensor is often comprised of different components that have different functions. The receptor is responsible for capturing the molecule (analyte) under study which leads to a detectable change in the fluorescence of the fluorophore, in the form of a change in wavelength or an enhancement or quenching of the fluorescence. A wide variety of chemical species can be used as the fluorophore, ranging from bodipy dyes[69,70] to green fluorescent protein.[71–75] More recently,

the application of quantum dots (QDs) in biosensing has become increasingly important[71–73] owing to their favorable sensing properties, biocompatibility and chemical inertness.[76] QDs are 1 – 20 nm luminescent semiconductor nanostructures with interesting photophysical and photochemical properties.[77–79]

The small size of QDs gives them unique absorption and emission properties as a consequence of the quantum confinement effect leading to their photoluminescence being size and composition dependent.[78] Through variation in composition and size, it is possible to obtain fluorescence in the full spectral range from ultraviolet (UV) to near infrared coupled with the capability to tune the fluorescence. They are characterized by a broad absorption band and narrow fluorescence emission profile which makes them ideal candidates for optical sensing applications. Additionally, QDs can be repeatedly excited without a noticeable decrease in their fluorescence because they have a high quantum yield, as well as a long radiation emission time (10 – 100 ns). Moreover, their fluorescence shows high resistance to photobleaching.[80,81] Some of the examples of using QDs in biosensors include, manganese doped zinc sulphide (ZnS:Mn/Zns) quantum dots functionalised with cysteine for the sensing of bilirubin,[82] thioglycolic acid functionalised ZnS:Mn/ZnS quantum dots for the sensing of creatinine[83] and CdSe/ZnS quantum dots functionalised with dopamine for the sensing of the α-fetoprotein.[84] A number of different photophysical processes underpin the sensing mechanisms in QD based systems, and these include photo-induced electron transfer (PET), charge transfer (CT), and fluorescence resonance energy transfer (FRET).[85–87] In the case of the PET mechanism, the excited fluorophore can accept or donate electrons leading to quenching of the photoluminescence in oxidative or reductive PET processes.[87] For the CT mechanism there is a change in the overall charge distribution in the system. Often the receptor and fluorophore coexist in the same conjugated system or there is a strong interaction between them making the photophysical behaviour strongly dependent on the analyte.[85] In the FRET mechanism, a

transfer of excitation energy occurs causing a decrease in the donor photoluminescence intensity, and the distance between donor and acceptor can influence the fluorescence process.[86]

Alongside experimental work,[88,89] computational studies can contribute to the understanding of the relationship between the structural and optical properties of QDs. Furthermore, they allow the nature of the sensing mechanism to be probed and have the potential to guide the design of QDs for specific sensing applications. In recent years there has been a number of studies that have used density functional theory (DFT) and time-dependent density functional theory (TDDFT) to study the properties of fluorescent biosensors[83,90,91] including QD based systems.[92–98] It is common to interpret the photophysical behaviour of the fluorophores in terms of the molecular orbital diagram based upon the KS orbitals and energies.[99–104] A more accurate approach is to calculate the excited states explicitly through TDDFT or higher level wavefunction based calculations, which can also provide greater insight into the sensing mechanisms of the fluorescent probes.[105–114] Examples of studies of QDs include hydrogenated silicon quantum dots of varying sizes[93] boronated and oxidated graphene QDs,[94] and graphene QDs functionalised with various, oxygen containing functional groups.[94] Calculation of emission spectra have been reported for functionalised graphene quantum dots,[96] acetate functionalised CdSe[97] or halogen atoms passivated silicon nanocrystals.[98] Dye-sensitised QDs have been studied with TDDFT with the effects of solvent included through polarized continuum solvent models.[115,116] Also, studies involving orbital characterisation have been performed for ligated QDs which have included investigation of CT mechanisms.[87,117,118]

The studies discussed above demonstrate that it is possible to use DFT and TDDFT calculations to characterise the properties of QD-based sensors and rationalise the photophysical processes underlying the sensing mechanism. This leads to the question of whether these calculations can be utilised in the

design of sensors for a particular sensing application. In this work we focus on a dopamine (DA)-functionalized QD sensor, similar to one reported in experimental work by Zhang *et al.*[84] This sensor detects the disease biomarker ALFA-fetoprotein exploiting the catalytic oxidation of DA to DA-quinone which results in the fluorescence quenching of a CdSe/ZnS QD. We have explored how DFT and TDDFT calculations can be exploited to characterise and guide the design of hydrogenated carbon silicon and germanium QDs for this sensing application.

2.2 Computational Methods

The structure of the QDs was taken from the work of Karttunen *et al.*[119] who studied the structure and electronic properties of a series of hydrogenated carbon, silicon and germanium clusters using DFT with the B3LYP functional[120] and def2-SVP basis set. It was found that the band gap decreases as the size of the cluster increases. The band gap for the silicon and germanium clusters are similar, and smaller than those of the carbon clusters of comparable size. In this work, two types of QDs have been studied, those with diamond-like structure and icosahedral structure, and these QDs are shown in Figure 2.1. The size of the QDs range from 35 to 280 C, Si or Ge atoms with 36 to 120 H atoms. The diameter of the small ($X_{35}H_{36}$) QDs is 0.9 nm for Si, 1.3 nm for Ge and C, and for the large ($X_{280}H_{144}$) QDs 2.1 nm, 2.9 nm and 1.9 nm for Ge, Si and C, respectively.[119] The structure of the QDs with the oxidised and reduced forms of dopamine (DOP) absorbed onto the QDs were optimized using B3LYP/def2-SVP level of theory. The initial choice of the attachment of the DOP molecule to the QD surface via an $-(C{=}O)CH_2S$ linking group was guided by experimental observations.[84] The effect of the anchoring group and position of DOP at the QD surface (edge, corner, and face sites) has been further investigated.

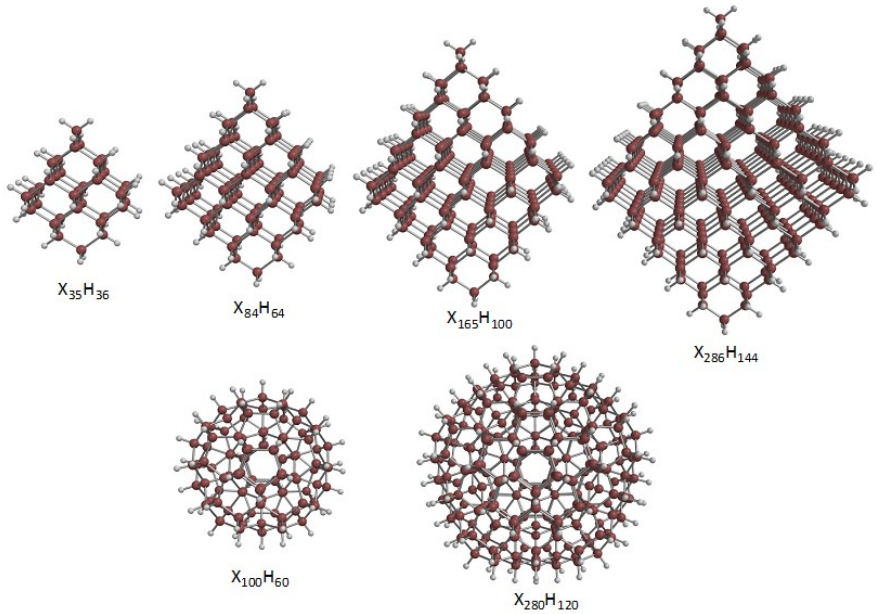


Figure 2.1: *Structures for QDs with various sizes. X = Ge, Si or C.*

To be able to study the larger QDs, it is necessary to establish a level of theory that is both computationally efficient and accurate. The excited states and corresponding absorption spectra were first computed using TDDFT with the CAM-B3LYP functional and a range of all-electron and effective core potential (ECP) basis sets (Table 2.1). All calculations were performed using the Q-Chem software package.[120] In addition, Table 2.2 shows the excitation energies calcualted with the Tamm–Dancoff approximation (TDA). However these calculations show that in all cases of interest the TDA approximation does not improve the values of excitation energies.

The low-lying excited states were of a main focus since these are the most relevant for a fluorescence-based sensor. There have been relatively few computational studies of the excited states of these systems, but some TDDFT calculations primarily for silicon have been reported[86,93,121,122] and TDDFT calculations have been shown to be accurate for studying other systems composed of dopamine and nanoparticles such as TiO_2,[123] Ag,[91] and Au.[124]

Table 2.1 summarises the lowest four singlet transition energies for $X_{35}H_{36}$ QDs (X = C, Si and Ge) calculated using the TDDFT/CAM-B3LYP level of

Table 2.1: Lowest four singlet transition energies (ΔE/eV) for $C_{35}H_{36}$, $Si_{35}H_{36}$, and $Ge_{35}H_{36}$ quantum dots calculated using TDDFT/CAM-B3LYP with several basis sets.

	ΔE/eV					
	6-31G*	6-31+G*	6-31++G**	def2-SVP	LANL2DZ	SRLC
$Ge_{35}H_{36}$	4.87	4.84	4.84	4.90	5.20	4.87
	5.03	5.00	5.00	4.93	5.34	5.04
	5.09	5.04	5.03	5.09	5.41	5.14
	5.17	5.12	5.10	5.20	5.42	5.25
$Si_{35}H_{36}$	5.17	5.19	5.18	5.16	5.68	5.54
	5.26	5.20	5.19	5.27	5.78	5.64
	5.28	5.39	5.38	5.30	5.83	5.70
	5.48	5.46	5.45	5.50	6.08	5.87
$C_{35}H_{36}$	8.17	6.45	6.30	7.62	8.14	8.14
	9.18	6.89	6.71	8.43	9.13	9.15
	9.47	7.23	7.06	8.80	9.47	9.49
	9.52	7.29	7.13	8.85	9.53	9.53

theory with the 6-31G*, 6-31+G*, 6-31++G**, def2-SVP all-electron basis sets and LANL2DZ and SRLC ECP basis sets. It can be observed that in the latter case, the 6-31G basis set is used for the hydrogen atoms. For Ge- and Si-containing quantum dots, the results show a weak variation of the predicted transition energies with the choice of all-electron basis sets, however the effect is significant for the C-based QDs. For $C_{35}H_{36}$, adding diffuse functions leads to an improvement in the accuracy of predictions for singlet transition energies as compared to the results obtained with the ECP basis sets. Therefore, further calculations on larger C-containing QDs were performed using the 6-31+G* basis set.

The performance of the selected ECP basis sets is variable. In all cases, LANL2DZ overestimates the transition energies predicted with all-electron basis sets, although for the larger SRLC basis set the values for $Ge_{35}H_{36}$ are in good agreement with those for 6-31G*, 6-31+G*, 6-31++G**, and def2-SVP. There remains some discrepancy in predictions for $Si_{35}H_{36}$, but the agreement

Table 2.2: Computed lowest four singlet transition energies ΔE/eV for $C_{35}H_{36}$, $Si_{35}H_{36}$, and $Ge_{35}H_{36}$ for a range of computational methods, using the TDA approach.

	ΔE/eV					
	6-31G*	6-31+G*	6-31++G**	def2-SVP	LANL2DZ	SRLC
$Ge_{35}H_{36}$	4.87	4.84	4.84	4.90	-	4.87
	5.03	5.00	5.00	4.90	5.20	5.04
	5.09	5.04	5.03	5.09	5.34	5.14
	5.17	5.12	5.10	5.20	5.41	5.25
$Si_{35}H_{36}$	5.17	5.19	5.18	5.16	5.42	5.54
	5.26	5.20	5.19	5.27	5.68	5.64
	5.28	5.39	5.38	5.30	5.78	5.70
	5.48	5.46	5.45	5.50	5.83	5.87
$C_{35}H_{36}$	8.17	6.45	6.30	7.62	6.08	8.14
	9.18	6.89	6.71	8.43	8.14	9.15
	9.47	7.23	7.06	8.80	9.13	9.49
	9.52	7.29	7.13	8.85	9.47	9.53

is sufficiently close to justify the use of the SRLC basis set in calculations for the larger Ge- and Si-containing QDs where the size difference between ECP and all-electron basis sets becomes significant (for the $Ge_{165}H_{100}$ cluster, the SRLC basis set employs 1520 basis functions compared to 5480 basis functions of the 6-31G* basis set). Additionally, a similar comparison was produced for the lowest singlet transition energies in functionalised $X_{35}H_{36}$ QDs with attached oxidised and reduced forms of dopamine. Calculated transition energies for the lowest four singlet states for functionalised $X_{35}H_{36}$ QDs are shown in Table 2.3 to support the above conclusion regarding the use of the SRLC basis for bigger systems.

Table 2.3: Calculated transition energies for the lowest four singlet states for functionalised $X_{35}H_{36}$ QDs with attached oxidised and reduced forms of dopamine for a range of computational methods. Asterisks by the energy values indicate oscillator strengths lower than 0.005.

	SRLC	6-31G*	def2-SVP	6-31+G*
$Ge_{35}H_{36}$+DOPox	2.11*	2.03*	2.01*	2.10*
	3.22*	3.13*	3.13*	3.16
	3.32	3.40	3.40	3.50
	3.37	3.73*	3.70*	3.50
	3.53	3.94	3.90	3.70
	3.57	4.00*	4.00	3.75*
$C_{35}H_{36}$ + DOPox	2.12*	2.05*	2.04*	2.07*
	3.14	3.15	3.16*	3.07
	3.24	3.20	3.22	3.15*
	3.51	3.73	3.67	3.54
	3.62	3.85	3.79	3.80
$Ge_{35}H_{36}$+ DOPox	2.13*	2.04*	2.04*	2.10*
	3.24	3.14*	3.14*	3.16*
	3.28	3.33	3.40	3.48
	4.13	4.37	4.30	3.50
$Ge_{35}H_{36}$+DOPred	4.22	4.27	4.31	-
	4.53	4.59	4.70	-
	4.75	4.80	4.90	-
	4.75	4.81	4.90	-
$C_{35}H_{36}$+DOPred	3.82*	3.87	3.87	3.89
	4.30	4.41	4.39	4.30
	4.76	4.94	4.93	4.90
	5.23	5.18	5.11	5.05
$Si_{35}H_{36}$+ DOPred	4.82	4.90	4.89	4.84
	5.00	5.11	4.94	4.84
	5.20	5.12	5.11	5.04*
	5.31	5.13	5.12*	5.04*

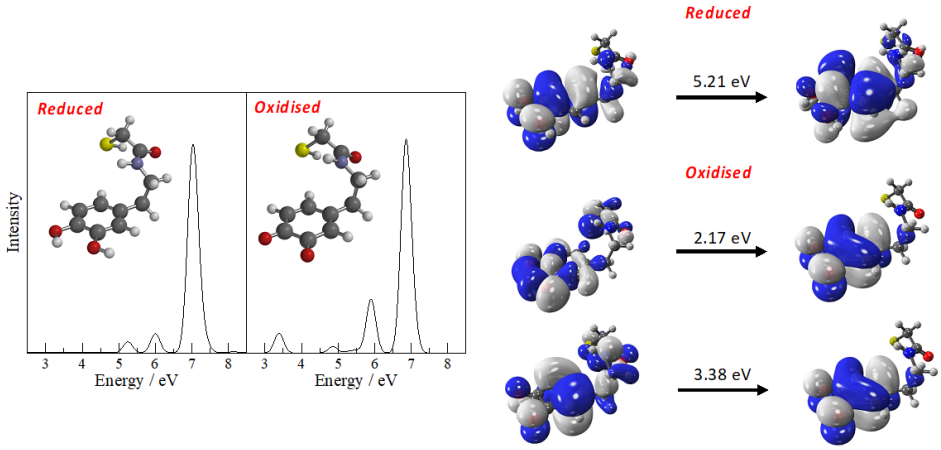


Figure 2.2: *Absorption spectra for oxidised and reduced form of dopamine with the linking group, and the orbitals associated with the lowest energy transitions (excitations below* 3 eV *are not visible).*

2.3 Characterisation of QDs and Dopamine

2.3.1 Dopamine Characterisation

Absorption spectra were generated by convoluting the calculated excitation and oscillator strengths with Gaussian functions with full-width half maximum of 0.3 eV. Figure 2.2 shows the computed TDDFT CAM-B3LYP/SRLC electronic spectra for the oxidised and reduced forms of dopamine. In these calculations the –(C=O)CHS– group used to attach dopamine to the quantum dot is included. The spectra reveal the critical difference between the two forms of dopamine where the lowest-energy transitions for the oxidized form are significantly ($\sim$ 3 eV) lower in energy compared to the reduced form. Figure 2.2 also shows the orbitals associated with the lowest energy transitions (an isovalue of 0.02 Å^{-3} was used to produce isodensity plots). It can be seen that these orbitals are predominantly on the dopamine part of the molecule, and consequently will be affected by the change from OH to =O substituents on the ring. For comparison, the absorption spectra and the excitation energies for dopamine with and without the inclusion of the linking group are included in

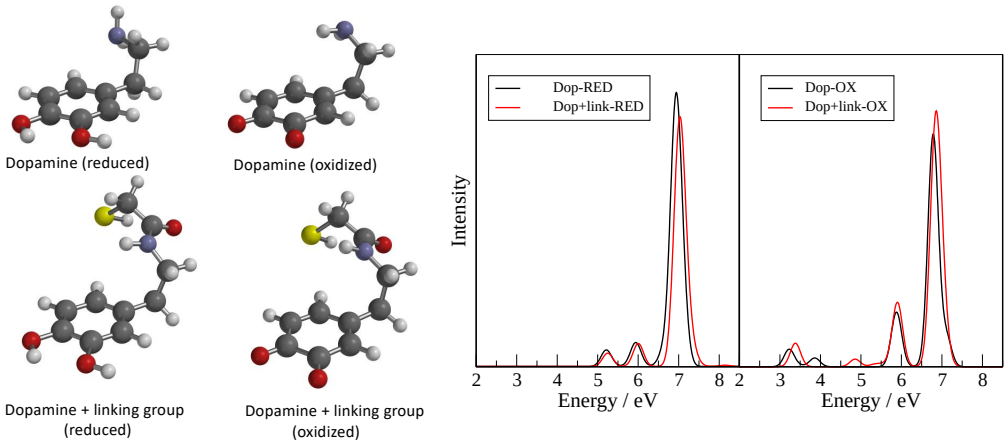


Figure 2.3: *The oxidised and reduced forms of dopamine with and without the linking group and corresponding absorption spectra.*

Figure 2.3. The results show that the lowest-energy transitions are associated with the dopamine part of the molecule, while the linking group contributes to the transitions at higher energy. In addition, Table 2.4 shows the calculated excitation energies with and without the TDA for dopamine with and without the linking group. These show that the introduction of the TDA does not have a noticeable effect on the calculated excitation energies and it was decided that this approximation would not be used in the subsequent analysis.

2.3.2 QD Characterisation

Table 2.5 summarises values for three important quantities, namely the HOMO-LUMO gap (ΔE_{HL}), the excitation energy for the lowest singlet state ($\Delta E_{\mathrm{S_1}}$), and (ΔE_{MAX}) which is the excitation energy for the most intense transition, within the energy range studied, calculated at the TDDFT CAM-B3LYP level of theory (SRLC basis set was used for Si- and Ge-based QDs, and 6-31+G* for C-containing QDs). For the largest clusters it was not possible to obtain values for ΔE_{MAX}. The results show that the excitation energy for the lowest singlet state decreases as the size of the cluster increases and this observation

Table 2.4: Calculated transition energies for the lowest 10 singlet states for oxidised and reduced forms of dopamine with and without the linking group using the TDDFT and TDDFT/TDA methods (CAM-B3LYP/SRLC).

	TDDFT	TDA		TDDFT	TDA
dopamineOX	2.17	2.20	dopamine+linkOX	2.17	2.20
	3.23	3.78		3.38	3.55
	3.53	3.57		3.53	3.62
	3.86	3.95		4.63	4.63
	5.88	5.96		4.86	4.87
	5.96	5.98		5.34	5.36
	6.29	6.29		5.56	5.56
	6.42	6.42		5.86	5.88
	6.58	6.59		5.90	5.98
	6.75	6.86		5.99	6.02
dopamineRED	5.24	5.34	dopamine+linkRED	5.30	5.20
	6.00	6.06		5.38	5.35
	6.06	6.24		5.87	5.85
	6.84	6.84		6.17	6.23
	6.92	6.97		6.23	6.63
	6.99	7.16		6.67	6.73
	7.09	7.19		6.74	6.90
	7.15	7.36		6.98	6.96
	7.26	7.54		7.04	7.00
	7.43	7.60		7.11	7.04

is consistent with previous studies.[119,125,126]

The value of the excitation energy for clusters of a similar size also decreases going from carbon → silicon → germanium, and there is a large difference between the carbon based QDs and the silicon and germanium ones. For example, for the $X_{84}H_{86}$ QD ΔE_{MAX} values of 6.3 eV, 4.8 eV and 4.3 eV are calculated for X = C, Si, and Ge, respectively. This difference is associated with a qualitative difference in the nature of the molecular orbitals for the carbon QDs as illustrated in Figure 2.4 which shows the molecular orbitals involved in the ΔE_{MAX} transitions. For all QDs the electron is being excited from an orbital associated with the σ bonding framework. The difference is

observed for the orbital receiving the electron, which in the case of $C_{84}H_{86}$ has the character of a Rydberg π orbital, whereas for the silicon and germanium QDs it has $\sigma/\sigma*$ type character.

Table 2.5: HOMO-LUMO gap ΔE_{HL}/eV, the excitation energy for the lowest singlet state ($\Delta E_{\mathrm{S_1}}$/eV), and excitation energy for the most intense transition (ΔE_{MAX}/eV) calculated using TDDFT CAM-B3LYP with SRLC basis set for Si- and Ge-based QDs and 6-31+G* basis set for C-containing QDs.

QD	ΔE_{HL}/eV	$\Delta E_{\mathrm{S_1}}$/eV	ΔE_{MAX}/eV
$C_{35}H_{36}$	8.4	6.4	7.2
$C_{84}H_{64}$	7.6	6.0	6.3
$C_{165}H_{100}$	7.2	5.8	-
$C_{286}H_{144}$	-	-	-
$C_{100}H_{60}$	7.8	6.2	6.3
$Si_{35}H_{36}$	7.7	5.5	5.6
$Si_{84}H_{64}$	6.6	4.7	4.8
$Si_{165}H_{100}$	6.0	4.3	4.5
$Si_{286}H_{144}$	5.5	4.0	-
$Si_{100}H_{60}$	5.9	4.1	5.0
$Si_{280}H_{120}$	5.1	3.6	-
$Ge_{35}H_{36}$	7.0	4.8	5.0
$Ge_{84}H_{64}$	6.0	4.1	4.3
$Ge_{165}H_{100}$	5.2	3.7	3.8
$Ge_{286}H_{144}$	4.7	3.3	-
$Ge_{100}H_{60}$	5.0	3.4	4.4
$Ge_{280}H_{120}$	4.4	2.9	-

Similar behaviour is also observed for the HOMO-LUMO gap, the values for the HOMO-LUMO gap presented here are significantly larger than those from previous works.[119,127–129] This reflects the nature of the CAM-B3LYP exchange-correlation functional compared with the B3LYP functional and other theoretical approaches. QDs can be compared with a particle in the box problem, and the band gap of the QD can be related to the simple expression for the energy difference between levels for a particle in the box. This suggests that as size L of a semiconductor QD increases to the corre-

sponding energy difference between levels decreases as $1/L^2$. The range of QD sizes considered in this work (1 – 3 nm) is too narrow for a meaningful analogy to be drawn. Takai *et al.*,[129] provided a simple phenomenological expression applicable to the estimation of the energy gaps at any given temperature in the 0 -– 600 K range, for a wide variety of QD sizes from very small QDs to bulk. The electronic structure of the octahedral diamond-like Si and Ge QDs converges toward the corresponding cubic bulk materials as their structure can be superimposed with cubic bulk lattice (octahedral QDs can be considered as finite hydrogenated clusters cut from cubic bulk lattices of silicon and germanium). However, the icosahedral shapes possess slightly different electronic characteristics. Because the icosahedral QD structures are not superimposable with the cubic bulk lattice of Si or Ge, their structures can be considered to approach icosahedral quasicrystals.[130] This suggests that the electronic characteristics of the icosahedral QDs could be different from the cubic bulk material, as suggested previously for icosahedral silicon quantum dots.[131] For carbon QDs, the band gap values converge towards that of diamond. The results show that the HOMO-LUMO gap provides a relatively poor estimate of the excitation energy for the lowest energy state indicating that going beyond KS DFT based molecular orbital picture maybe necessary for a reliable description of the photophysical mechanisms. Since the QDs will fluoresce from the S_1 state, the results show that a wide range of fluorescent energies are possible by tuning the size and composition of the QD.

2.3.3 Dopamine Attachment to QDs

The geometry optimisation of smaller, dopamine functionalised $X_{35}H_{36}$ QDs was initially tested using B3LYP DFT and a range of basis sets including 6-31G, 6-31G*, and def2-SVP (Table 2.6). The calculated energy values are shown to be insensitive to the choice of basis set, and def2-SVP is used in the

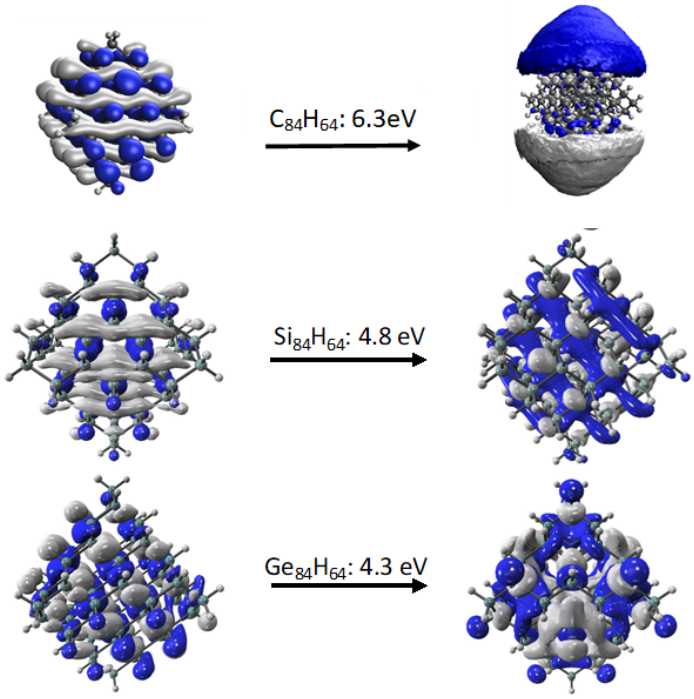


Figure 2.4: *Molecular orbitals associated with intense transitions for $X_{84}H_{64}$ QDs.*

subsequent analysis of the bigger QDs to obtain the binding energy corresponding to the attachment of dopamine at different sites on the QD surface. This computational setup has been used previously[119] to study the structure and electronic properties of hydrogenated carbon, silicon and germanium clusters.

Figure 2.5 gives a schematic representation of a diamond-like $X_{84}H_{64}$ QD structure, in two different orientations as shown in 4(a) and 4(b), where terminating hydrogen atoms are coloured to distinguish symmetry-equivalent groups. Five distinct adsorption sites (A1 – A5) on the surface of the $Ge_{84}H_{64}$ QD were compared to confirm that the corresponding binding energies are the same for all five sites (Table 2.7).

This conclusion might have important implications on the experimental realisation of a QD-based fluorescent sensor, giving a flexibility in its design where dopamine molecule does not need to be attached to a specific binding site. It is important to mention that in QDs with icosahedral structure (Figure 2.1) all adsorption sites are identical.

Table 2.6: Calculated energies (in Hartree) for functionalised $X_{35}H_{36}$ QDs with attached oxidised and reduced forms of dopamine using DFT and 6-31G, 6-31G*, and def2-SVP basis sets level of theory.

	6-31G	6-31G*	def2-SVP
$Si_{35}H_{36}$ – DOPox	−11218.5634	−11219.5486	−11216.3467
$C_{35}H_{36}$ – DOPox	−2459.2719	−2459.8553	−2458.2843
$Ge_{35}H_{36}$ – DOPox	−73771.9074	−73774.6624	−73774.6957
$Si_{35}H_{36}$ – DOPred	−11219.8115	−11220.7887	−11217.5976
$C_{35}H_{36}$ – DOPred	−2460.5176	−2461.0932	−2459.5345
$Ge_{35}H_{36}$ – DOPred	−73773.1590	−73775.9054	−73775.9500

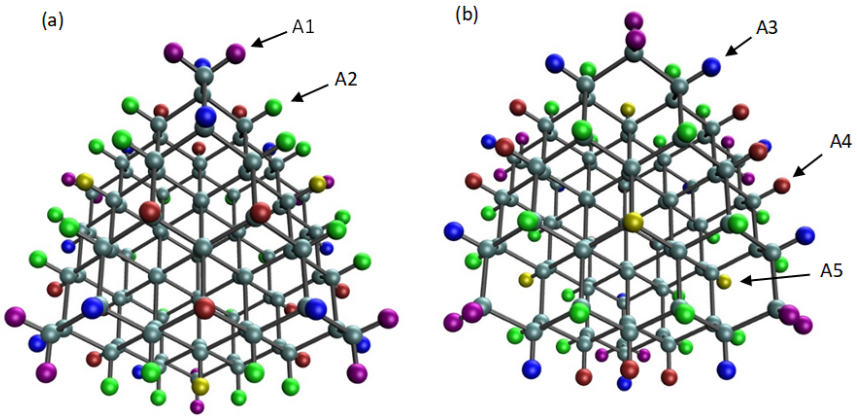


Figure 2.5: *The $X_{84}H_{64}$ system with atom coloured based on their symmetry-equivalent groups.*

2.4 QD-Based Fluorescent Probes

2.4.1 Molecular Orbital Energy Analysis

Based upon the electronic structure calculations characterising the QDs and dopamine we now explore whether these QDs are suitable to act as the fluorophore in a QD-based fluorescent probe that operates using a PET mechanism. A schematic of this mechanism is shown in Figure 2.6 which also illustrates how both oxidative and reductive PET mechanisms can occur. The QD undergoes an initial excitation that can lead directly or indirectly via non-

Table 2.7: Binding energies (in Hartree) in a dopamine functionalised $Ge_{84}H_{64}$ QD, calculated at B3LYP/def2-SVP level of theory.

H atom replaced with DOP	QD+DOPox	QD+DOPred
A1	−175555.9062	−175557.1558
A2	−175555.9119	−175557.1528
A3	−175555.9039	−175557.1517
A4	−175555.9067	−175557.1584
A5	−175555.9035	−175557.1498

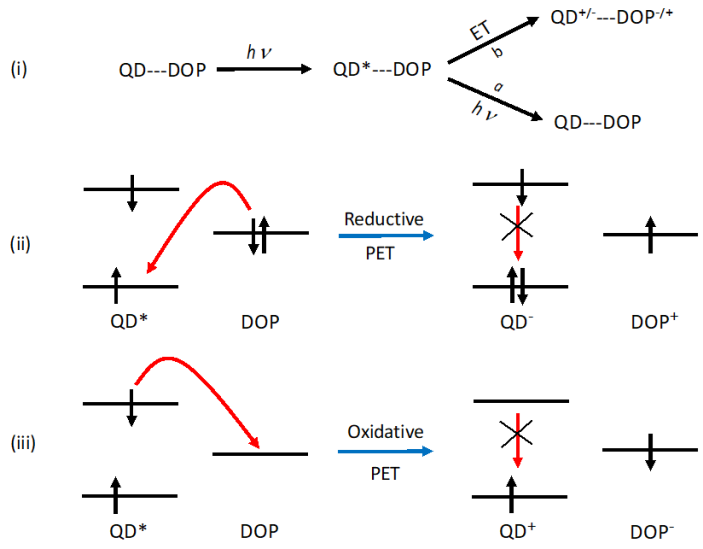


Figure 2.6: *Schematic of the PET mechanism (i), with an illustration of the electronic transitions for (ii) reductive PET and (iii) oxidative PET.*

radiative processes to the S_1 state of the QD from which fluorescence can occur, as denoted by path a. However, several other photophysical processes may be possible. For example, if dopamine has occupied orbitals that lie higher in energy than the singly occupied orbital of the QD, an electron can transfer from dopamine to the QD in a reductive PET process (the QD is reduced) which has the effect of quenching the fluorescence. Alternatively, if dopamine has unoccupied orbitals lower in energy than the singly occupied orbital of the QD, electron transfer from the QD to dopamine can occur in oxidative PET, which again leads to a quenching of the fluorescence.

In the design of a QD sensor there are several factors to consider. Firstly, it is desirable for the absorption and emission bands of the QD not to overlap with the transitions of dopamine. The spectra in Figure 2.2 show the region 3.75 eV to 4.5 eV is suitable, and the calculated transition energies shown earlier indicate that the $Si_{165}H_{100}$ and $Ge_{84}H_{64}$ QDs would satisfy this condition, while none of the carbon based QDs studied are suitable. Secondly, it is required that PET mechanism occurs leading to quenching of the fluorescence for one form of dopamine and not the other. Initially it is convenient to examine the molecular orbital diagrams. Figure 2.7 illustrates the energy difference between the molecular orbitals of $Ge_{84}H_{64}$ and $Si_{165}H_{100}$ QDs and the reduced and oxidised forms of dopamine. Analysis of these energies suggests that for $Ge_{84}H_{64}$ and $Si_{165}H_{100}$ QDs oxidative PET would occur for the oxidised form of dopamine but not the reduced form. Consequently, quenching of the fluorescence for the oxidised form of dopamine would be predicted, while the reduced form would continue to fluoresce. This would be consistent with the experimental operation of the biosensor in the original work.[84] These two QDs are not the only two QDs that fulfil these criteria, others that this level of analysis would predict to be suitable fluorophores include $Si_{100}H_{60}$ and $Ge_{100}H_{60}$.

2.4.2 Analysis Based on Excited States of QD-Dopamine Systems

Analysis of the photophysical behaviour based purely on an orbital energy analysis can be unreliable since differences in orbital energies can provide a poor estimate of the relative energies of the excited states. Going beyond this level of analysis requires explicit consideration of the excited states of the combined QD-dopamine system. Figure 2.8 shows that optimised structures for the oxidised and reduced forms of dopamine on the $Ge_{84}H_{64}$ QD ($Ge_{84}H_{64}$-DOPox and $Ge_{84}H_{64}$-DOPred) along with the calculated absorption spectrum.

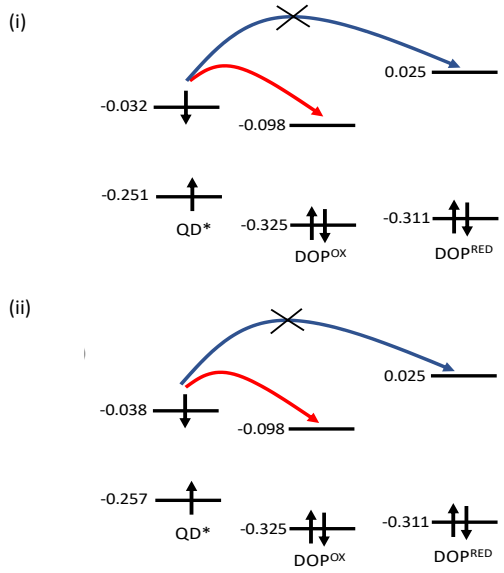


Figure 2.7: *Molecular orbital diagrams showing the HOMO and LUMO energies (in Hartree) based upon the ground state CAM-B3LYP/SRLC calculation for the $Ge_{84}H_{64}$ and $Si_{165}H_{100}$ QDs and the reduced and oxidised forms of dopamine.*

The spectra are dominated by the transitions localised on the QD (QD → QD transitions), the exception is the peak at about 3.25 eV for the oxidised form which corresponds to a transition localised on dopamine (DOP → DOP transition). However, the absorption spectra do not reveal the CT transitions that underpin the sensing mechanism since these will have low oscillator strength. Table 2.8 shows the low energy transitions along with a characterisation of the nature of the transition. The 3-D visualization of the ground state and excited state molecular orbitals contributing to different optical transitions in vacuum are shown in Figure 2.9. For the reduced form of dopamine, all the low energy states correspond to QD → QD transitions indicating lack of possibility of forming a state where an electron has been transferred from QD to dopamine that will have lower energy than the S_1 state formed through excitation on the QD. However, for the oxidised form there are several QD → DOP transitions that lie at lower energy than the QD → QD transitions, the final state arising from these transitions is consistent with the final state that would arise from the oxidative PET mechanism. These results are consistent with molecular orbital energy-based analysis. This approach to determine the occurrence of

Table 2.8: Transition energies and assignments for the dopamine functionalised $Ge_{84}H_{64}$ QD calculated at CAM-B3LYP/SRLC level of theory.

	ΔE/eV	Nature of the transition	Oscillator strength
$Ge_{84}H_{86}$-DOPred	3.93	QD to QD	0.0186
	4.13	QD to QD	0.0114
	4.13	QD to QD	0.0006
	4.15	QD to QD	0.0001
	4.17	QD to QD	0.0020
	4.18	QD to QD	0.0035
	4.18	QD to QD	0.0250
	4.20	QD to QD	0.0010
	4.24	QD to QD	0.0020
	4.25	QD to QD	0.0175
$Ge_{84}H_{86}$-DOPox	2.12	DOP to DOP	0.0000
	3.24	DOP to DOP	0.0118
	3.25	DOP to DOP	0.0320
	3.67	QD to DOP	0.0001
	3.71	QD to DOP	0.0002
	3.73	QD to DOP	0.0005
	3.84	QD to DOP	0.0000
	3.84	QD to DOP	0.0000
	3.86	QD to DOP	0.0000
	3.94	QD to QD	0.0156

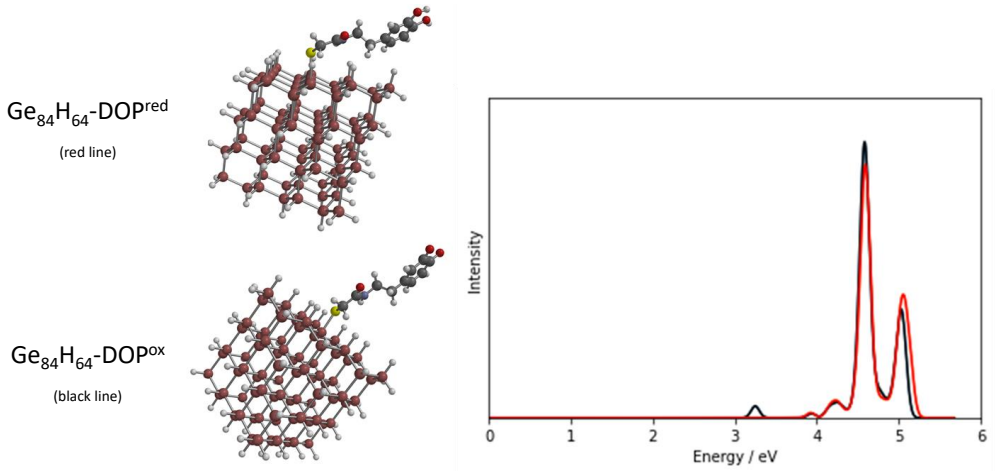


Figure 2.8: *Optimised structures of the two forms of dopamine on a $Ge_{84}H_{64}$ QD and computed CAM-B3LYP/SRLC spectra for $Ge_{84}H_{64}$-DOPred (red line) and $Ge_{84}H_{64}$-DOPox (black line).*

PET is based purely on energetic considerations. There are other factors that will determine the efficiency of these processes occurring, such as the rates of surface crossing. While it is possible to take them into consideration,[132] such calculations are much more computationally demanding to be applied on a routine basis.

2.5 Solvent Inclusion

So far, the analysis presented has been based upon gas-phase calculations with no account of solvent. While the energetics of the QD surface can be significantly affected not only by ligands on the surface, but also the solvent surrounding the QD. The molecules of the solvent can attach to the surface of QDs and form a thin film which can be considered as weakly binding ligands. This effect might depend more or less on the polarity of the solvent and is expected to be more pronounced for solvents with a lone electron pair, like acetonitrile or propylene carbonate.[133] It has been reported in literature that the dielectric constant of the solvent does have an effect on the charge distribution over the surface of QD.[134] The inclusion of solvent has been shown

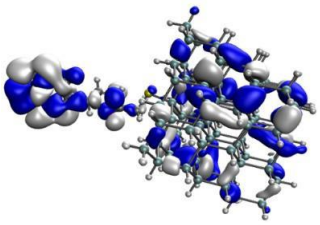
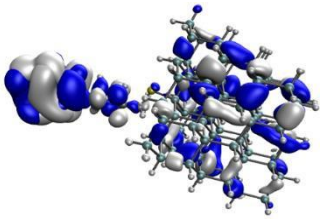
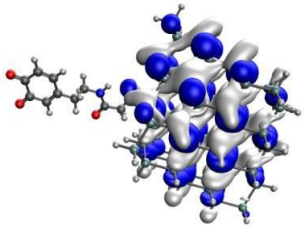
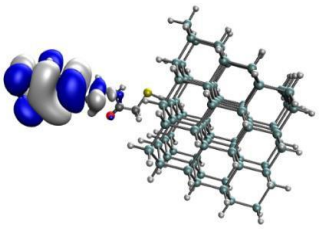
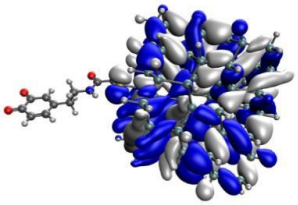
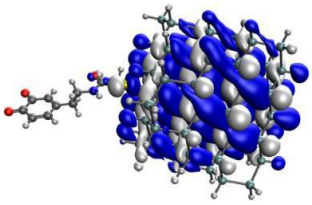
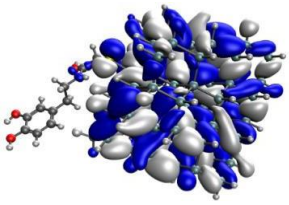
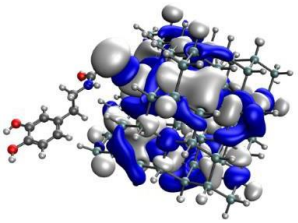
ΔE / eV	Transition	Occupied orbitals involved in transition	Virtual orbitals involved in transition
2.12	DOP → DOP^{ox}		
3.67	QD → DOP^{ox}		
3.94	QD → QD for $Ge_{84}H_{86}$-DOP^{ox}		
3.93	QD → QD for $Ge_{84}H_{86}$ - DOP^{red}		

Figure 2.9: *Molecular orbitals (with the highest amplitudes) involved in the transition for functionalised $Ge_{84}H_{64}$-DOP in vacuum.*

to be important, particularly for sensing of metal ions.[105] PET leads to the formation of $QD^{+/-} - DOP^{+/-}$ species, which will interact more strongly with a polar solvent that the states formed from local QD → QD or DOP → DOP transitions. Consequently, the states formed from QD to DOP transitions are likely to become relatively lower in energy.

Table 2.9 shows the excitation energies and character of the transitions for the $Ge_{84}H_{64}$-DOP system calculated using a polarised continuum solvent model (PCM) with a dielectric constant of 80 corresponding to bulk water. The 3-D visualization of the ground state and excited state molecular orbitals contributing to different optical transitions in solvent are shown in Figure 2.10. For the oxidised form of dopamine ($Ge_{84}H_{64}$-DOPox), there is clear evidence that the energies of states formed from QD → DOP transitions have been lowered in energy and these transitions dominate the lowest energy states except for the lowest energy DOP → DOP transition. For the reduced form of dopamine ($Ge_{84}H_{64}$-DOPred), the introduction of solvent does not have a significant effect on the low energy states, which are dominated by QD → QD transitions, and, interestingly the transition energies for these states show a very small change with the introduction of solvent. Overall, the predicted function of the QD in as sensor is not altered by the solvent, and the presence of additional charge-transfer (CT) type transitions for the oxidised form would enhance its effectiveness.

2.6 Conclusion

The use of DFT-based calculations to characterise QDs and to select suitable QDs for a sensing applications has been explored within the context of a sensor to differentiate between two forms of dopamine. TDDFT calculations of hydrogenated carbon, silicon and germanium QDs show that the band gap and

Table 2.9: Transition energies and assignments for the dopamine functionalised $Ge_{84}H_{64}$ QD with the PCM solvent model calculated at CAM-B3LYP/SRLC level of theory.

	ΔE/eV	Nature of the transition	Oscillator strength
$Ge_{84}H_{86}$-DOPred	3.92	QD to QD	0.0400
	4.09	QD to QD	0.0312
	4.13	QD to QD	0.0023
	4.14	QD to QD	0.0000
	4.16	QD to QD	0.0090
	4.17	QD to QD	0.0030
	4.17	QD to QD	0.0053
	4.18	QD to QD	0.0011
	4.19	QD to QD	0.0008
	4.20	QD to QD	0.0022
$Ge_{84}H_{86}$-DOPox	2.34	DOP to DOP	0.0001
	2.84	QD to DOP	0.0402
	3.16	QD to DOP	0.0001
	3.20	QD to DOP	0.0002
	3.22	QD to DOP	0.0005
	3.31	QD to DOP	0.0000
	3.32	QD to DOP	0.0000
	3.34	QD to DOP	0.0000
	3.51	QD to DOP	0.0004
	3.56	QD to DOP	0.0000

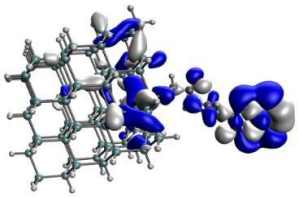
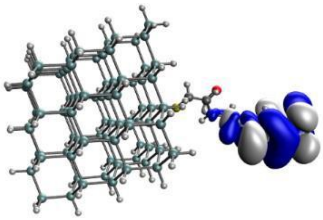
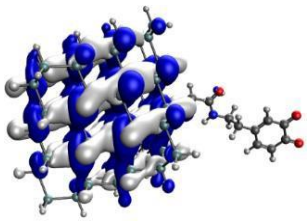
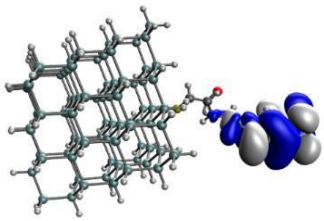
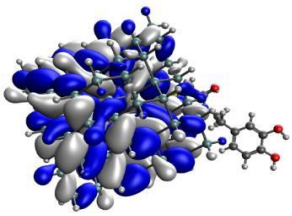
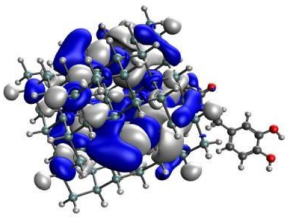
ΔE / eV	Transition	Occupied orbitals involved in transition	Virtual orbitals involved in transition
2.34	DOP → DOP^{ox}		
3.20	QD → DOP^{ox}		
3.92	QD → QD for $Ge_{84}H_{86}$-DOP^{ox}		

Figure 2.10: *Molecular orbitals (with the highest amplitudes) involved in the transition for functionalised $Ge_{84}H_{64}$ in solvent.*

fluorescence energies of these QDs varies with size and composition allowing for the possibility of tuning the QDs for a specific application. Additionally, it was shown that the lowest energy excited singlet states are significantly lower in energy for the oxidised form compared with the reduced form of dopamine. This factor is significant when considering the design of a fluorescence dopamine functionalised QD sensor. Through an analysis of orbital diagrams and calculations of the excited states of the combined QD-DOP system, it was demonstrated that a sensor could operate based upon a PET mechanism that would occur for the oxidised form of dopamine and not the reduced form. This is evident from low energy states arising from QD $\rightarrow$ dopamine transitions that are present for the oxidised form of dopamine. This leads to a quenching of the fluorescence for the oxidised form, allowing the two forms to be distinguished. It was shown that $Ge_{84}H_{64}$ and $Si_{165}H_{100}$ QDs satisfy the criteria that would make then suitable candidates for the fluorophore in a sensor. Overall, the study highlights how quantum chemical calculations can be used to inform the photophysical processes underpinning the operation of fluorescent probes and presents an approach to support the design of QD based optical sensors for the detection of biomolecules.

Chapter 3

Super Atomic Molecular Orbitals of Endohedral Fullerenes

3.1 Introduction

Fullerenes are easy-to-synthesise, high symmetry allotropes of carbon that can adopt various sizes of a characteristic cage structure. Among various fullerene sizes, C_{60} has been found to be the smallest stable, most abundant fullerene which satisfies the isolated pentagon rule (twelve pentagons surrounded exclusively by hexagons, providing good stability to the structure).[135] The cage structures of fullerenes are characterised by high number of π-electrons, and large polarizability, which makes them a good electron acceptor. One of the most important properties of fullerenes is their ability to capture both individual atoms and small clusters, which has resulted in the creation of novel and potentially beneficial electronic properties for science and innovations.[136–138] This, in turn, has led to a wide range of potential applications such as solar cells, sensors, drug delivery and energy storage.[139–142] In addition to that they

are ideal candidates for probing the electronic and dynamical properties of nanomaterials, allowing the possibility to gain a deeper understanding of how such systems behave under different experimental conditions.

The electronic structure of fullerenes has been the subject of theoretical and experimental investigations, revealing an interesting property of those molecules. In 2 Photon Polymerisation (2PP) and Low Temperature Scanning Tunneling Microscopy (LT-STM) measurements,[143] a number of molecular orbitals that have the appearance of atomic molecular orbitals were observed and later called super atom molecular orbitals (SAMO). SAMOs are diffuse electronic levels of the excited states of fullerenes. They resemble low-lying Rydberg states in electron distribution, except the electron density of SAMOs is located much closer to the centre of the hollow cage of C_{60} when compared to low-lying Rydberg states. Because of the characteristic shape, SAMOs are comparable to diffuse s-, p- and *d* - hydrogenic atomic orbitals. The delocalised character of SAMOs opens the possibility for hybridisation of these orbitals. Consequently, when bringing C_{60} molecules close enough (within 1.0 nm van der Waals distance) hybridisation of SAMOs into s-electron metal-like nearly free electron (NFE) bands can take place.[144] The observation of NFE bands in empty states of C_{60} suggests that the transport properties of fullerenes can be enhanced, and it represents a significant development in their potential role in the advancement of the field of molecular electronics. However, the high energy level of the C_{60} SAMOs compared to the Fermi level currently limits their practical application.[145,146] Various methods have been proposed to lower the energy of SAMOs in fullerenes such as endohedral doping[144] and fullerene absorption on various substrates.[145–147] However more investigation of SAMOs in various fullerene combinations are required.

Experimentally, the SAMOs of C_{60} and endohedral C_{60} in both gas phase and on the substrate have been observed by several research groups. They have used various spectroscopic techniques such as femtosecond photoelectron spec-

troscopy, low-temperature ultrahigh-vacuum scanning tunnel microscopy, and two-photon photoemission experiments to observe SAMOs in fullerenes.[143,148] Alongside experimental work, computational studies can also aid in understanding the intrinsic physical properties of fullerenes, including their SAMOs characterisation, charge transfer properties, and design considerations for practical applications of fullerenes. There have been number of works carried out that have used *ab initio* calculations, HF, DFT, and TDDFT to study the properties of fullerenes.[149–162] Most of those studies focused on investigating the electronic structure of endohedral fullerenes (doped with various atoms), but there have been fewer studies specifically focusing on SAMOs in C_{60}. *Ab initio* calculations have been used for fullerenes doped with Si, Ge, and Al atoms.[149] Semi-empirical and DFT methods were used for the investigation the stability of C_{60} isomers and C_{60} doped with Sc, Y, and K atoms.[149–152] DFT calculations were used for exploring the Li storage capacity of endohedral C_{60} fullerenes doped with noble gases, as well investigating catalytic properties for hydrogen evaluation of C_{60} doped with alkali metals,[153–155] including Li doped fullerenes for the application of molecular electronics.[156–159] HF was used to investigate the effect of the position of F^-, Ne, Na^+, Mg^{2+}, inside the C_{60} endohedral fullerenes on the stability and radius of the whole structure.[160–164] While DFT and second-order Møller Plesset perturbation (MP2) methods were used to investigate the formation mechanism of endohedral fullerenes, their most stable geometries and binding energies.[144,165–168] Theoretical studies that specifically focus on SAMOs used plane-wave DFT to characterise the one-electron SAMOs orbitals in C_{60} and C_{60} doped with alkali and noble metal atoms.[143,144] A many-body perturbative approach was used for investigating the stability of SAMOs states in C_{60}.[169] The TDDFT approach was utilised to calculate photoelectron spectra and investigate both photoionization of SAMOs and Rydberg states of C_{60}.[170–172]

More research investigating SAMOs could provide insights into the design

of novel advanced materials for molecular electronics. These materials would be expected to be based on SAMO-mediated electron transport if the excitation energy of SAMOs could be lowered. So far, SAMOs of isolated endohedral C_{60} molecules or those adsorbed on the metal surface have been rather broadly studied, while the effect of functionalisation of C_{60} on SAMOs distribution and energies were not much characterized. The presence of various ligands and functional groups on the surface of C_{60} molecules can greatly enhance their importance in practical applications. It is therefore interesting to check whether the attachment of other atoms on the surface will change the electronic properties and energies of SAMOs of fullerenes. This work uses DFT and TDDFT calculations to find and characterise SAMOs of C_{60}, Li@C_{60}, and Ca@C_{60} with and without hydrogen on the C_{60} surface, and investigates the effect of hydrogen on the shape and the energy of SAMOs within the studied systems.

3.2 Evaluation of Computational Methods

The structures of the studied fullerenes were optimised using DFT with three different functionals (B3LYP, B3P86, PBE) and basis sets (6-31G*, 6-311G**, 6-31++G**). In this work, two types of endohedral fullerenes were studied Li@C_{60} and Ca@C_{60} with and without hydrogen atoms on the surface. The excited states of the molecules were computed using TDDFT with the B3LYP functional and 6-31++G** basis set. All calculations were performed using the Q-Chem software package.[120] Visualisation of the orbitals (using an isosurface threshold of 0.02) was performed with IQmol software.

First, a ground state electronic structure calculations for isolated C_{60} molecules using DFT method were performed. Three different functionals (B3LYP, B3P86, PBE) and basis sets (6-31G*, 6-311G**, 6-31++G**) were

compared and the results are shown in Table 3.1. As can be seen, the choice of functional affects the value of HOMO-LUMO gap. The significant difference has been observed in the energy values when comparing B3LYP and B3P86 with PBE. The energy for PBE is much lower than for the others. With the 6-31++G** basis set the HOMO-LUMO energy gap for B3LYP and B3P86 is 2.73 eV, while for PBE is 1.65 eV. Published experimental results show the HOMO-LUMO gap for C_{60} to be around 1.5 eV when high resolution photoelectron spectroscopy experiment was carried out..[173,174] However, using photoemission-inverse-photoemission experiments the HOMO-LUMO gap for C_{60} was found to be 2.5 eV.[175,176] The value close to 2.5 eV was further confirmed by Lof *et al.*, through a precise measurement considering Frenkel-type excitons.[177] The theoretical values reported in the literature also vary and depend on the used methods. Using B3LYP/6-311G* the calculated HOMO-LUMO gap in C_{60} was predicted to be 2.73 eV,[178] using the PBE/6-311G** level of theory, it was predicted to be 1.65 eV,[178] and with local density approximation (LDA) it was predicted to be 1.5 eV. Discrepancy in the results could come from different approaches in the experimental techniques, and the various nature of functionals and basis sets. Our calculated values with the B3LYP and B3P86 functionals are close to that obtained experimentally by Lof *et al.*, (2.5 eV) using photoemission-inverse-photoemission experiments and theoretically by Wang *et al.*, (2.73 eV) using B3LYP/6-311G*.[178] While PBE predicted HOMO-LUMO values close to the other research groups (1.5 eV).[178]

Experimentally, when the HOMO-LUMO gap is deduced from the photoexcitation spectrum, the lowest energy dipole-allowed transition (optical gap) is measured. This optical gap is always smaller in energy than the fundamental gap (in the molecular case, the difference between the first ionization energy and the electron affinity) due to the Coulomb interaction between the excited electron and the hole left behind after its excitation.[179,180] As a result, a precise measurement of the photoexcitation energy does not necessarily corre-

late quantitatively with an exact estimate of the fundamental gap. In addition, if the measured sample is not in pristine conditions, then the presence of any defects on the sample can affect the HOMO-LUMO gap.[181] At the computational level, it is well known that the KS HOMO–LUMO gap is much below the ionization-affinitiy difference. This is due to the fundamental difference that the KS system has an attractive potential due to the exchange–correlation hole of -1 electron also for the virtual levels.[182] The calculated HOMO-LUMO gap only approximates the fundamental gap and the quality of that approximation is highly dependent on the nature of the exchange-correlation functional and the amount of HF exchange it includes. Therefore some discrepancy between experimental and theoretical results will be always expected.

Interestingly, the values for the LUMO-SAMO gap are not affected by the choice of functional, instead the effect is significant for using different basis sets. Adding diffuse function leads to an improvement in the accuracy of predictions for LUMO-SAMO energies as compared to the results obtained with the basis sets without it. LUMO-SAMO gaps found in literature were calculated using plane wave DFT methods and reported to be for the LUMO-*s*-SAMO 2.95 eV and for the LUMO-*p*-SAMO 3.95 eV.[147] In this work, for all studied functionals, the result show that using 6-31++G** calculations for the LUMO-SAMO energy value agree with the reported data. This could be because of the electron distribution in SAMO orbitals, and to be able correctly describe them diffuse functions are required which more accurately represent the part of the orbitals located much more distant from the atomic nuclei. Therefore, further calculations on endohedral fullerenes and functional fullerenes were performed using the 6-31++G** basis set and B3LYP functional.

Table 3.1: The HOMO-LUMO(Δ_{HL}) and LUMO-SAMO (Δ_{LS}) gaps (in eV); and Total Energy (in Hartree) for C_{60} calculated using various functionals and basis sets.

Structure	Functional	Basis set	Total Energy	Δ_{HL}	Δ_{LS}
C_{60}	B3P86	6-31G*	−2286.8888	2.76	$s = 15.8\,eV$
					$p = 16.6\,eV$
					$d = 17.0\,eV$
C_{60}	B3P86	6-311G**	−2287.2846	2.74	-
C_{60}	B3P86	6-31++G**	−2286.9261	2.73	$s = 3.6\,eV$
					$p = 4.6\,eV$
					$d = 5.2\,eV$
C_{60}	B3LYP	6-31G*	−2286.0176	2.76	$s = 15.7\,eV$
					$p = 16.2\,eV$
					$d = 17.0\,eV$
C_{60}	B3LYP	6-311G**	−2286.5884	2.74	-
C_{60}	B3LYP	6-31++G**	−2286.2204	2.73	$s = 3.3\,eV$
					$p = 4.2\,eV$
					$d = 4.7\,eV$
C_{60}	PBE	6-31G*	−2283.5947	1.67	-
C_{60}	PBE	6-311G**	−2283.9915	1.66	-
C_{60}	PBE	6-31++G**	−2283.6394	1.65	$s = 3.1\,eV$
					$p = 4.4\,eV$
					$d = 4.9\,eV$

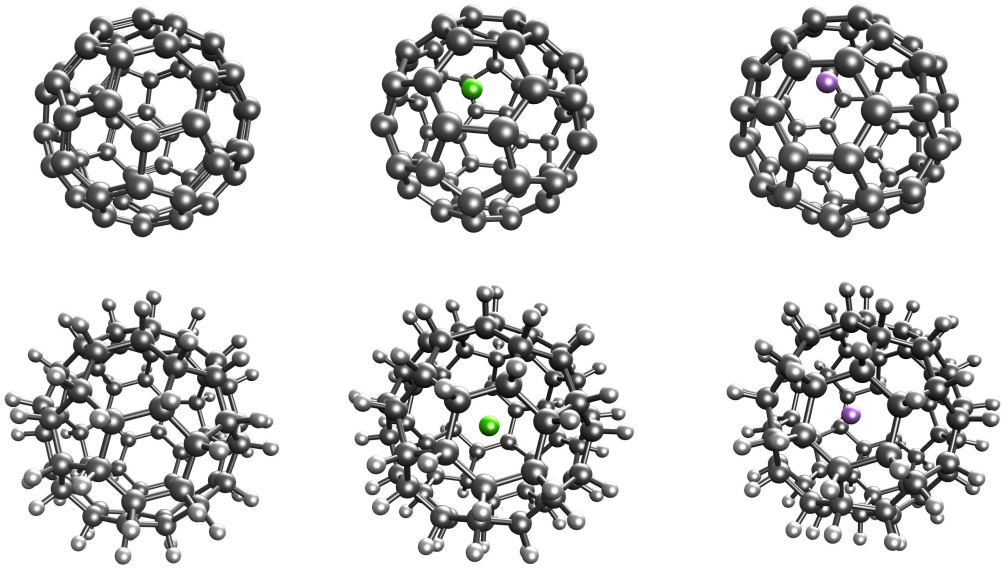


Figure 3.1: *Optimised structures of empty C_{60} (top left) with Ca (green) and Li (purple) atoms inside the cage, and hydrogenated C_{60} (bottom left) with Ca (green) and Li (purple) atoms, calculated using DFT/B3LYP/6-31++G** level of theory.*

3.3 Characterisation of $Li@C_{60}$ and $Ca@C_{60}$

The geometry of hydrogenated endohedral fullerenes was optimised using the DFT/B3LYP/6-31++G** level of theory. It has been reported that the presence of Li atom inside the C_{60} cage influences its electronic structure. Moreover, it was demonstrated that the position of the atom inside the cage could be changed using the STM technique via an inelastic scattering mechanism, and the SAMOs were shown to be affected by that position.[183] In this study a single position of the metal atom was considered. The Li and Ca atoms were initially placed in the centre position inside the cage, and then the structures were optimised. Figure 3.1 shows the relaxed geometry of the endohedral fullerenes, and the bond length for pure endohedral fullerenes ($Ca@C_{60}$ and $Li@C_{60}$), and functionalised (hydrogenated) endohedral fullerenes ($Ca@C_{60}H_{60}$ and $Li@C_{60}H_{60}$). As can be seen, the metallic atoms (Li and Ca) occupy the centre position in case of hydrogenated fullerenes while for the pure fullerenes they are located slightly off-centre of the cage. It can be seen in Figure 3.1 fullerenes adopt a form of a closed cage consisting of twelve pentagons and 20

Table 3.2: Bond length (in Å) and distance (in Å) of encapsulated atom (in Å) from a cage for studied fullerenes. M = Ca, Li.

	C–C (pentagon)	C–C (hexagon)	C–M (shortest)
C_{60}	1.45	1.40	-
Ca@C_{60}	1.45	1.40	2.43
Li@C_{60}	1.45	1.40	2.10
$C_{60}H_{60}$	1.57	1.56	-
Ca@$C_{60}H_{60}$	1.57	1.56	Centre
Li@$C_{60}H_{60}$	1.57	1.56	Centre

hexagons with two types of bonds: short double bonds between the hexagons and longer single bonds between the pentagons. As shown in Table 3.2 the atom inside the cage does not affect the bond length, however, the presence of the hydrogen on the surface does. It is determined in this study that the bond length of the hexagon-pentagon for C_{60} with and without metal atom inside the fullerene cage is approximately 1.45 Å, while the hexagon-hexagon bond is 1.40 Å long. The results agree with the neutron diffraction measurements,[184] where the respective bonds were found to be 1.46 Å and 1.39 Å. The calculated values are similar to the length of C–C bond found in diamond (1.52 Å) and graphite (1.42 Å), which can suggest comparable behaviour of fullerenes to the other carbon-based compounds. For the hydrogenated fullerenes the bond length increased and is found to be approximately 1.57 Å and 1.56 Å for hexagon-pentagon, and hexagon-hexagon respectively, for all with and without metal atom within the hydrogenated fullerenes. This could be because C=C double bonds are transformed into single bonds as a result of the attachment of the hydrogens to the surface of the C_{60} cage.

The study of the electronic structure of C_{60} molecules demonstrated, among other properties, that highly degenerate valence states of C_{60} consist of the σ

orbitals bound to carbon atoms and above them π. Using LT-STM the bonding and antibonding HOMO and LUMO orbitals were resolved.[185–187] Using scanning tunneling microscopy SAMO orbitals were observed.[143] The shape of the orbitals can be also reproduced using computational studies. In Figures 3.2, 3.3, and 3.4 HOMO and LUMOs orbitals (within the first 200 states) of the C_{60}, $Ca@C_{60}$, and $Li@C_{60}$ are shown. For C_{60} (Figure 3.2) the HOMO and LUMO orbitals look like typical sp^2 hybridised orbitals of the C atom. From LUMO+14 the orbitals shape starts to resemble the SAMOs shape. LUMO+14 looks like an *s*-SAMO while LUMO+20, +21, and +22 have an apperance of *p*-SAMOs type. From LUMO+28 to LUMO+32 the orbitals are similar to *d*-SAMOs. However, all of the observed SAMOs orbitals in C_{60} are well above LUMO. Figure 3.3 shows SAMOs orbitals calculated for $Ca@C_{60}$. It can be seen that the the HOMO and LUMO are the sp^2 type orbitals while LUMO+5 and and LUMO+14 could be considered to closely resemble SAMOs orbitals. There were no other SAMOs orbitals observed within the first LUMO+200 states. Figure 3.4 presents SAMOs observed for $Li@C_{60}$. As can be seen the presence of Li atom also affects the electronic structure of C_{60}. The HOMO orbitals and the first virtual LUMO have their electronic density centred close to the carbon atoms. However, higher lying orbitals look like *s*-SAMOs (LUMO+5), and *p*-SAMOs (LUMO+14, +15 and +16) atomic orbitals that are located in the middle of the C_{60} cage and these can be considered as SAMOs.

The potential practical applications of the SAMO properties of fullerenes are limited by the existence of the LUMO states below SAMOs. The lowest energy of *s*-SAMO was calculated and reported to be 3.28 eV above the LUMO for C_{60}.[147] However, if the SAMO orbitals could be stabilized to below the LUMO states, then the application of materials with the SAMO-based charge transport properties could be important, especially for molecular electronics. Therefore, the HOMO-LUMO and LUMO-SAMO energy differences for pure

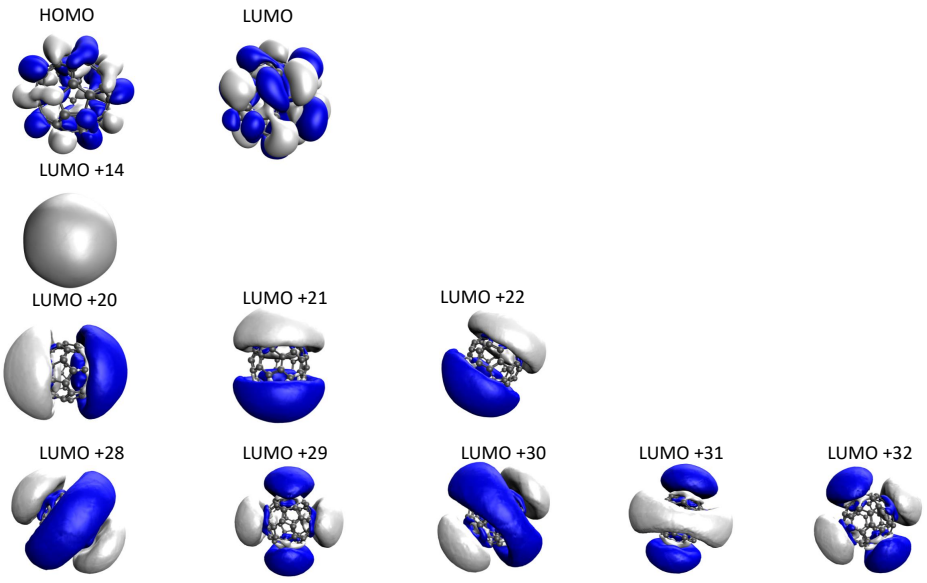


Figure 3.2: *Molecular orbitals for C_{60} calculated using the B3LYP/6-31++G** level of theory.*

Table 3.3: HOMO-LUMO (Δ_{HL}) and LUMO-SAMO (Δ_{LS}) (s,p, and d type) gaps (in eV) for C_{60}, Ca@C_{60} and Li@C_{60}.

	Δ_{HL}	$\Delta_{LS}(s)$	$\Delta_{LS}(p)$	$\Delta_{LS}(d)$
C_{60}	2.70	3.30	4.20	4.70
Ca@C_{60}	0.95	1.60	-	2.86
Li@C_{60}	0.90	2.01	3.50	4.60

and hydrogenated fullerenes with endohedral doping were determined using DFT at the B3LYP/6-31++G** level of theory and are shown in Table 3.3.

The HOMO-LUMO gap of C_{60} is predicted to be 2.7 eV and the LUMO-SAMO for C_{60} is predicted to be at 3.3, 4.2, and 4.7 eV for s-, p- and d- SAMOs respectively which is in a good agreement with the plane-wave calculations and the experimental work.[144] The HOMO-LUMO gap of C_{60} decreases once the atom is encapsulated within the cage, for Ca by 1.75 eV, and for Li by 1.8 eV. It can be observed that the SAMO energies are also altered by the Li and Ca presence when compared to empty C_{60}. The s-SAMO-LUMO gap is reduced by 1.3 eV and by 1.6 eV when Li and Ca atoms are added respectively. The energy difference of p-SAMO between C_{60} and Li@C_{60} is only 0.7 eV. It was

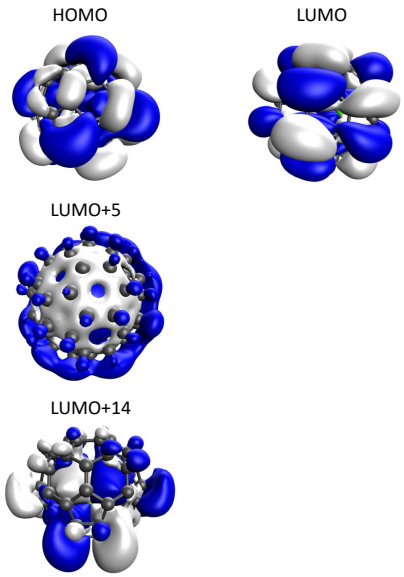


Figure 3.3: *Molecular orbitals for $Ca@C_{60}$ calculated using the B3LYP/6-31++G** level of theory.*

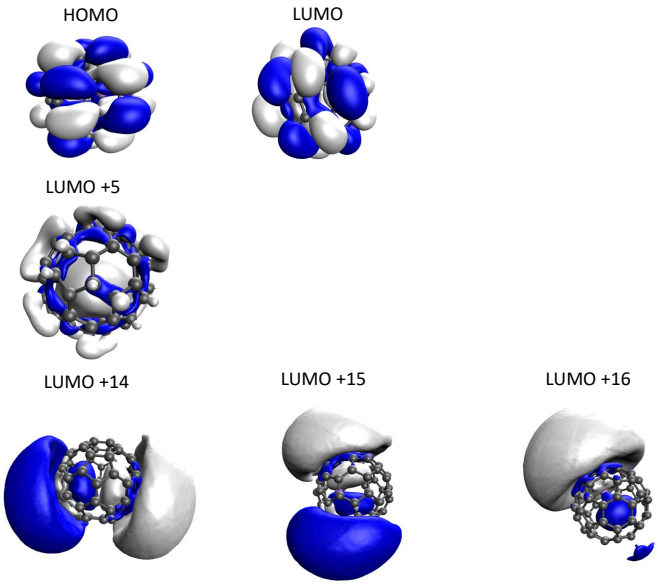


Figure 3.4: *Molecular orbitals for $Li@C_{60}$ calculated using the B3LYP/6-31++G** level of theory.*

not possible to find *p*-SAMO for Ca@C_{60}. The *d*-SAMO-LUMO was reduced by 1.84 eV when Ca atom was encapsulated in C_{60}. While a very small effect (0.1 eV gap reduction) was observed for Li@C_{60}. The reduced LUMO-SAMO energy can be explained by the effect of hybridization of the metal atom *d* orbitals and SAMOs of C_{60} as consequences of the corelation of Li and Ca ion and C_{60} molecule potentials within the hollow C_{60} core.[144] The other SAMOs, *p*- and *d*-types, of C_{60} are less affected by the encapsulated atoms because the respective *p* and *d* orbitals of endohedral atoms have higher energies than *s* orbitals, therefore making it more difficult for the orbitals to hybridize.[144]

3.4 Effect of Hydrogenation on Endohedral C_{60}

To explore how the presence of the hydrogen atoms on the surface of the C_{60} shell affects the SAMO wavefunction distribution and the energy of SAMOs, DFT/B3LYP/6-31++G** level of theory was used to investigate the hydrogenated fullerenes $C_{60}H_{60}$, Ca@$C_{60}H_{60}$ and Li@$C_{60}H_{60}$. Figures 3.5, 3.6, and 3.7 show the 3D visualisation of the orbitals found in hydrogenated fullerenes. As can be seen, the shape of the orbitals is much more regular when compared to non-hydrogenated fullerenes. Starting with *s*-SAMO, all three *p*-SAMOs and five *d*-SAMO orbitals were observed following in order, without any other orbitals between (*e.g.* for C_{60}, the LUMO corresponds to *s*-SAMO, LUMO+1 to p_x-SAMO, LUMO+2 to p_y-SAMO, LUMO+3 to p_z-SAMO, LUMO+4 to d_{xy}-SAMO, LUMO+5 to d_{yz}-SAMO, and so on). This was not observed in non-hydrogenated fullerenes where non-SAMO orbitals were found between the *s*-SAMOs and *d*-SAMOs. For $C_{60}H_{60}$ the LUMO already looks like *s*-SAMO, while for Ca@$C_{60}H_{60}$ and Li@$C_{60}H_{60}$ the SAMOs shape can be observed for HOMOs. It can be also noticed that the *p*-SAMOs orbitals are similarly located for both Ca@$C_{60}H_{60}$ and Li@$C_{60}H_{60}$, while for *d*-SAMOs distribution some difference is observed. The *d*-SAMO in Ca@$C_{60}H_{60}$ are much more cen-

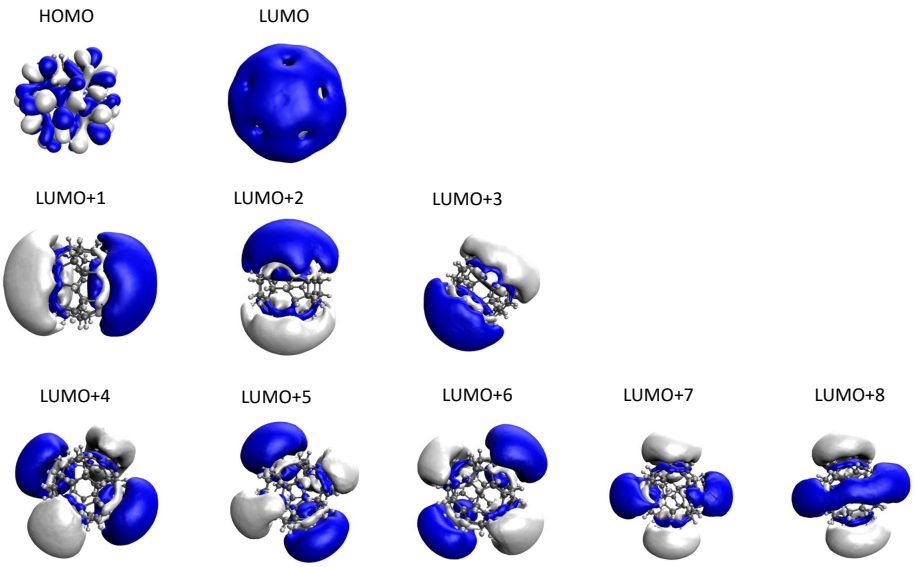


Figure 3.5: *Molecular orbitals for $C_{60}H_{60}$ calculated using the B3LYP/6-31++G** level of theory.*

tered on Ca atom than on the Li atom in Li@$C_{60}H_{60}$. It could suggest that the SAMOs in Li@$C_{60}H_{60}$ originate from the C_{60} cage, while the SAMOs in Ca@$C_{60}H_{60}$ arise from orbital hybridisation of the Ca atom and C_{60} cage.

The LUMO-SAMO gap energies were calculated for the hydrogenated C_{60} with and without the endohedral doping and are shown in Table 3.4. It can be observed that the SAMO energies are significantly altered by the presence of hydrogen atoms on the surface of the carbon cage when compared to empty C_{60} with and without atoms within the cages. The energy of the *s*-SAMO in $C_{60}H_{60}$ is identical to that of the LUMO therefore the LUMO-*s*-SAMO gap is considered to be 0. The LUMO-*p*-SAMO gap is calculated to be 0.38 eV and LUMO-*d*-SAMO as 0.87 eV. These values are much lower (by 5, 8, and 4 times) than for the LUMO-*s*-, *p*-, and *d*-SAMO gaps in C_{60}, respectively.

Also, for the hydrogenated endohedral fullerenes significant difference in the SAMO energy can be observed compared to non-hydrogenated ones. Interestingly, the lowest energy of the *s*-SAMO in Li@$C_{60}H_{60}$ and Ca@$C_{60}H_{60}$ has the same energy as that of HOMO. When comparing the LUMO-SAMO gap for the Li in C_{60} to Li in $C_{60}H_{60}$ we can see that the energy gap is slightly re-

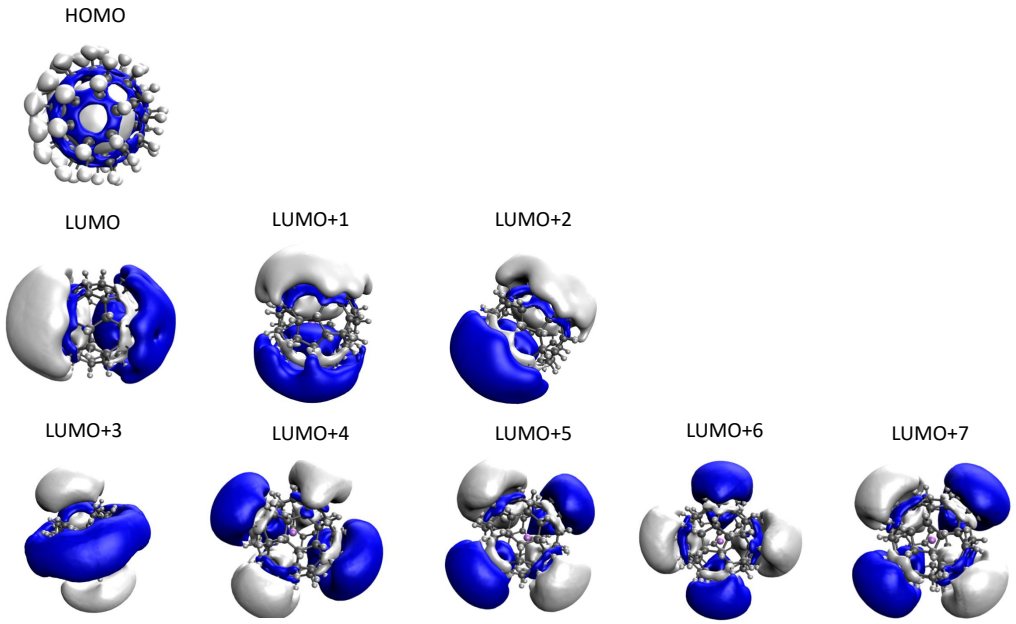


Figure 3.6: *Molecular orbitals for $Li@C_{60}H_{60}$ calculated using the B3LYP/6-31++G** level of theory.*

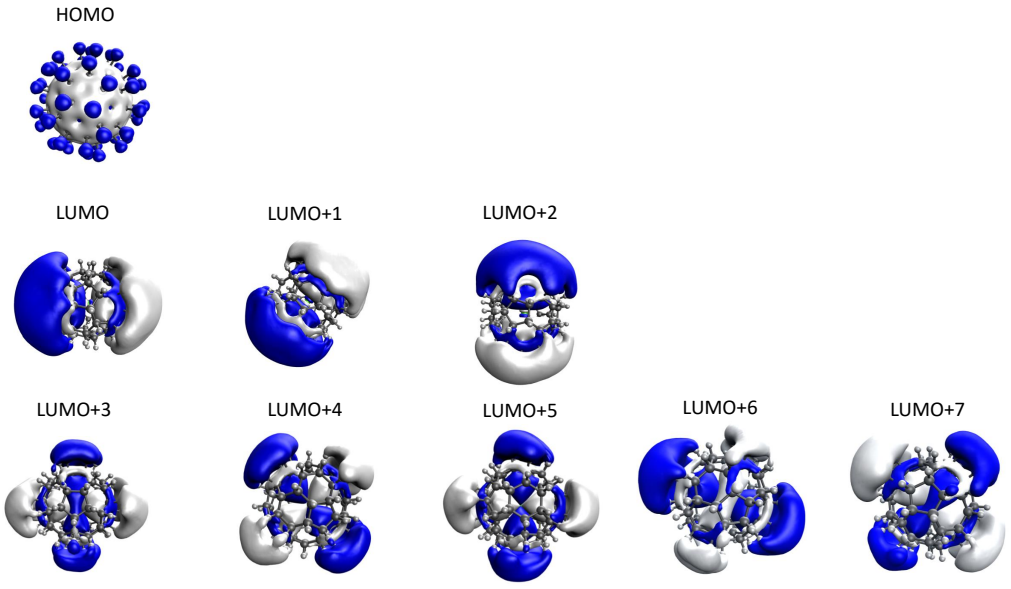


Figure 3.7: *Molecular orbitals for $Ca@C_{60}H_{60}$ calculated using the B3LYP/6-31++G** level of theory.*

Table 3.4: HOMO-LUMO (Δ_{HL}) and LUMO-SAMO (Δ_{LS}) (*s*-, *p*-, and *d*-type) gaps (in eV) for $C_{60}H_{60}$, $Ca@C_{60}H_{60}$ and $Li@C_{60}H_{60}$.

	Δ_{HL}	$\Delta_{LS}(s)$	$\Delta_{LS}(p)$	$\Delta_{LS}(d)$
$C_{60}H_{60}$	5.36	0	0.38	0.87
$Ca@C_{60}H_{60}$	2.15	2.15	0	0.33
$Li@C_{60}H_{60}$	1.96	1.96	0	1.28

Table 3.5: Lowdin charges calculated for the HOMO in hydrogenated and non-hydrogenated $Li@C_{60}$ and $Ca@C_{60}$.

HOMO	C_{60}	$C_{60}H_{60}$
Li *s*	0.0000	0.2400
Li *p*	0.0003	0.0184
Li *d*	0.0041	0.1920
Ca *s*	0.0000	0.4201
Ca *p*	0.0012	0.0000
Ca *d*	0.0020	0.4228

duced for LUMO-*s*-SAMO (by 0.04 eV) but significantly (*ca.* 3 times) reduced for LUMO-*p*-SAMO and LUMO-*d*-SAMO. A similar situation is observed for the presence of a Ca atom within the cage. The results indicate that the SAMO energy can be potentially tailored by the shell molecules (in this case hydrogen atom). In the future, it would be worth investigating other ligands and their effect on the electronic structure of C_{60}, as well as on the stability of the structures.

The reduced LUMO-SAMO energy can be explained by the effect of hybridization of metal atom and SAMOs of C_{60} as a consequences of the correlation of the Li ion and C_{60} molecule potentials within the hollow molecule core.[144] When we then look at the partial charge on the metal atoms in the highest occupied states of the fullerenes presented in Table 3.5, it can be seen that the HOMO in hydrogenated fullerene mainly originates from the *s*-orbitals and *d*-orbtials of the metal ions in both, $Li@C_{60}H_{60}$ and $Ca@C_{60}H_{60}$.

In C_{60} the highest occupied states mainly originate from carbon cage for both endohedral fullerenes. Potentially, the presence of H on the surface influences the contribution of *d* orbitals of the endohedral atoms to the HOMO orbital. Potentially the involvement of *d* orbitals of the metal atoms in hybridization with SAMO lowers the LUMO-SAMO gap of the fullerenes.

3.5 SAMO States of Endohedral Fullerenes Calculated using TDDFT

DFT describes one-electron SAMO orbitals and helps to estimate the LUMO-SAMO gaps while it is interesting to investigate the SAMOs states. To describe SAMOs excited states in C_{60}, TDDFT calculations were used. TDDFT allows determination of the excitation energies and finding orbitals which are involved in the corresponding transitions. Table 3.6 shows the highest oscillator strength low-energy transitions along with a characterization of the nature of the transition. In the case of pure C_{60} and $C_{60}H_{60}$ no excited states were found with the oscillator strength higher than 0.0005. Previous experimental work showed that in C_{60}, an $\mathcal{I}_h$ point group molecule with icosahedral symmetry, the SAMO states are not optically active and can only be accessed by vibronic coupling between optically active valence states and the SAMO states.[188] However the C_{60}'s symmetry can be broken by doping with other atoms which lifts the degeneracy of certain SAMO states and consequently make them optically active.[189] The results (Table 3.6) show that the first lowest lying excited states with the oscillator strength higher than 0.0005 for Li@C_{60} and Ca@C_{60} correspond to transition from HOMO orbitals to the LUMOs both located on carbons of the C_{60}. Transition from the HOMO to SAMO is observed at higher energies, for Li@C_{60} at 2.1 eV (oscillator strength of 0.0007) and for Ca@C_{60} at 1.82 eV (oscillator strength 0.0002).

Table 3.6: Transition energies, assignments, and oscillator strength (f) calculated using TDDFT/B3LYP/6-31++G** for the pure and hydrogenated C_{60}, Li@C_{60}, and Ca@C_{60}. (L) stands for localised.

	ΔE/eV	Nature of transitions	f
C_{60}	2.5	Multi-excitations	>0.0005
Ca@C_{60}	0.4412	HOMO (L) to LUMO+1 (L)	0.0025
	1.6468	HOMO (L) to LUMO+2 (L)	0.0618
	1.7221	HOMO (L) to LUMO+3 (L)	0.0754
	1.8234	HOMO (L) to LUMO+5 (*s*-SAMO)	0.0002
Li@C_{60}	1.3707	HOMO (L) to LUMO+2 (L)	0.0370
	1.4078	HOMO (L) to LUMO+3 (L)	0.0397
	2.1388	HOMO (L) to LUMO+5 (*s*-SAMO)	0.0007
$C_{60}H_{60}$	4.8	Multi-excitation	>0.0005
Ca@$C_{60}H_{60}$	2.0361	HOMO (*s*-SAMO) to LUMO (*p*-SAMO)	0.6089
	2.0375	HOMO (*s*-SAMO) to LUMO+2 (*p*-SAMO)	0.6069
	2.0382	HOMO (*s*-SAMO) to LUMO+1 (*p*-SAMO)	0.6100
Li@$C_{60}H_{60}$	1.4079	HOMO (*s*-SAMO) to LUMO (*p*-SAMO)	0.2385
	1.4118	HOMO (*s*-SAMO) to LUMO+2 (*p*-SAMO)	0.2388
	1.4490	HOMO (*s*-SAMO) to LUMO+3 (*p*-SAMO)	0.2420

The electronic structure of those endohedral fullerenes changes significantly once the hydrogen atoms are present on the surface of the C_{60} shell. The first excited state for $Li@C_{60}H_{60}$ is at 1.4 eV and is formed through excitation from HOMO to LUMO, where the HOMO looks like a *s*-SAMO and the LUMO like a *p*-SAMO (Figure 3.8). The excitation energy is lower by 1 eV when compared to the excited state arising from the excitation to the SAMO orbital for $Li@C_{60}$. In the next excited states, an electron is transferred from HOMO to other LUMOs which all have *p*-SAMO character. The oscillator strength for all those states is 0.24. The presence of Ca within the carbon cage has a similar effect to Li on shifting the position of SAMO however has less pronounced effect on the energies of the excited states where an electron has been transferred from HOMO to SAMO. The first excited state for $Ca@C_{60}H_{60}$ is at 2 eV and is formed through excitation from the HOMO to LUMO, where HOMO looks like an *s*-SAMO and the LUMO like a *p*-SAMO (Figure 3.9). The three-dimensional (3D) visualization of the ground-state and excited-state molecular orbitals contributing to first optical transition are shown in Figures 3.8 and 3.9 for $Li@C_{60}H_{60}$ and $Ca@C_{60}H_{60}$ respectively. As it can be seen that the HOMO and LUMO orbitals look like *s*-type and *p*-type atomic orbitals, respectively. They have significant electronic density inside C_{60} and therefore are considered as SAMOs.

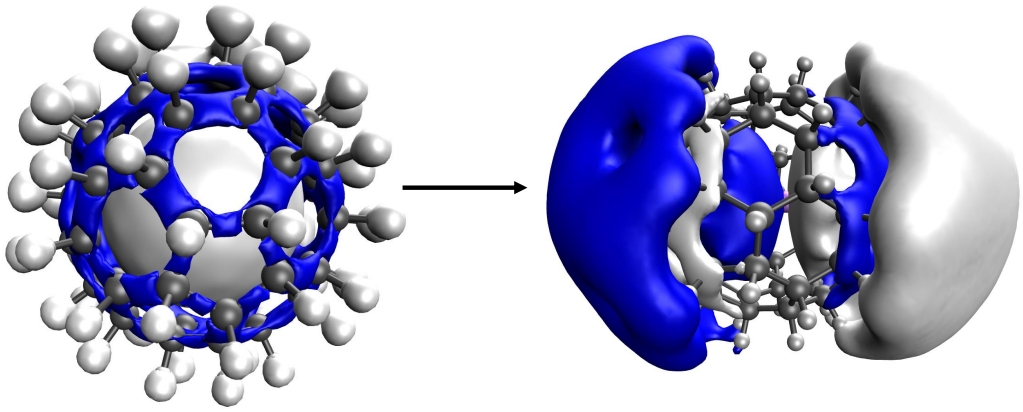


Figure 3.8: *Molecular orbitals associated with the intense transition for* $Li@C_{60}H_{60}$.

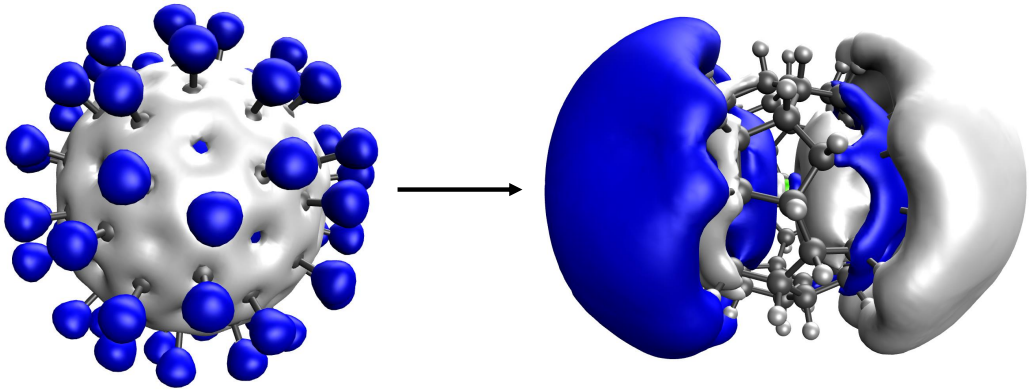


Figure 3.9: *Molecular orbitals associated with the intense transition for* $Ca@C_{60}H_{60}$.

3.6 Conclusion

The use of DFT-based calculations to characterize endohedral fullerenes (in particular, $Li@C_{60}$ and $Ca@C_{60}$) and the effect of their hydrogenation on the energy and distribution of SAMOs was investigated. Calculated results of hydrogenated C_{60}, $Li@C_{60}$, and $Ca@C_{60}$ show that the LUMO-SAMO energy of these fullerenes vary with the type of atoms inside the cage and the presence of hydrogen atoms on the shell. Through an analysis of calculations of the excited states of the hydrogenated endohedral fullerenes, it was confirmed that the SAMO orbitals are affected by the presence of the metal atom within the C_{60} cage and the hydrogen atoms on its surface. Results of DFT calculations show that the presence of metal atoms lowers the LUMO-(s, p, d)-SAMO gaps of C_{60} and $C_{60}H_{60}$. While the presence of hydrogen atoms on the surface of the carbon cage lowers further the LUMO-(d)SAMO gap, and more profoundly for $Ca@C_{60}H_{60}$. The use of TDDFT calculations highlights that the SAMO states are lower in energy for hydrogenated $Li@C_{60}H_{60}$ compared to $Li@C_{60}$. In $Li@C_{60}$ and $Ca@C_{60}$, SAMO states are above the LUMO states and, therefore, they are unlikely to be relevant for charge transport used in molecular electronics. However, in the case of hydrogenated $Li@C_{60}$ and $Ca@C_{60}$ electronic states are observed where the s-SAMO can be found below the LUMO. In

fact, HOMO and LUMO in both cases are *s*-SAMO and *p*-SAMO respectively. This characteristic is significant when considering the design of fullerene-based systems for molecular electronics applications. Overall, the results enable the characterisation of the electrical properties of a novel type of material designed for molecular electronic applications. The unusual electronic properties of C_{60} based molecules are obtained from the SAMO states. Also, the characterisation method can be used for exploring other C_{60} based molecules. Both DFT and TDDFT calculations confirm the positive effect of hydrogen atoms on the surface of studied fullerenes in terms of reducing the LUMO-SAMO gap and excitation energy of SAMO states. Therefore, it is believed that if materials such as $Ca@C_{60}H_{60}$ or $Li@C_{60}H_{60}$ could be synthesized, then it would open the possibility of using those materials for molecular electronic applications.

Chapter 4

Vibrationally Resolved Spectra for N_2 and $N_2@C_{60}$

4.1 Introduction

As mentioned in the previous chapter, one of the most interesting properties of fullerenes is their capability to enclose different atoms and small molecules within their cage. Consequently they exhibit unusual properties. The ability to trap not only metallic atoms but also gases and non-metal atoms inside fullerenes could lead to the development of new materials characterised by unique properties and applications. In contrast to metal atoms which transfer their charge to the cage and occupy the position closer to the walls of the cage (because of Coulombic interactions), atoms such as N, P or noble gases do not interact strongly with the cage and show little or no charge transfer to the cage, consequently occupying the centre position within the carbon cage.[190,191] The lack of interactions between the cage and the atom makes the properties of those endohedral fullerenes similar to the properties of the empty cages. As a result, they can be used as traces by He-NMR, or electron paramagnetic resonance.[192,193] Some examples of gases encapsulated in fullerenes include Ar,

Kr, Xe, He, and Ne.[194–198]

To understand better the structural properties of the endohedral fullerenes, various techniques were employed, such as He-NMR, single-crystal X-ray analysis, photoelectron diffraction and X-ray photoelectron spectroscopy.[192–195,197,198] Alongside experimental work, theoretical studies of fullerenes and endohedral fullerenes can help to predict the properties of endohedral fullerenes and explain the experimental results. Using *ab initio* and molecular dynamics calculations various characteristics were investigated, including stabilisation of noble gases inside the C_{60}, as well as the mechanism of entering the gases into the C_{60}.[160,161,199,200] The research conducted on the stabilization of the noble gases within C_{60} has provided interesting insights on the behaviour of these gases inside their cage. For instance, the calculations on $Ne@C_{60}$ revealed slight interaction of Ne with the cage and its cantered position within the cage.[160,161,199] Molecular dynamics studies performed on the encapsulated noble gases in C_{60} and C_{70} showed the possibility of forming He and Ne complexes with C_{60} and C_{70}, whereas encapsulation of much bigger atoms such as Ar and Kr was shown to be more challenging due to van der Waals interactions.[200] Using *ab initio* methods, the mechanism of the encapsulation of atoms in fullerenes was also studied. One of the suggested mechanisms of the encapsulation of atoms, explored through various computational methods, suggests that one, or a few, carbon-carbon bonds breaks and resulting 'window' allows the atom to enter the fullerene cage.[201] Another mechanism called the direct entrance mechanism was suggested for H, He, and N atoms using DFT calculations.[202] Apart from information on stability and the formation mechanism, it is very useful to be able to obtain more detailed information about the electronci structure of endohedral fullerenes. Vibrational frequencies of $Ne@C_{60}$ were simulated, and the assignment of the peaks for the experimental infrared IR spectra was possible.[203] Also, the effect of spin state on the vibrational spectra of $La@C_{60}$ and $Ce@C_{60}$ were calculated using DFT.[204]

High resolution X-ray absorption spectroscopy (XAS) of molecules is a technique that is sensitive to the symmetry of the molecules and specific to their individual elements. Clearly identifiable vibrational structures of studied molecules can be obtained using XAS. By combining theoretical studies with XAS it is possible to obtain the vibrational structure of the spectrum, assign the individual spectral features; and determine the effect of vibrations on the excitation energy.[23,205–208] Various levels of theory were used to obtain the XAS, such as symmetry-adapted cluster–configuration interaction (SAC–CI); algebraic diagrammatic construction (ADC); and time-dependent density functional theory (TD-DFT).[54,209–214]

In this work; the accuracy of DFT-based methods for the simulation of vibrationally resolved X-ray absorption spectra of the N_2 molecule were investigated. Subsequently TDDFT was applied to study the XAS of $N_2@C_{60}$ to investigate the dependence of the spectra on the presence of the fullerene cage. Also, the effect of C_{60} cage on the bond length, frequency and force constant of encapsulated N_2 was investigated.

4.2 Computational Methods

4.2.1 Electronic Calculations

DFT calculations were used for the computation of the ground state geometries and vibrational frequencies for both, N_2 and $N_2@C_{60}$. To determine and characterise the excited states and the transition energies, TDDFT calculations were carried out. To study the N_2 molecule, five density functionals were tested, namely the gradient corrected BLYP functional, hybrid functionals with different ratios of HF exchange, *i.e.* B3LYP (20% of HF exchange), and PBE0 (25% of HF exchange), the long-range corrected CAM-B3LYP func-

tional, and short range corrected SRC1R1. In addition, three different basis sets were used, namely the modest 6-31G(d) and more extended 6-31+G(d,p) and 6-311+G(2d,2p) basis sets with diffuse and polarisation functions. All the calculations were performed by using the software Q-Chem version 6.1.

4.2.2 Calculation of the Vibronic Spectra

To calculate vibrationally resolved spectra by incorporating Franck–Condon effects, the ezFCF package was used.[215] The ezFCF program computes spectra within the double-harmonic approximation and calculates the Franck–Condon factors (FCFs) based on the equilibrium geometries, harmonic frequencies and normal modes computed previously with DFT and TDDFT. The ezFCF package uses the vibrations of both energy states along with the energy difference between the two. Franck–Condon factors (FCFs), as the overlaps between the initial and target vibrational wavefunctions are calculated in the parallel normal modes approximation as products of one-dimensional harmonic wave functions. In the parallel approximation, the normal coordinates of the initial and the target electronic states are assumed to be the same. Consequently, the multidimensional Franck–Condon factors reduce to products of one dimensional FCFs. ezFCF then computes each one-dimensional harmonic FCF analytically. The vibrationally-resolved XAS were then obtained by convoluting the excitation energies with a Lorentzian function.

4.3 Characterisation of N_2

4.3.1 Evaluation of Computational Methods

The focus of this chapter is to simulate vibrationally resolved XAS for N_2 and $N_2@C_{60}$ and to investigate the effect of C_{60} on the behaviour and spectra of N_2.

Table 4.1: Energy transitions (from $1s$ to $\pi*$) and corresponding oscillator strengths (f) for N_2 using five different functionals (B3LYP, CAM-B3LYP, PBE0, SCR1R1, and BLYP) and three different basis sets (6-31G, 6-31++G**, and 6-31(2+,2+)G**).

Method	ΔE/eV	f
B3LYP/6-31G	389.03	0.1128
B3LYP/6-31++G**	389.14	0.1083
B3LYP 6-311(2+,2+)G**	388.45	0.1090
CAM-B3LYP/6-31G	389.03	0.1126
CAM-B3LYP/6-31++G**	389.15	0.1081
CAM-B3LYP/6-311(2+,2+)G**	388.41	0.1086
PBE0/6-31G	390.11	0.1168
PBE0/6-31++G**	390.21	0.1125
PBE0/6-311(2+,2+)G**	389.63	0.1132
SRC1R1/6-31G*	-	-
SRC1R1/6-31++G**	-	-
SRC1R1/6-311(2+,2+)G**	400.68	0.1542
BLYP/6-31G	383.01	0.0938
BLYP/6-31++G**	383.10	0.0875
BLYP/6-311(2+,2+)G**	382.26	0.0860

To observe the vibrational levels, the nitrogen molecule must be first excited into metastable radiative states. After X-ray absorption the core electron in N_2 is excited from $1s$ to π^*. To find out which excited state corresponds to this transition, TDDFT calculations were performed. Firstly, the geometry of the ground and excited states of N_2 were optimised. Then, the performance of the different functionals and basis sets for the excitation energies was investigated. Table 4.1 shows energy transitions (from $1s$ to π^*) and corresponding oscillator strengths for N_2 using five different functionals (B3LYP, CAM-B3LYP, PBE0, SCR1R1, and BLYP) and three different basis sets (6-31G, 6-31++G**, and 6-311(2+,2+)G**).

The experimental value for the excitation of N_2 was observed to be 400.53 eV

(unpublished data, courtesy of Prof. Phil Moriarty, School of Physics, University of Nottingham). As can be seen in Table 4.1, the values for all of the functionals and basis sets, apart from SRC1R1/6-311(2+,2+)G** are much lower than the experimental value. The SRC1R1/6-311(2+,2+)G** method has been specially designed for XAS spectroscopy and provides the most accurate results.[56] However, it includes analytical calculation, therefore for bigger systems it might be not the most suitable method. The other methods underestimated the energy values because of the challenge associated with a significant reduction in the screening of the core when the electron is excited from a core orbital. This leads to large relaxation effects such as contraction of the valence electron density and repulsion. Therefore, it is a common practice in scientific community to shift the energy values to match the experimental results, even up to 17 eV.[216–219] Therefore, using hybrid functionals is still valid. Further analysis was carried out using a DFT approach with hybrid functioanl, but without SRC1R1.

4.3.2 Bond Length and Vibrational Frequency of N_2

It is also interesting to see how the bong length and frequency calculations are affected by the choice of functional and basis set. Table 4.2 presents the theoretical bond lengths for N_2 in the optimized ground state (R) and excited state (R'), as well as their differences denoted by $\Delta R = R' - R$ obtained with different functionals and basis sets. A comparison with gas phase experiments is also provided. Experimentally, the bond length of N_2 in its ground state was found to be around 1.098 Å and it increases up to 1.164 Å in the excited states. The longer bond in the excited state is expected as the excitation out of the σ molecular orbital into the π^* antibonding orbital weakens the N_2 bond and causes it to elongate. As shown in Table 4.2, the theoretical results obtained from all functionals and basis sets vary in agreement with the

experiments. The closest values to the bond length of N_2 in the ground state obtained experimentally were obtained using the 6-311(2+,2+)G** basis set regardless of the type of functional. This indicates that the basis set plays a more important role than the functional when describing the ground state of N_2. For the excited state, the bond length was predicted more accurately when using the 6-31G basis set for B3LYP, CAM-B3LYP, and PBE0. While for BLYP, using the 6-31G basis set resulted in longer bond length when compared to experiment, and the bond length was overestimated by 0.02 Å. For the other basis sets, the bond length was much shorter than the experimentally measured value, by around 0.03 Å. The closest value for the difference in the bong length (ΔR) to the experimental value was predicted using B3LYP and BLYP functionals with the 6-31G basis set where the difference in bond length (ΔR) is 0.050 Å and 0.057 Å respectively. Followed by the calculations using B3LYP/6-31++G** which resulted in a ΔR value of 0.040 Å. While other methods substantially underestimated the value for ΔR.

The vibrational frequencies for ground (Ω) and excited states (Ω') are presented in Table 4.3. The experimental vibrational frequencies for N_2 in the ground state were found to be 2359.0 cm^{-1} and in the excited state 1966.2 cm^{-1}. This value corresponds to the frequency characteristic for the stretching vibrational mode in N_2 molecule. The frequency for the ground and excited state is predicted the most accurately by using the 6-31G basis set with hybrid functionals. Among which B3LYP shows the closest values to experiment with deviation of 4.5 cm^{-1} and 15.3 cm^{-1} for ground and excited states respectively. Using larger basis sets with hybrid functionals results in a larger difference for both states where, much higher values are observed for the excited states. Differences of 173.8 cm^{-1}, 248.8 cm^{-1}, 243.8 cm^{-1}, and 177.94 cm^{-1} were predicted when using 6-31++G** with B3LYP, CAM-B3LYP, PBE0, and BLYP, respectively.

Also, as can be seen in Table 4.3, using 6-31G basis set with all func-

Table 4.2: Comparison of bond lengths (in Å) in the optimized ground (R) and excited (R') states of N_2 calculated using DFT with different functionals and basis sets.

	-	B3LYP	CAM-B3LYP	PBE0	BLYP
Experiment					
R	1.098	-	-	-	-
R'	1.164	-	-	-	-
ΔR	0.066	-	-	-	-
6-31G					
R	-	1.118	1.112	1.114	1.132
R'	-	1.168	1.159	1.160	1.188
ΔR	-	0.050	0.047	0.046	0.057
6-31++G**	-				
R	-	1.105	1.100	1.102	1.118
R'	-	1.145	1.137	1.138	1.160
ΔR	-	0.040	0.037	0.036	0.042
6-311(2+,2+)G**	-				
R	-	1.096	1.090	1.094	1.101
R'	-	1.130	1.123	1.126	1.143
ΔR	-	0.034	0.033	0.032	0.042

Table 4.3: Comparison of vibrational frequencies (cm^{-1}) in the optimized ground (Ω) and excited (Ω') states of N_2 calculated using DFT with different functionals and basis sets.

	-	B3LYP	CAM-B3LYP	PBE0	BLYP
Experiment					
Ω	2359.01	-	-	-	-
Ω'	1966.21	-	-	-	-
$\Delta\Omega$	392.83	-	-	-	-
6-31G					
Ω	-	2354.50	2414.36	2394.11	2229.62
Ω'	-	1950.90	2032.60	2019.60	1788.26
$\Delta\Omega$	-	403.60	381.76	374.51	441.36
6-31++G**					
Ω	-	2456.50	2510.00	2497.30	2337.11
Ω'	-	2144.83	2215.00	2210.00	2011.07
$\Delta\Omega$	-	311.67	295.00	287.30	326.04
6-311(2+,2+)G**					
Ω	-	2446.00	2498.61	2484.44	2329.95
Ω'	-	2195.00	2263.44	2252.94	2072.36
$\Delta\Omega$	-	251.00	235.17	231.50	257.59

tionals resulted in the smallest difference in $\Delta\Omega$ when compared to experimental results. The values are overestimated only by $10.8\,cm^{-1}$ for B3LYP, $11.4\,cm^{-1}$ for CAM-B3LYP, $18.6\,cm^{-1}$ for PBE0, and $48.56\,cm^{-1}$ for BLYP. Using the 6-31++G** basis set the predicted values are overestimated by $76\,cm^{-1}$, $97.8cm^{-1}$, $105.5\,cm^{-1}$, and $66.76\,cm^{-1}$ for B3LYP, CAM-B3LYP, PBE0 and BLYP, respectively. However this is still considered to be acceptable value for the prediction of vibrational frequencies. A similar level of accuracy was observed in literature, where overestimation of $102\,cm^{-1}$ in the N_2 ground state was reported using the MP2 method.[220] The largest discrepancy with the experimental results is obtained with the 6-311(2+,2+)G** basis set for all tested functionals.

4.4 Vibrationally Resolved XAS of N_2

Figure 4.1 illustrates the simulated vibrationally-resolved XAS of N_2, computed using TDDFT with four different functionals and three different basis sets and compared to experimental data. In the experimental spectrum five distinct vibronic features can be observed, separated by the same distance which is equivalent to the vibrational frequency. The separation between the experimental peaks is equal to 0.27 eV.

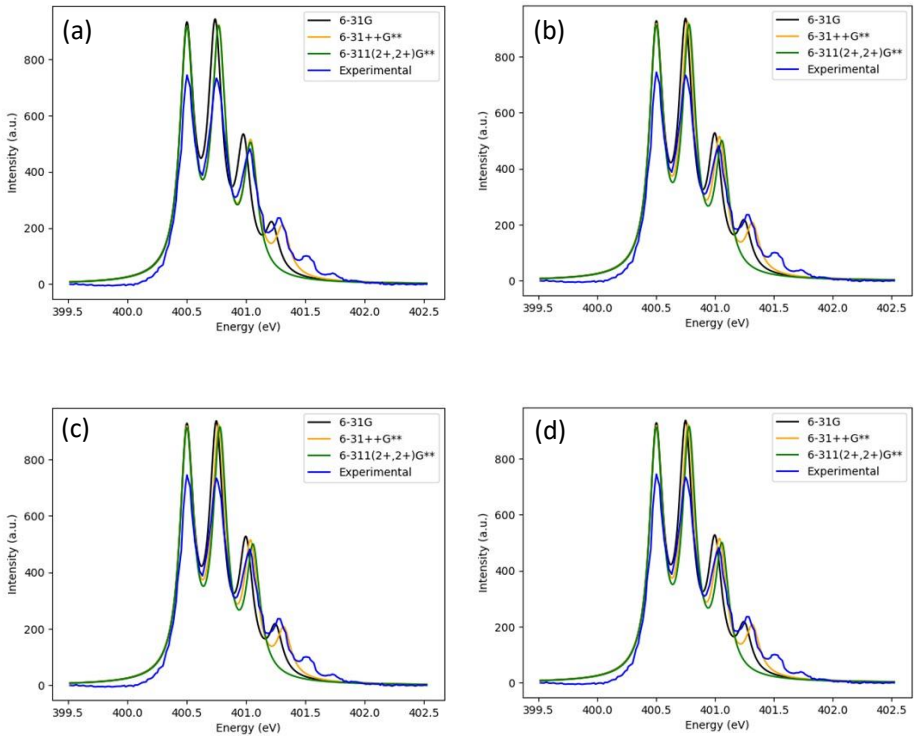


Figure 4.1: *Vibrationally resolved N 1s XAS of N_2 simulated using TDDFT with B3LYP (a), CAM-B3LYP (b), PBE0 (c), and BLYP (d) and different basis sets.*

The intensity of the peaks represents the overlap between the initial and final vibrational wavefunctions and is observed to vary depending on the transition. The higher the overlap between the wavefunctions the higher the intensity of the peak can be observed. The obtained theoretical results with various functionals and basis sets demonstrate generally good agreement with experimental observations. The intensity of the two first peaks is overesti-

mated but the intensity of the rest of the peaks agrees with the experiment. The main difference between different functionals and basis sets can be observed in the peak separations. The calculations using B3LYP functional and the 6-31++G** basis set accurately predict the peak separations (0.27 eV). While 6-31G* with all studied functionals predicted relatively small peak separations (between 0.22 eV for BLYP and 0.25 eV for PBE0 and CAM-B3LYP), while the 6-311(2+,2+)G** calculations slightly overestimated the separation when compared to the experimental results. The results show that the basis sets influence the calculations of vibrational frequency more profoundly than functionals. All of the basis sets apart form 6-311(2+,2+)G** predicted four peaks. The four peaks correspond to four vibronic transitions (Table 4.4).

They all represent transition from ground state (0(0)) to first excited state (1(0)), then consecutively to one vibrational quanta in the zeroth vibronic mode of the first excited state 1(1v0), followed by transition to two quanta in the zeroth vibronic mode of the first excited state (1(2v0)), and to three quanta in the zeroth vibronic mode of the first excited state (1(3v0)) for the first, second, third and fourth peak respectively. The energies of the corresponding peaks vary slightly between different functionals. BLYP predicts the lowest energies (around 383 eV) while the others functionals show similar behaviour and calculated the vibrational energies are around 389 eV.

4.5 Characterisation of $N_2@C_{60}$

Calculations of the vibrationally resolved XAS indicated that using B3LYP with 6-31++G** yields the most accurate results in terms of the peak separation, which corresponds to the vibrational frequency. The results for the bond length and frequency using B3LYP with 6-31++G** were also in an acceptable range for the agreement with the experimental data. Therefore,

Table 4.4: Calculated energies (E/eV) for the vibrational transitions for N_2 using various functionals and basis sets. Column Δ/eV gives peak separations.

Functional	Basis set	Transitions	E/eV	Δ/eV
B3LYP	6-31G	$0(0) \rightarrow 1(0)$	389.03	0.24
		$0(0) \rightarrow 1(1v0)$	389.27	0.24
		$0(0) \rightarrow 1(2v0)$	389.51	0.24
		$0(0) \rightarrow 1(3v0)$	389.75	0.24
		$0(0) \rightarrow 1(4v0)$	389.99	0.24
	6-31++G**	$0(0) \rightarrow 1(0)$	389.14	0.27
		$0(0) \rightarrow 1(1v0)$	389.41	0.27
		$0(0) \rightarrow 1(2v0)$	389.67	0.27
		$0(0) \rightarrow 1(3v0)$	389.94	
	6-311(2+,2+)G**	$0(0) \rightarrow 1(0)$	388.31	0.27
		$0(0) \rightarrow 1(1v0)$	388.58	0.27
		$0(0) \rightarrow 1(2v0)$	388.85	
CAM-B3LYP	6-31G	$0(0) \rightarrow 1(0)$	389.03	0.25
		$0(0) \rightarrow 1(1v0)$	389.28	0.25
		$0(0) \rightarrow 1(2v0)$	389.53	0.25
		$0(0) \rightarrow 1(3v0)$	389.78	
	6-31++G**	$0(0) \rightarrow 1(0)$	389.15	0.27
		$0(0) \rightarrow 1(1v0)$	389.42	0.28
		$0(0) \rightarrow 1(2v0)$	389.70	0.30
		$0(0) \rightarrow 1(3v0)$	390.00	
	6-311(2+,2+)G**	$0(0) \rightarrow 1(0)$	388.31	0.28
		$0(0) \rightarrow 1(1v0)$	388.59	0.28
		$0(0) \rightarrow 1(2v0)$	388.87	
PBE0	6-31G	$0(0) \rightarrow 1(0)$	390.11	0.25
		$0(0) \rightarrow 1(1v0)$	390.36	0.25
		$0(0) \rightarrow 1(2v0)$	390.61	0.25
		$0(0) \rightarrow 1(3v0)$	391.86	
	6-31++G**	$0(0) \rightarrow 1(0)$	390.21	0.27
		$0(0) \rightarrow 1(1v0)$	390.48	0.28
		$0(0) \rightarrow 1(2v0)$	390.76	0.27
		$0(0) \rightarrow 1(3v0)$	391.03	
	6-311(2+,2+)G**	$0(0) \rightarrow 1(0)$	389.70	0.28
		$0(0) \rightarrow 1(1v0)$	389.98	0.28
		$0(0) \rightarrow 1(2v0)$	390.26	
BLYP	6-31G	$0(0) \rightarrow 1(0)$	383.01	0.22
		$0(0) \rightarrow 1(1v0)$	383.23	0.22
		$0(0) \rightarrow 1(2v0)$	383.45	0.22
		$0(0) \rightarrow 1(3v0)$	383.67	
	6-31++G**	$0(0) \rightarrow 1(0)$	383.10	0.24
		$0(0) \rightarrow 1(1v0)$	383.35	0.24
		$0(0) \rightarrow 1(2v0)$	383.59	0.24
		$0(0) \rightarrow 1(3v0)$	383.85	
	6-311(2+,2+)G**	$0(0) \rightarrow 1(0)$	382.26	0.25
		$0(0) \rightarrow 1(1v0)$	382.51	0.26
		$0(0) \rightarrow 1(2v0)$	382.77	

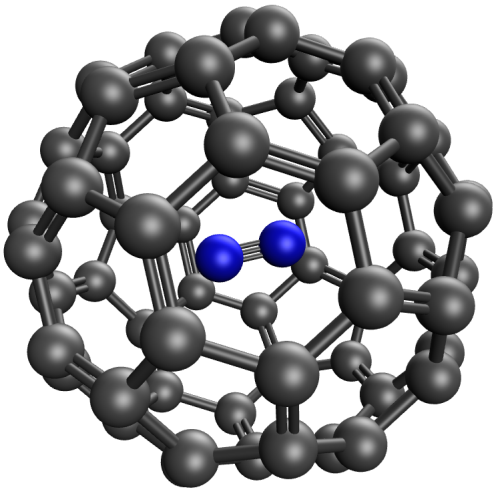


Figure 4.2: *Optimised ground state structure of $N_2@C_{60}$ using the B3LYP/6-31++G** level of theory.*

B3LYP/6-31++G** level of theory was chosen to carry out the rest of the studies. Figure 4.2 shows the optimised $N_2@C_{60}$ structure using B3LYP/6-31++G** level of theory. In the most stable geometry of $N_2@C_{60}$, the nitrogen molecule occupies the centre position of the cage (Figure 4.2). In Figure 4.3 the schematic MO diagram for the excitation of an electron from $1s$ to π^* is shown and the corresponding orbitals involved in the transition for N_2 and $N_2@C_{60}$. While for the nitrogen the electron is excited to the π^* located on N_2, in the case of $N_2@C_{60}$ the core electron is excited from σ to π^* located predominantly on the N_2 but also in small amount on the cage.

Table 4.5: Transition energies, assignments and oscillator strength (f) for the N_2 and $N_2@C_{60}$ calculated at the B3LYP/6-311++G** for N and 6-31G for C level of theory.

	ΔE/eV	Nature of transition	f
N_2	388.3624	N $\rightarrow$ N	0.1063
N_2	388.3624	N $\rightarrow$ N	0.1063
$N_2@C_{60}$	389.0745	N $\rightarrow$ N	0.0440
$N_2@C_{60}$	389.0756	N $\rightarrow$ N	0.0440

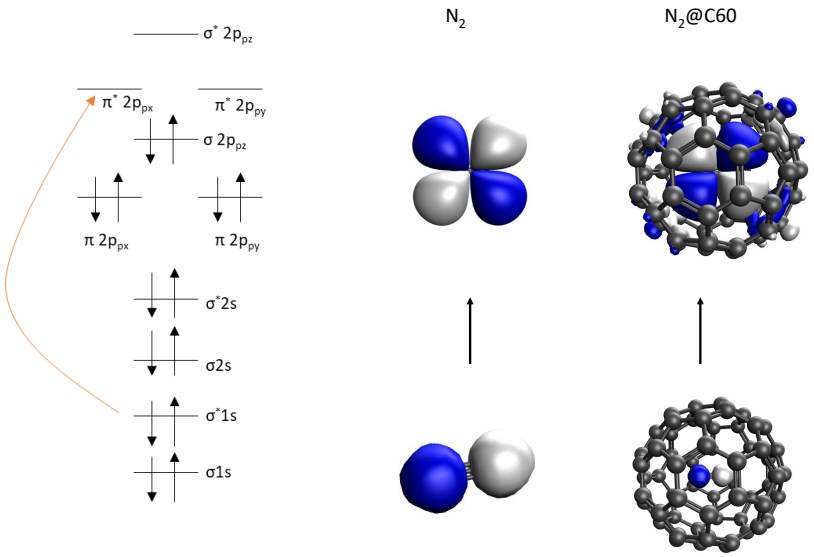


Figure 4.3: *MO diagram and 3D visualization of the ground-state and excited-state MOs involved in the transition corresponding to the first excited state for N_2 and $N_2@C_{60}$.*

After X-ray absorption, the core electron in N_2 is excited from initial $1s$ state to final π^*. Table 4.5 shows the transition energies with oscillator strengths higher than 0.1 along with a characterization of the nature of the transition for $N_2@C_{60}$ and compared to N_2 in gas phase. The first and second energy states (S_1 and S_2) correspond to N $\rightarrow$ N transitions and have high oscillator strengths (1.09). Looking at MO diagram and the three-dimensional visualization of the ground-state and excited-state molecular orbitals (Figure 4.6) it can be seen that those transitions correspond to $\sigma^* \rightarrow \pi^*$. In fact, there are two π^* degenerate orbitals within the molecule. The two excited states are formed through the transition to those orbitals. The transition energies for N_2 is the same for both excited states, while for $N_2@C_{60}$, there is very slight difference in the energy observed, indicating that the degeneracy of the the π^* orbitals is lifted in the presence of the cage. This could be because of the interaction between the N_2 and C_{60}, as shown in Figure 4.3, the π^* orbitals are slightly spread over the cage.

Table 4.6 shows the influence of a C_{60} cage on the bong length, frequency,

Table 4.6: The bond length (R) in Å, frequency (Ω) in cm^{-1}, and force constant (k) in atomic units of $N_2@C_{60}$ and N_2 in the ground and excited states predicted using the DFT/B3LYP/6-31++G** level of theory.

	$N_2@C_{60}$			N_2		
	Ground	Excited	Δ	Ground	Excited	Δ
R	1.10	1.14	0.04	1.10	1.14	0.04
Ω	2469.59	2325.15	144.44	2456.49	2139.95	316.54
k	50.31	44.60	5.70	49.78	37.78	12.00

and force constant of N_2 in the ground and excited states. All calculated using the B3LYP/6-31++G** level of theory. As can be seen, the bond length is very slightly influenced by the cage in both ground and excited state. In the ground state the bond length for N_2 in C_{60} is predicted to be 1.103 Å and in the ground state 1.143 Å, which is only shorter by 0.002 Å from N_2 bond length in the gas phase. The difference in the bond length after excitation is the same for both, N_2 and $N_2@C_{60}$. Table 4.6 includes also frequencies for the optimised ground and excited state of $N_2@C_{60}$. In $N_2@C_{60}$ there are 180 normal modes, and only one mode corresponds to the stretching mode of N_2, the rest of the modes are related to the cage. Table 4.6 shows the frequency of this exact mode, and as it can be seen, the frequency of $N_2@C_{60}$ in both, ground and excited state is predicted to be slightly higher than for the N_2 in gas phase. It is increased by 13 cm^{-1} for ground state and by 185 cm^{-1} for the excited state. The difference in the frequency ($\Delta\Omega$) is reduced by almost twice when N_2 is present in the C_{60} cage. This could indicate that in the presence of the cage less energy is required for the vibronic transition of N_2.

Table 4.6 also includes the calculated force constant for $N_2@C_{60}$ and its comparison to N_2 in gas phase. In the harmonic approximation of an interatomic potential, the force constant is a measure of the force of attraction between the atoms. Since the attractive interatomic force in the electronically excited state of N_2 is weaker than in the ground state, the force constant is

also reduced, for both the molecule in gas phase and in the cage. However, as seen in the Table 4.6 the force constant difference (Δk) between N_2 in gas phase and in the cage differs, it is reduced by twice when N_2 is in the cage, from 12 to 5.7. Indicating that the interaction of two nitrogen atoms when encapsulated in the cage is weakened when compared to the gas phase.

4.6 Vibrationally Resolved XAS of $N_2@C_{60}$

To describe the vibrational motions within molecules, normal modes are used. Each normal mode is an independent motion of atoms in a molecule which does not affect the movement of the other modes and is orhtogonal to other modes. The number of normal modes within molecule will depend on the number of atoms and for $N_2@C_{60}$ there are 180 normal modes (following the formula for vibrational degrees of freedom which is equal to $3M - 6$, where M represents number of nuclei in the molecule). All 180 normal modes are expected to contribute to the spectra of $N_2@C_{60}$. Figure 4.4 shows spectra for $N_2@C_{60}$ with different peak widths: 0.0025 eV, 0.025 eV, and 0.08 eV. As can be seen with low width it is possible to see all the peaks involved in the spectra which correspond to the N_2 stretching mode, and also other normal modes of the carbon atoms. Increasing the peak width to 0.025 eV results in three main peaks with shoulders. Further increase in the peak width gives three smooth peaks which, based on their positions, can be identified with those obtained in the experimental XAS of free N_2 (Figure 4.1).

Table 4.7 shows the corresponding transitions assigned to the peak energies (shifted by 11.42 eV). It can be noticed that there are four transitions assigned from ground state to one, two, and three quanta in 179^{th} vibrational mode of the first excited state ($0(0) \rightarrow 1(1v179)$; $0(0) \rightarrow 1(2v179)$, and $0(0) \rightarrow 1(3v179)$). The v179 mode corresponds to the N_2 stretching mode. The differ-

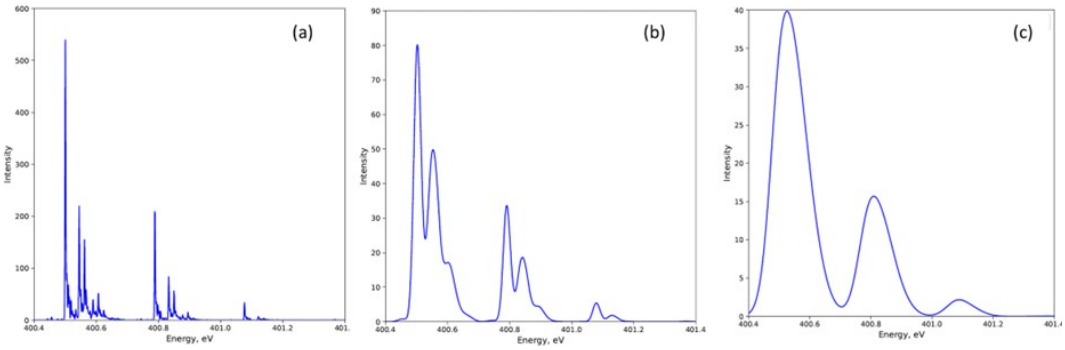


Figure 4.4: *Vibrationally resolved N 1s XAS of N_2@C_{60} simulated using TDDFT with the B3LYP functional and different basis sets and plotted with (a)* 0.0025 eV*, (b)* 0.025 eV*, and (c)* 0.08 eV *peak width.*

ence in the shift between the peaks is equal to 0.29 eV, which is higher than for N_2 in gas phase (0.27 eV). However, around those values, there are other transitions which involve the normal mode corresponding to N_2 and other normal modes corresponding to the carbon atoms within the cage. For instance, at 400.82 eV the assigned transition corresponds to $0(0) \rightarrow 1(1v4,1v179)$, which means transition from ground state to one quanta of the fourth vibrational normal mode and to the first quanta of 179^{th} normal mode of the first excited state. The 179^{th} vibrational normal mode corresponds to N_2 while the fourth vibrational normal mode belongs to some of the carbon atoms within the cage. This indicates that the carbon cage also contributes to the spectra of N_2@C_{60}.

Figure 4.5 shows the absorption spectra for N_2 and N_2@C_{60} generated by convoluting the calculated excitation energies with Lorentzian functions. As can be seen, the energy for N_2@C_{60} increases by 0.03 eV for the $0 \rightarrow 1(1v0)$ transition and further by 0.03 eV for the $0 \rightarrow 1(2v0)$ transition. There is also difference in the shift between the peaks when compare with N_2 in the phase gas and in the cage. One of the explanations for that could be the difference between the force constant for the N_2 stretching mode calculated previously (Table 4.6). A smaller force constant for N_2 will result in smaller value of β in Morse functional approximation (Eq. 1.1) and a broader potential well. N_2 will have smaller potential well. This could explain the results showing that

Table 4.7: Vibrational transitions in $N_2@C_{60}$ and corresponding energies calculated using the parallel normal modes approximation.

Energy/eV	Transition
400.5000	0(0) → 1(0)
400.5447	0(0) → 1(1v10)
400.5492	0(0) → 1(2v2)
400.5674	0(0) → 1(2v4)
400.5886	0(0) → 1(2v8)
400.5887	0(0) → 1(2v9)
400.5893	0(0) → 1(2v10)
400.5983	0(0) → 1(4v2)
400.6062	0(0) → 1(1v10,1v26)
400.6120	0(0) → 1(2v3,1v10)
400.6121	0(0) → 1(2v4,1v10)
400.6165	0(0) → 1(2v2,2v3)
400.6231	0(0) → 1(2v26)
400.6285	0(0) → 1(2v0,1v10,1v26)
400.6289	0(0) → 1(2v3,1v26)
400.6289	0(0) → 1(2v4,1v26)
400.6340	0(0) → 1(3v10)
400.6347	0(0) → 1(4v3)
400.6385	0(0) → 1(2v2,2v10)
400.6399	0(0) → 1(1v4,1v10,1v26)
400.6423	0(0) → 1(1v10,1v84)
400.6509	0(0) → 1(2v10,1v26)
400.6554	0(0) → 1(2v2,1v10,1v26)
400.6567	0(0) → 1(2v3,2v10)
400.6591	0(0) → 1(1v26,1v84)
400.6678	0(0) → 1(1v10,2v26)
400.6736	0(0) → 1(2v3,1v10,1v26)
400.6846	0(0) → 1(3v26)
400.7883	0(0) → 1(1v179)
400.8105	0(0) → 1(2v0,1v179)
400.8220	0(0) → 1(1v4,1v179)
400.8228	0(0) → 1(1v7,1v179)
400.8329	0(0) → 1(1v10,1v179)
400.8374	0(0) → 1(2v2,1v179)
400.8498	0(0) → 1(1v26,1v179)
400.8552	0(0) → 1(2v0,1v10,1v179)
400.8556	0(0) → 1(2v3,1v179)
400.8557	0(0) → 1(2v4,1v179)
400.8666	0(0) → 1(1v4,1v10,1v179)
400.8721	0(0) → 1(2v0,1v26,1v179)
400.8776	0(0) → 1(2v10,1v179)
400.8821	0(0) → 1(2v2,1v10,1v179)
400.8835	0(0) → 1(1v4,1v26,1v179)
400.8859	0(0) → 1(1v84,1v179)
400.8945	0(0) → 1(1v10,1v26,1v179)
400.8990	0(0) → 1(2v2,1v26,1v179)
400.9003	0(0) → 1(2v3,1v10,1v179)
400.9114	0(0) → 1(2v26,1v179)
400.9172	0(0) → 1(2v3,1v26,1v179)
400.9223	0(0) → 1(3v10,1v179)

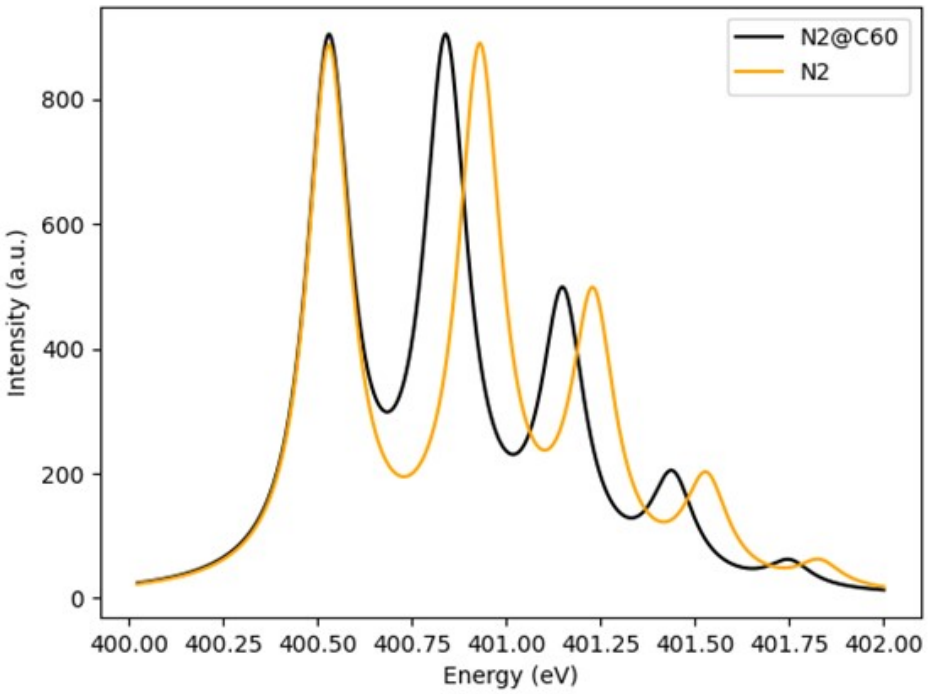


Figure 4.5: *Vibrationally resolved N 1s XAS of N_2 and $N_2@C_{60}$ simulated using TDDFT with the B3LYP functional and 6-31++G** basis set.*

the spacing between the level increases in case of $N_2@C_{60}$ (from 0.27 eV to 0.29 eV).

Figures 4.6 shows the calculated absorption spectra of $N_2@C_{60}$ compared to the experimental one. It shows differences when compared to experimental data, especially in the shift between the second and third, and third and fourth peaks, which can indicate the role of anharmonicity. To predict accurately the spectra, anharmonic corrections might be required.

4.7 Conclusion

The vibrationally resolved X-ray emission spectra of the N_2 molecule in gas phase was simulated using DFT-based approaches. Comparison with experimental results showed that TDDFT with the B3LYP hybrid functional and 6-31++G** basis set provides the most accurate description of the measured

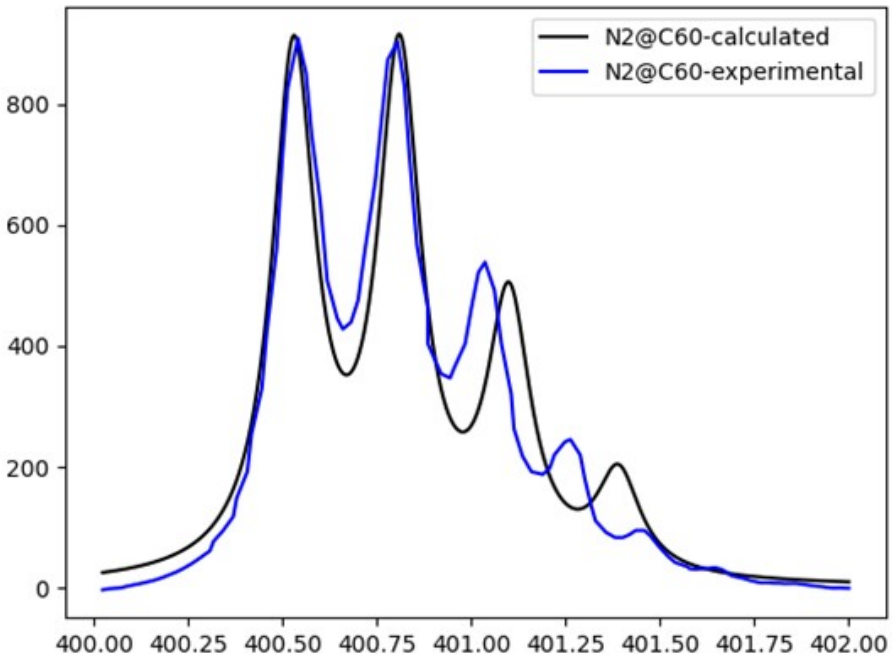


Figure 4.6: *Vibrationally resolved N 1s XAS of $N_2@C_{60}$ simulated using TDDFT with the B3LYP functional and 6-31++G** basis set, compared to experimental results.*

spectra among the studied methods. This approach was applied to study $N_2@C_{60}$ in order to probe the sensitivity of the spectra to the presence of the C_{60} cage. The results of the calculations highlighted that the spectra for $N_2@C_{60}$ are dominated by the bands arising from transitions from σ orbitals that are localised on the N_2 molecule to the π^* orbitals that are localised predominantly on N_2 but also in small percentage on the C_{60} cage. This interaction between N_2 and C_{60} results in the shift for peaks at higher energies for the $0(0) \rightarrow 1(2v0)$ and $0(0) \rightarrow 1(3v0)$ vibronic transitions. The calculated spectra for $N_2@C_{60}$ differ slightly from the experimental observations. This discrepancy is thought to be due to the harmonic approximation used in the present calculations. Including anharmonicity in the calculation could potentially improve the accuracy of the results. The result also show that the presence of C_{60} cage does not influence the bond length of encapsulated N_2. However, the difference in the frequency between ground and excited state of

N_2 is reduced by almost twice when N_2 is encapsulated in the C_{60} cage. This could indicate that in the presence of the cage less energy is required for the vibronic transition of N_2. The force constant difference between ground and excited state of N_2, for N_2 encapsulated in the cage, is also reduces. Indicating that the interaction between two nitrogen atoms when encapsulated in the cage is weaker when compared to the gas phase.

Chapter 5

TD-DFT study of the X-ray emission spectroscopy of amino acids and proteins

5.1 Introduction

Amino acids are the fundamental building blocks of nature and combine together to form proteins, and this biological significance has led to an interest in understanding their geometrical and electronic structure. Chiroptical spectroscopic methods are commonly used to probe the structure of oligopeptides and proteins.[221] These methods are based on differential absorption of chiral molecules with left- and right-circularly polarized light. Despite offering much lower resolution than solid-state X-ray diffraction, the fast timescales accessible to these techniques allows processes such as folding and unfolding processes to be studied.[222,223] For instance, by combining natural circular dichroism (CD) spectroscopy with nuclear magnetic resonance (NMR), Buck *et al.*,[222] has observed a transition to a new and partially structured state of a protein lysosome after addition of 2,2,2 – trifluoroethanol at pH 2.0 at 27°C to the protein solu-

tion.While Nielsen *et al.*,[223] have investigated, among other factors, the effect of pH on insulin fibril formation and found out, by obtaining near-UV CD spectra of insulin, some loss of tertiary structure under conditions of low pH. Natural circular dichroism (CD) spectroscopy in the ultraviolet region is widely used in this regard since the different elements of secondary structure, helix, β-sheet and turn, have characteristic spectral profiles.[221]

In recent years, spectroscopic techniques using X-rays have emerged as a powerful analytical tool driven by the increasing availability of synchrotron sources and free-electron lasers. This raises the question of whether spectroscopic measurements in the X-ray region are able to distinguish between different elements of secondary structure. There have been a number of studies on the X-ray absorption spectroscopy, or more specifically the near edge X-ray absorption fine structure (NEXAFS), of amino acids and small polypeptides.[218,224–227] including molecules such as glycine,[225] glycyl-glycine,[225] methionine,[218] and proline.[218] Although the fingerprinting character of individual units of 20 amino acids commonly occurring in nature have been determined, it has been found that, in general, these spectra are not sufficiently different for chemical identification.[224] This work has been extended to consider protein secondary structure models, where it was concluded that there are relatively small differences in the computed NEXAFS spectra at the carbon and oxygen K-edges, with the greatest difference predicted to occur at the nitrogen K-edge.[228] In addition, based on TDDFT calculation in conjunction with a short-range corrected exchange–correlation functional designed for core excitations, the NEXAFS of glycine, alanine and glycyl-glycine have been obtained and found to be in good agreement with experiment.[228] Other computational studies have considered X-ray natural circular dichroism (XNCD) of amino acids,[229–233] including using the static-exchange (STEX) approximation[229] and the complex polarization propagation method in conjunction with density functional theory (DFT).[230,232] Using that approach, the XNCD spectra of carbon,

nitrogen, and oxygen in the neutral and zwitterionic forms of L-alanine have been obtained.[230] It has been shown that XNCD has a greater sensitivity to the type of amino acid compared with X-ray absorption spectroscopy, and the potential to be a better technique to fingerprint these compounds.

The focus of this chapter is X-ray emission spectroscopy (XES), and the XES of glycine on the Cu(110) surface has been studied.[21] More recent work has probed the XES and resonant inelastic X-ray scattering (RIXS) of amino acids in aqueous solution[234–236] and the solid state.[237,238] In particular, Weinhardt and co-workers have presented a detailed characterisation of the XES and RIXS of amino acids. This includes a library of spectra for all proteinogenic amino acids,[238] the development of a building block model[236] and the study of peptides.[239]

In parallel with the advances in experimental measurements, there have also been developments in the calculation of X-ray emission spectra using quantum chemical methods, such as Kohn-Sham density functional theory (DFT) and time-dependent density functional theory (TDDFT).[22,55] These calculations can play an important role in enabling the understanding and interpretation of experimental data. In this work, the accuracy of DFT-based methods for the simulation of X-ray emission spectra of amino acids, in particular assessing the relative accuracy of simulated spectra based upon DFT and TDDFT calculations are examined. Subsequently TDDFT is applied to study the XES of polypeptides and fragments of protein secondary structure to investigate the dependence of the spectra on the structure of the peptide bond.

5.2 Computational Methods

Non-resonant XES measures the emission following ionisation of a core electron, XES can also be performed under resonant conditions where the emission

from a core-excited state, rather than core-ionised state, is measured. Within the framework of DFT, the transition energies and the associated intensities can be determined directly from the Kohn-Sham DFT calculation by approximating the transition energy as the energy difference between the orbital energies of the neutral ground state molecule

$$\Delta E = \epsilon_v - \epsilon_c \tag{5.1}$$

with the oscillator strength given by

$$f \propto |\langle \phi_c | \hat{\boldsymbol{\mu}} | \phi_v \rangle|^2 \tag{5.2}$$

where ϕ_c is a core orbital and ϕ_v is a valence orbital. This approach takes no account of the orbital relaxation for the core-ionised state, but despite of this approximation, it has been applied successfully in a variety of applications, including the probing the chemical bonding of molecules on surfaces,[31,240] valence-to-core XES of transition metal complexes[241,242] and the study of carbon nanostructures.[243] A semi-classical Kramers-Heisenberg (SCKH) approximation that captures vibrational interference effects has been developed,[244] and applied to study liquids,[245,246] and damped coupled-cluster response theory methods have also been developed.[247] XES can also be determined using TDDFT through the use of a reference determinant with a core-hole,[248] and this approach has been used to study the valence-to-core XES of transition metal complexes[249–252] and water.[33,253] The advantage of this approach is that the core-hole relaxation is incorporated explicitly. This strategy of using a core-hole reference determinant is not limited to TDDFT calculations and has also been exploited within ADC[254] and EOM-CCSD formalisms.[255] An important consideration in these calculations is that the basis set is able to describe the core-ionised state.[256] Recently is has been proposed that the basis set be augmented through the addition of the core and valence (not polarisation) ba-

sis functions for the element with one higher nuclear charge.[257] This is only necessary for the element being ionised, and the resulting basis sets are termed (Z+1) basis sets.

For both neutral and zwitterionic forms of glycine, X-ray emission spectra were computed for the nitrogen and oxygen K-edges using DFT (i.e. via equations 5.1 and 5.2) and TDDFT. The structure of glycine was optimised at the B3LYP/6-31G* level, and for the DFT spectra the long-range corrected CAM-B3LYP[52] and short-range corrected SRC1R1[53] exchange-correlation functionals were used with 6-311G* basis set. TDDFT spectra were computed using the B3LYP[258] and CAM-B3LYP functionals and the (Z+1)6-311G* basis set, where the additional basis functions were included only for the element being ionised. In these calculations the maximum overlap method[60] was used to maintain the core-hole during the DFT calculation. For comparison, spectra were also determined using the EOM-CCSD method with the (Z+1)6-311G* basis set. Further TDDFT/CAM-B3LYP calculations for alanine, cysteine and proline were performed using a similar approach. All of the calculations on the zwitterionic forms of the amino acids used the polarised continuum model (PCM)[259] with a dielectric constant of 78.39. Spectra have also been computed that include averaging over structures generated from an ab initio molecular dynamics (AIMD) simulation of the core-ionised state. These calculations sample 50 structures extracted at uniform time intervals from a 5 fs (which reflects the typical lifetime of the core-ionised state)[260] AIMD simulation using the CAM-B3LYP functional and (Z+1)6-311G* basis set for the appropriate core-ionised state. Spectra have been generated by convoluting the calculated transition energies and intensities with Gaussian functions with full-width at half maximum (FWHM) of 0.25 eV, which accounts for many factors such as shake-up and Auger processes that are not described by the calculations. This FWHM is chosen to provide a visual representation of the computed spectra and has not been optimised to fit the experimental data.

5.3 XES of Amino Acids

Despite its small size, the molecular structure of glycine shows a complex behaviour. In the gas-phase the carboxylic acid (COOH) and amino (NH_2) groups are uncharged, which we refer to as the neutral form, while in the solid state glycine exists as the zwitterionic form (COO^- and NH_3^+). In solution the charge state of the carboxylic acid and amino groups depends on the pH of the solution. Figures 5.1 and 5.2 show the computed X-ray emission spectra for the zwitterionic and neutral forms of glycine determined with a range of computational approaches.

The formally the most accurate method used is EOM-CCSD/(Z+1)6-311G* and the corresponding spectra are used as a benchmark to assess the DFT-based calculations. The transition energies calculated using DFT and TDDFT show a wide variation, from being systematically too high to systematically too low. This is expected, and has been discussed previously in the literature.[242,248] As a consequence, in Figures 5.1 and 5.2 the spectra have been shifted in energy to align with the EOM-CCSD spectra and we focus on the ability of the DFT-based methods to describe the spectral profile correctly, with the understanding that a constant energy shift can be applied to align the spectra with experiment.

For both the nitrogen and oxygen K-edge, the spectra computed directly from the DFT calculation using the CAM-B3LYP and SRCr1 functionals show the greatest deviation from the EOM-CCSD spectra, and overall provide a poor description for both neutral and zwitterionic forms. The spectra predicted by the two functionals, which are very different in nature, are similar to each other suggesting that the source of the observed discrepancy is the approach for determining the transition energies and intensities rather than the functionals themselves. In particular, for the zwitterionic form the calculated intensity is low for the higher energy bands in the nitrogen K-edge spectra, which is not

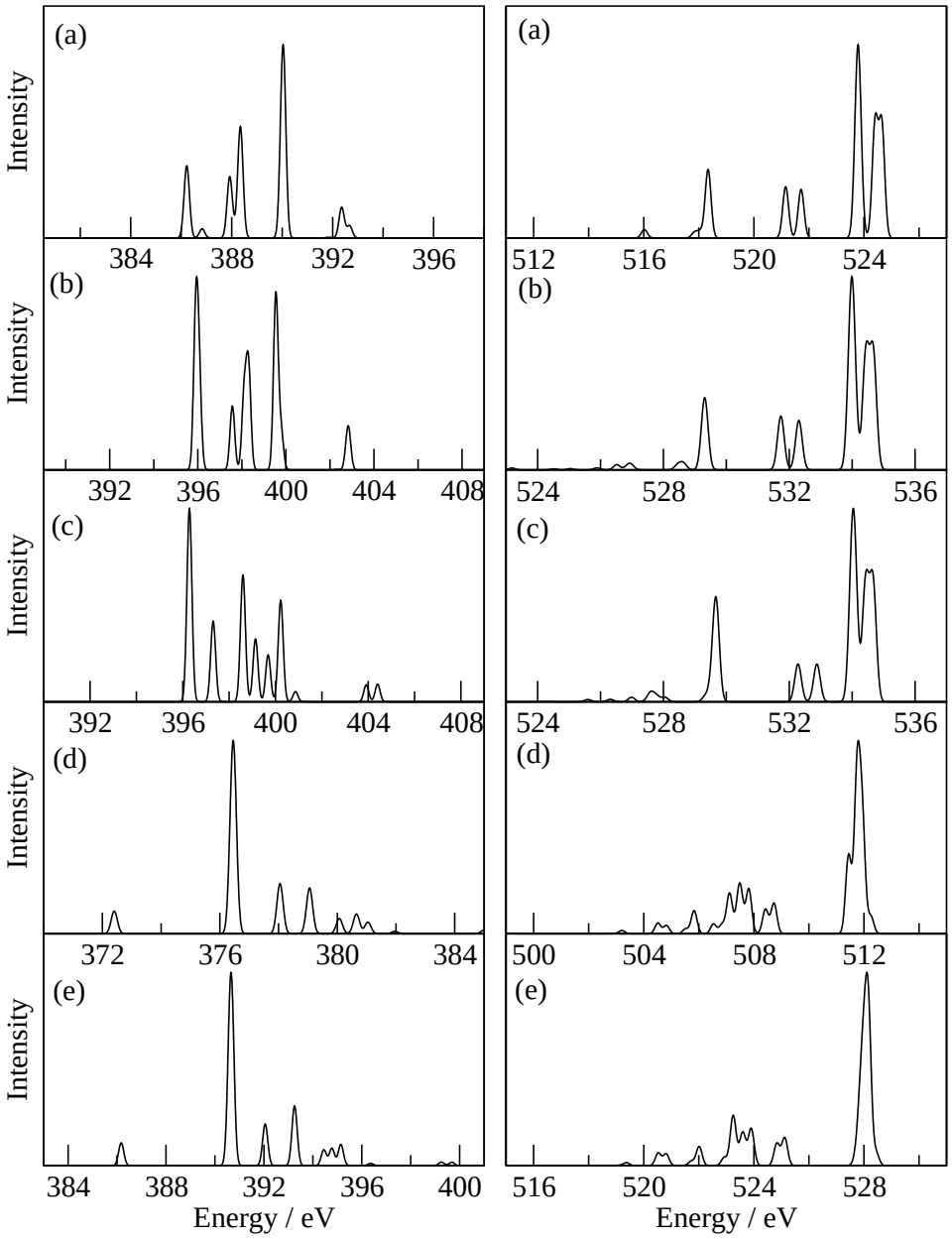


Figure 5.1: *Calculated non-resonant X-ray emission spectra the zwitterionic form of glycine at the nitrogen K-edge (left) and oxygen K-edge (right). (a) EOM-CCSD/(Z+1)6-311G* (b) TDDFT-CAM-B3LYP/(Z+1)6-311G* (c) TDDFT-B3LYP/(Z+1)6-311G* (d) DFT-CAM-B3LYP/6-311G* (e) DFT-CAM-SRC1R1/6-311G*.*

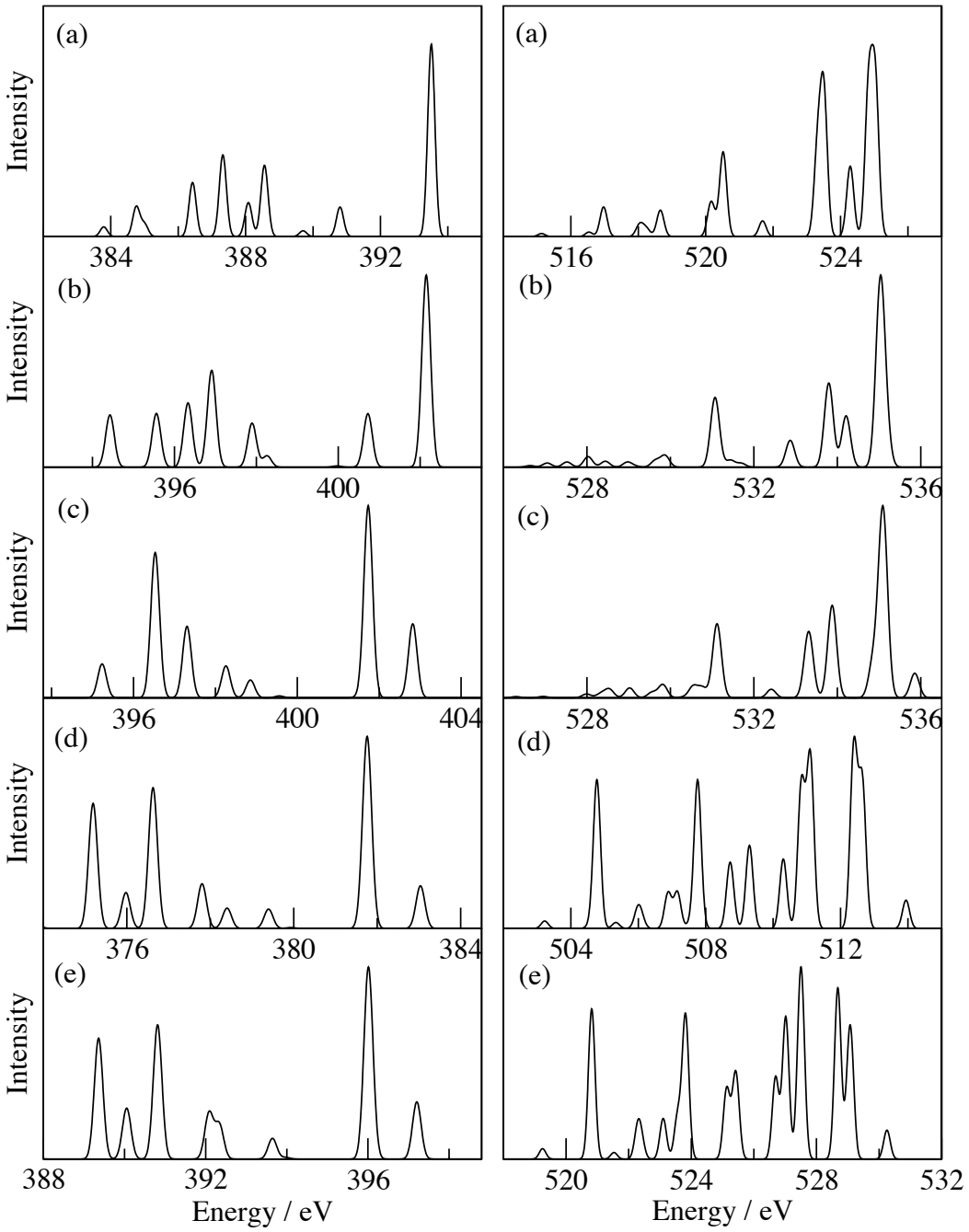


Figure 5.2: *Calculated non-resonant X-ray emission spectra the neutral form of glycine at the nitrogen K-edge (left) and oxygen K-edge (right). (a) EOM-CCSD/(Z+1)6-311G* (b) TDDFT-CAM-B3LYP/(Z+1)6-311G* (c) TDDFT-B3LYP/(Z+1)6-311G* (d) DFT-CAM-B3LYP/6-311G* (e) DFT-CAM-SRC1R1/6-311G*.*

consistent with experiment (see later). This has also been observed in previous calculations,[235] although this was improved through the consideration of effects of molecular dynamics along the core-ionised trajectory.

The nitrogen and oxygen K-edge spectra computed using TDDFT show a closer agreement with the EOM-CCSD spectra. This is perhaps not surprising since there is a much greater similarity in the approaches to determining the spectra. A closer examination of the spectra for the two functionals shows that there is little variation between the calculated spectra at the oxygen K-edge, while there are significant differences for the nitrogen K-edge where CAM-B3LYP provides a significantly better description of the EOM-CCSD spectra.

This is consistent with recent work that found CAM-B3LYP to give accurate spectra for a range of organic molecules in a comparison with experimental data.[261] In particular, for the nitrogen K-edge of the zwitterionic form CAM-B3LYP and EOM-CCSD methods predict high intensity for the higher energy bands, in contrast to the B3LYP spectrum. The agreement between CAM-B3LYP and EOM-CCSD for the neutral form is slightly poorer than for the zwitterionic form, however, the discrepancy is primarily associated with the predicted intensities rather than the relative energy of the bands.

It is also important to compare the computed spectra with experimental data. Experimental measurements have been reported for the 20 most common proteingenic amino acids in their solid zwitterionic forms,[238] and as a consequence we focus on the zwitterionic forms of the amino acids. The calculations on glycine suggest that the TDDFT/CAM-B3LYP approach provides a good description of the EOM-CCSD spectra. This is significant since the lower computational cost of TDDFT means that this approach can be readily applied to study larger systems.

Figure 5.3 shows computed TDDFT/CAM-B3LYP spectra for glycine, alanine, cysteine and proline. The resulting spectra show that at the oxygen K-

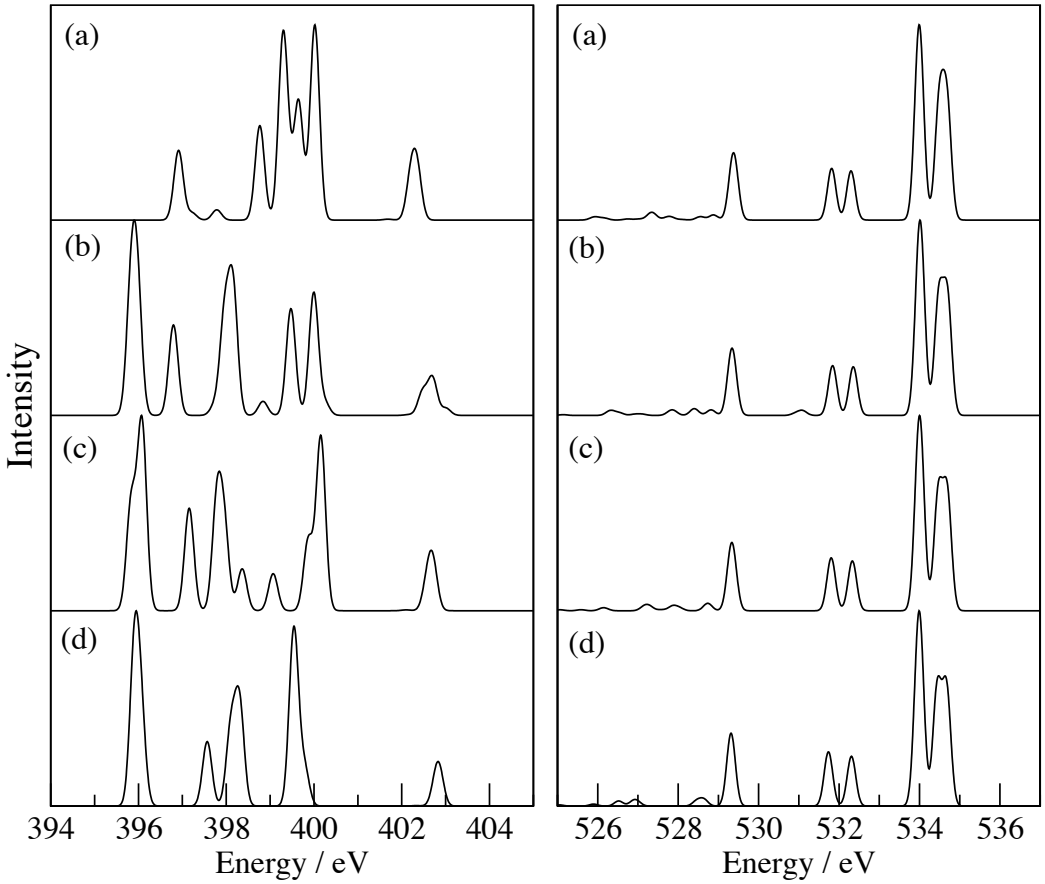


Figure 5.3: *Calculated TDDFT/CAM-B3LYP non-resonant X-ray emission spectra of the zwitterionic forms of (a) proline, (b) cysteine, (c) alanine and (d) glycine at the nitrogen K-edge (left) and oxygen K-edge (right).*

edge there is little variation between the spectra for the different amino acids. This is consistent with the experimental observations and reflects the nature of the COO^- group which is relatively unaffected by the changes in the amino acid structure. For the nitrogen K-edge there are only small variations in the spectra for glycine, alanine and cysteine, but there is a significant change for proline which results from the changing nature of the bonding to nitrogen in proline, where the amino group is part of the heterocycle, in contrast to the other amino acids.

Figure 5.4 shows a direct comparison for glycine and proline of the computed TDDFT/CAM-B3LYP spectra with experimental spectra, which have been taken from reference 237.[238] In this comparison experimental spectra for the solid state are compared with spectra computed for single molecules with

the PCM describing the extended environment, so some variations may be expected, however, these differences are expected to be small.[239] An energy shift has been applied to the computed spectra to align the most intense bands with experiment, which results in a shift of −4.8 eV for nitrogen K-edge and −7.4 eV for the oxygen K-edge spectra.

Initially the spectra computed based upon the single ground state molecular structure was considered. The oxygen K-edge spectra are in good agreement with the experimental data for both glycine and proline. The largest discrepancy is for the peak labelled 3, which is too low in energy and only appears as a small shoulder in the experimental data. The molecular orbitals associated with the observed bands are shown in Figures 5.5, 5.6, 5.7, and 5.8. The intense band that dominates the experimental spectra comprises two components from orbitals with oxygen lone pair or π character at the carboxylic group, but crucially these orbitals have atomic p-orbital character around the oxygen atoms consistent with the large intensity for the transition to the oxygen 1s orbital.

The nitrogen K-edge spectra are more complex with a large number of transitions contributing to the broad band observed in experiment. However, in general the calculations predict bands that align with the distinct features observed in experiment. The peak labelled 1 corresponds to orbitals that are predominantly localised on the carboxylic acid group, and there is some evidence of a weak feature in the experimental spectra at this energy. For glycine, bands 2 and 5 are the most intense and arise from σ and π-type orbitals localised on the amino group. Also shown are spectra that incorporate the nuclear motions that occur on the femtosecond timescale in the core-ionised state. This leads to a relatively small change for the oxygen K-edge spectra, but larger changes are observed for the nitrogen K-edge leading to an improved agreement with the experimental data.

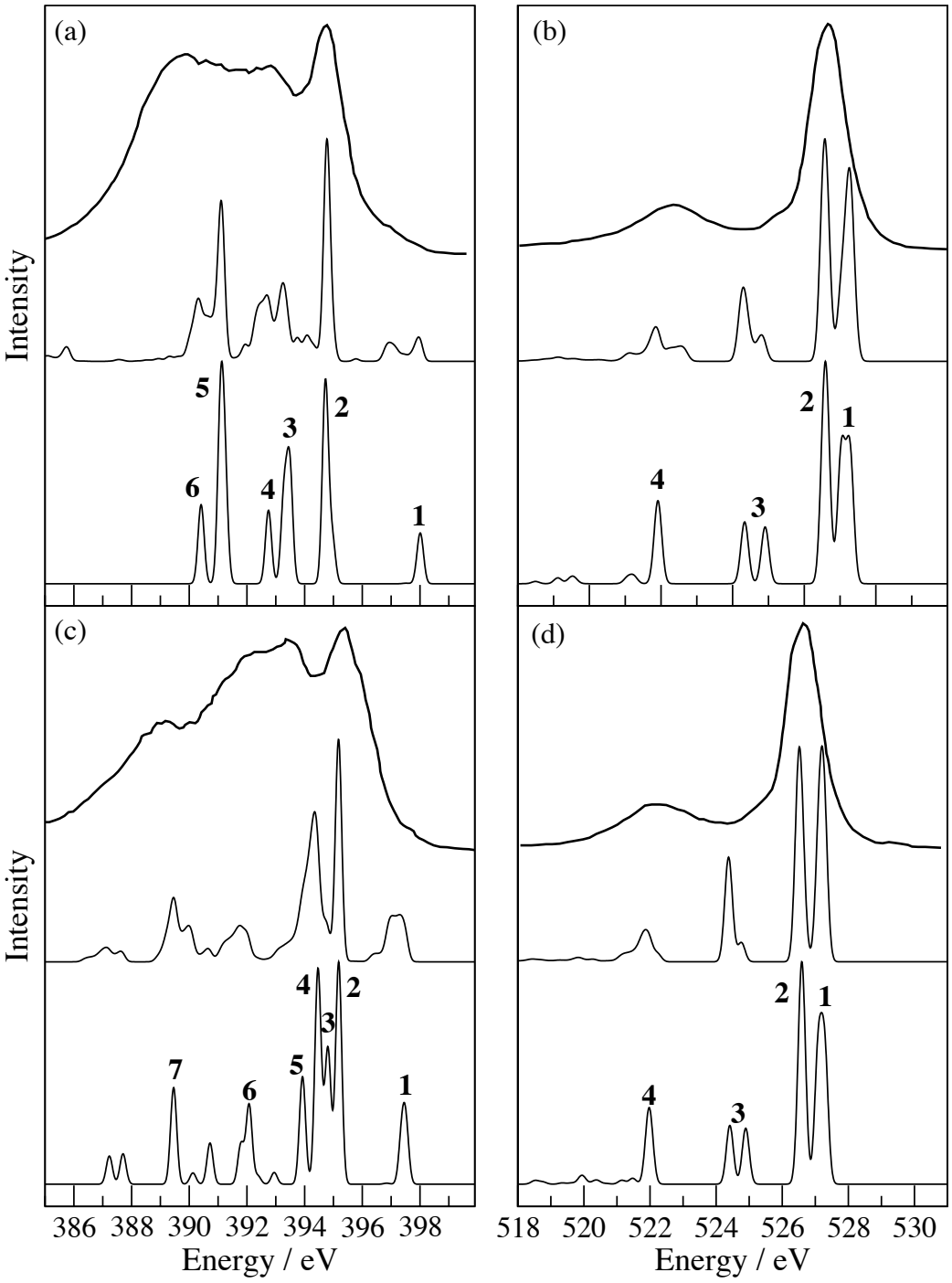


Figure 5.4: *Experimental and calculated TDDFT/CAM-B3LYP non-resonant X-ray emission spectra for the zwitterionic forms of (a) nitrogen K-edge glycine, (b) oxygen K-edge glycine, (c) nitrogen K-edge proline and (d) oxygen K-edge proline. Upper spectra: experiment adapted from reference,[238] middle spectra: calculated spectra including molecular dynamics and lower spectra: static (single structure) calculated spectra. An energy shift of* $-4.8\,\mathrm{eV}$ *for nitrogen and* $-7.4\,\mathrm{eV}$ *for oxygen have been applied to the calculated spectra to align them with experiment.*

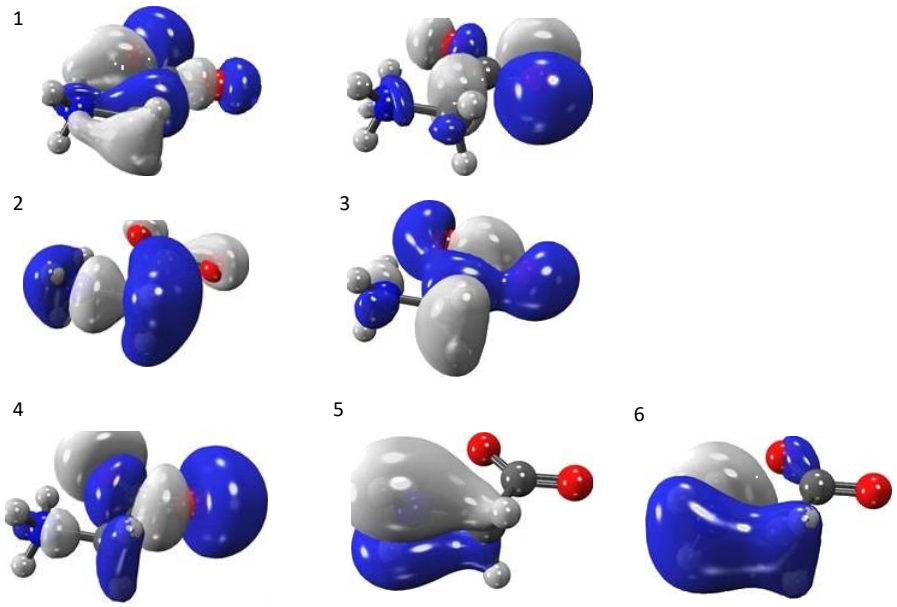


Figure 5.5: *Molecular orbitals associated with the observed bands in the nitrogen K-edge X-ray emission spectrum of the zwitterionic form of glycine calculated using TDDFT/CAM-B3LYP level of theory. Orbitals plotted with an iso-surface value of 0.08 using IQMol.*

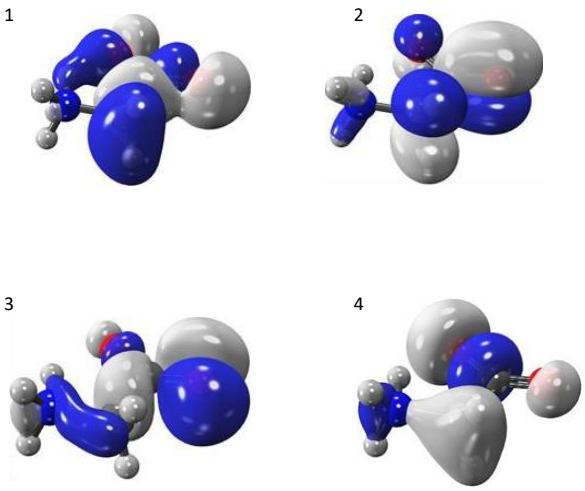


Figure 5.6: *Molecular orbitals associated with the observed bands in the oxygen K-edge X-ray emission spectrum of the zwitterionic form of glycine calculated using TDDFT/CAM-B3LYP level of theory. Orbitals plotted with an iso-surface value of 0.08 using IQMol.*

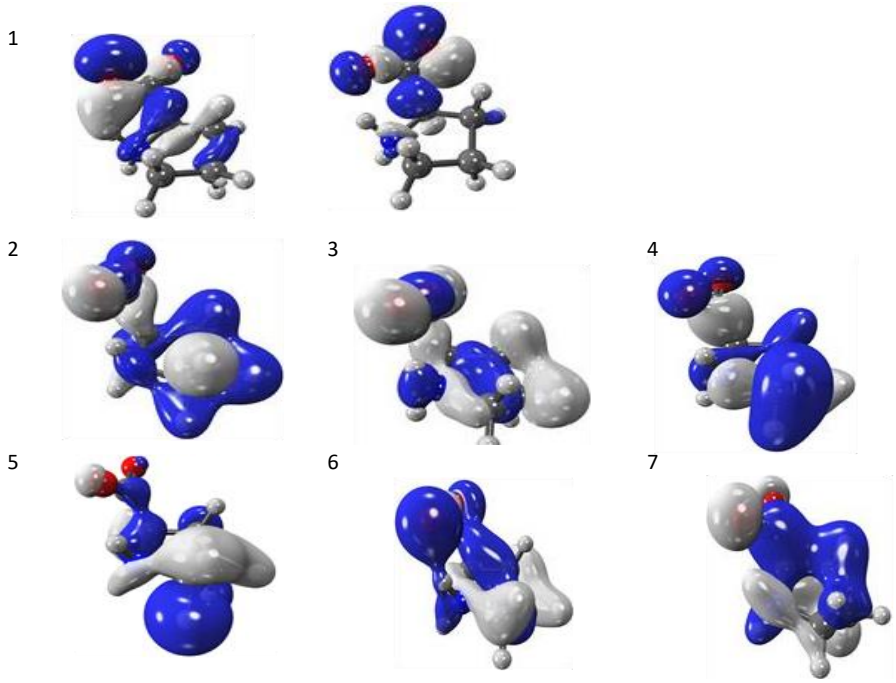


Figure 5.7: *Molecular orbitals associated with the observed bands in the nitrogen K-edge X-ray emission spectrum of the zwitterionic form of proline calculated using TDDFT/CAM-B3LYP level of theory. Orbitals plotted with an iso-surface value of 0.08 using IQMol.*

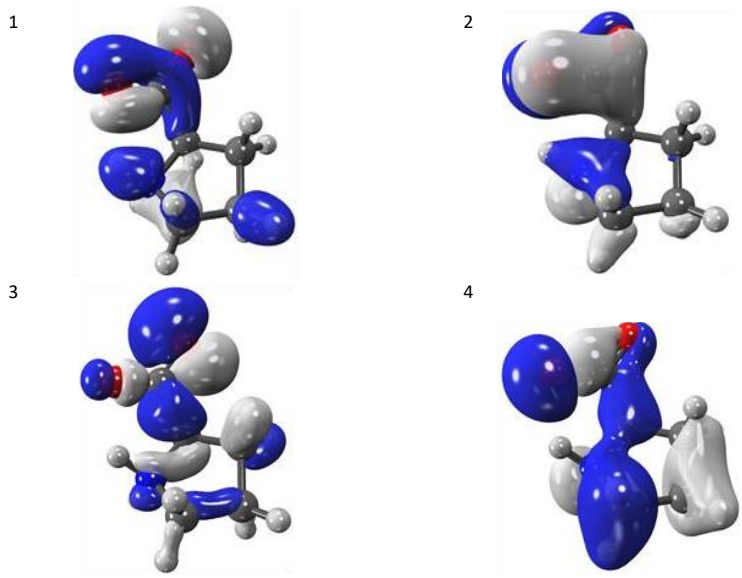


Figure 5.8: *Molecular orbitals associated with the observed bands in the oxygen K-edge X-ray emission spectrum of the zwitterionic form of prolinevcalculated using TDDFT/CAM-B3LYP level of theory.Orbitals plotted with an iso-surface value of 0.08 using IQMol.*

5.4 XES of Di-Amino Acids

Diglycine represents a simple system that contains the peptide bond. Figure 5.9 shows the computed nitrogen and oxygen K-edge TDDFT with CAM-B3LYP spectra for the zwitterionic form of diglycine along with the experimental data from reference 238.[239] To align the calculated spectra with experiment energy shifts of $-6.6\,\text{eV}$ and $-7.3\,\text{eV}$ have been applied for nitrogen and oxygen, respectively. The agreement between the computed spectra and experiment is very good. Figure 5.9 also shows the contribution to the spectra from the different nitrogen and oxygen atoms. For this purpose the two oxygen atoms of the COO^- group are treated together.

The most intense peak at the nitrogen K-edge is associated with the nitrogen atom of the peptide bond. This band arises from a π orbital on the peptide group that has a node between the carbon and the nitrogen, these orbitals are shown in Figure 5.10. The peptide nitrogen also contributes a peak at higher energy from orbitals that have σ character around the nitrogen atom. Two peaks (2 and 4) from the amino nitrogen are also evident in the spectrum. The orbitals associated with these peaks are similar in character to the orbitals that lead to the two most intense peaks in the spectrum for the zwitterionic form of glycine. For the oxygen K-edge spectra, the calculations show that both carbonyl and carboxylic acid group oxygens contribute to the dominant intense feature observed in the spectrum and the transitions arise from oxygen lone pair and π orbitals (Figure 5.11).

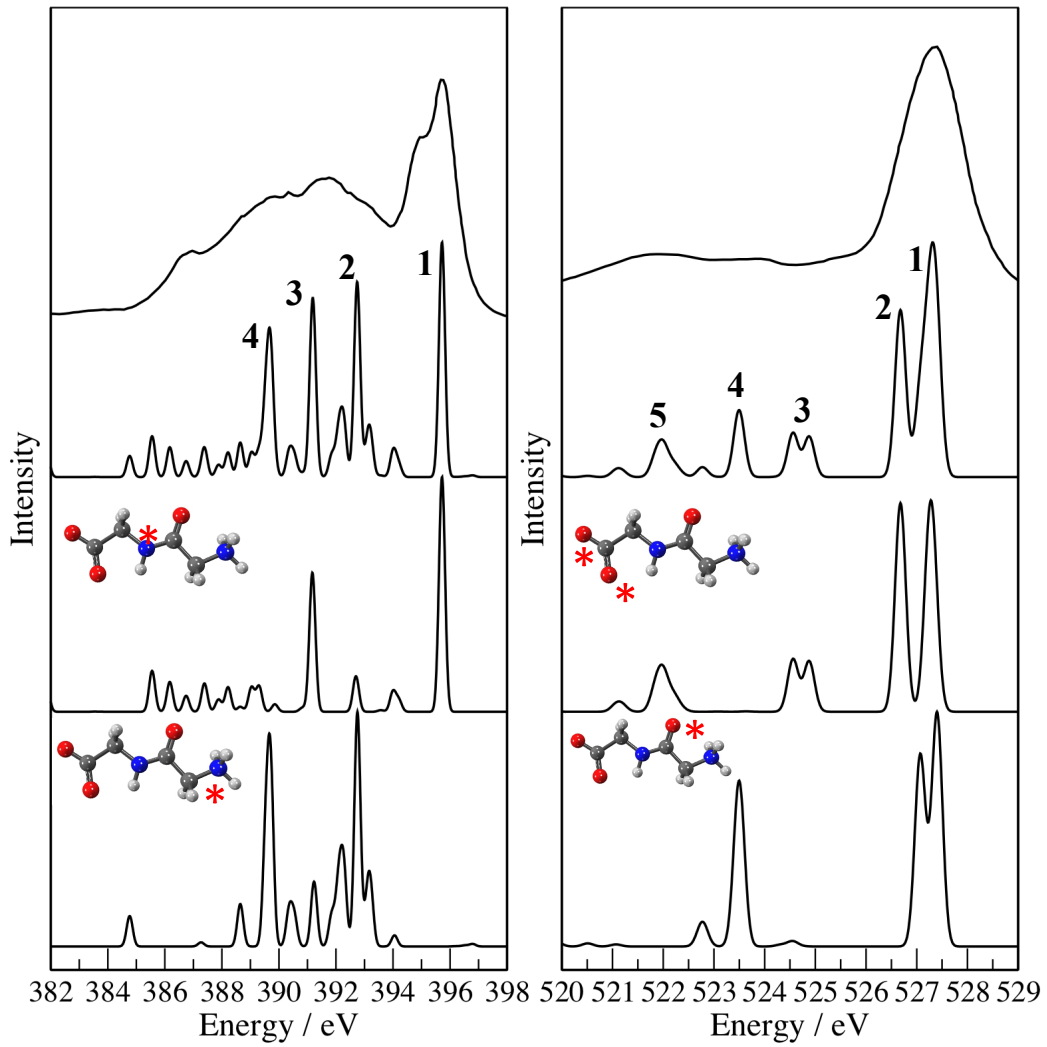


Figure 5.9: *Experimental and calculated TDDFT/CAM-B3LYP non-resonant X-ray emission spectra the zwitterionic form diglycine. Upper spectra: experiment taken from from reference 238.*[239] *The total computed spectrum and the contributions from the different nitrogen and oxygen atoms (indicated by an asterisk) are shown. An energy shift of* $-6.6\,\mathrm{eV}$ *for nitrogen and* $-7.3\,\mathrm{eV}$ *for oxygen has been applied to the calculated spectra to align them with experiment.*

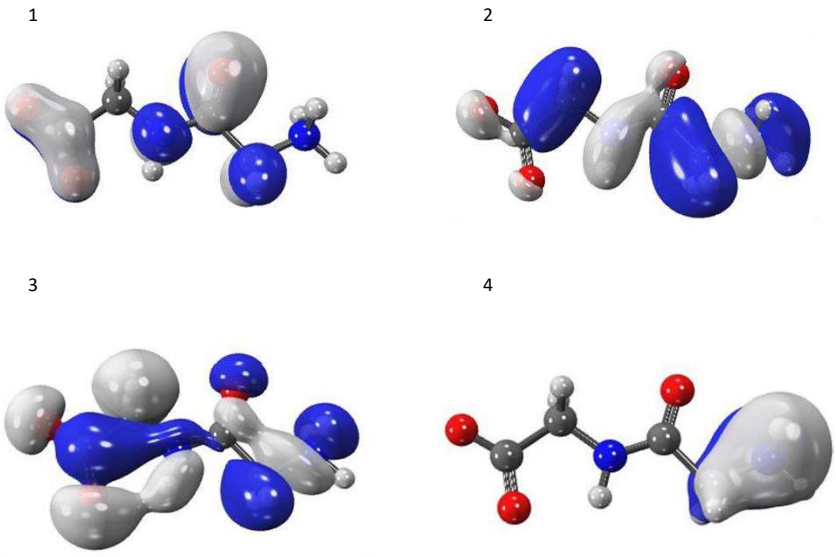


Figure 5.10: *Molecular orbitals associated with the observed bands in the nitrogen K-edge X-ray emission spectrum of the zwitterionic form of di-glycine calculated using TDDFT/CAM-B3LYP level of theory. Orbitals plotted with an iso-surface value of 0.08 using IQMol.*

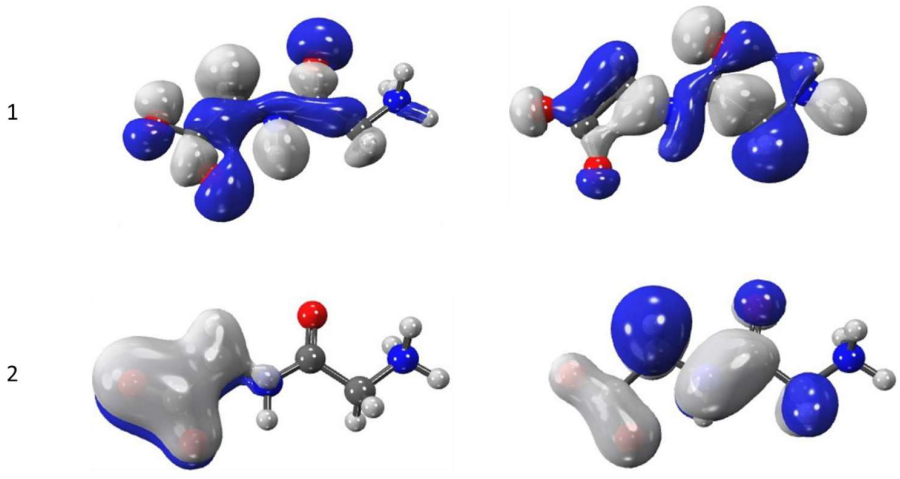


Figure 5.11: *Molecular orbitals associated with the observed bands in the oxygen K-edge X-ray emission spectrum of the zwitterionic form of di-glycine calculated using TDDFT/CAM-B3LYP level of theory. Orbitals plotted with an iso-surface value of 0.08 using IQMol.*

5.5 XES of Proteins

The biological significance of amino acids lies in their role in the structure of proteins. Previous computational studies have examined the near-edge X-ray absorption spectroscopy of different elements of protein secondary structure.[228] The computational cost of the TDDFT approach used here allows the study of quite large systems, and Figures 5.12 and 5.13 show calculated spectra for model α-helix and β-sheet structures. The α-helix contains ten glycine residues with ψ/ϕ angles of $-57°$ and $-48°$ and the computed spectra only considers core-ionisation occurring on the four central residues. The β-sheet structure has been extracted from the agitoxin protein (PDB code: 1AGT) with the side chains removed, and transitions associated with the end residues are not included. These structures are considered in isolation and the effects of solvent are not included. However, these calculations provide some insight into the sensitivity of XES to the structural variation of the peptide bond that occurs in the different elements of protein structure.

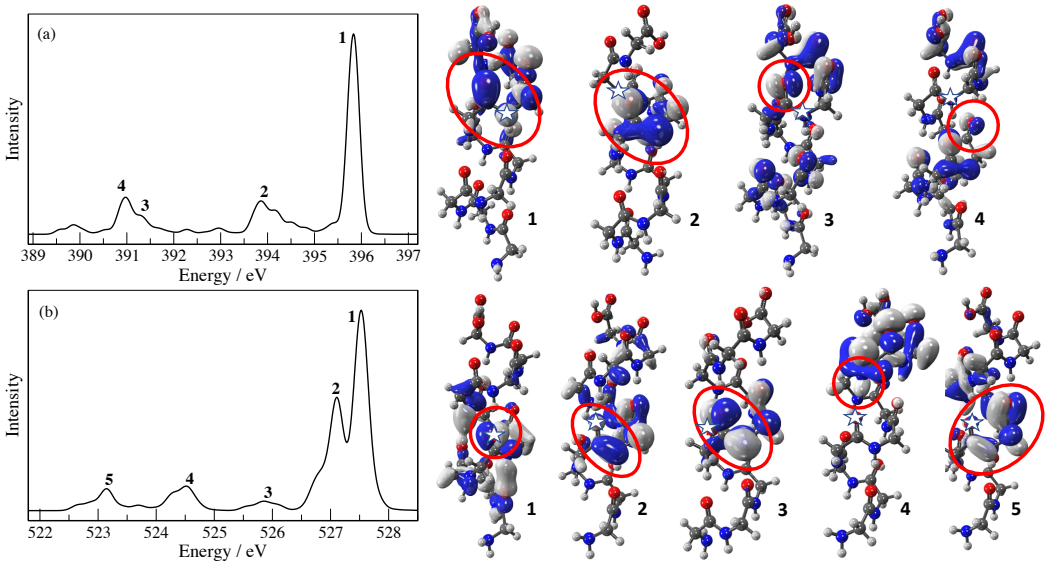


Figure 5.12: *Calculated non-resonant X-ray emission spectra for a model α-helix at the (a) nitrogen K-edge and (b) oxygen K-edge. Representative molecular orbitals associated with the labelled peaks are shown, where the star indicates the site of the core-hole in the initial state. An energy shift of -6.6 eV for nitrogen and -7.3 eV for oxygen has been applied to the calculated spectra.*

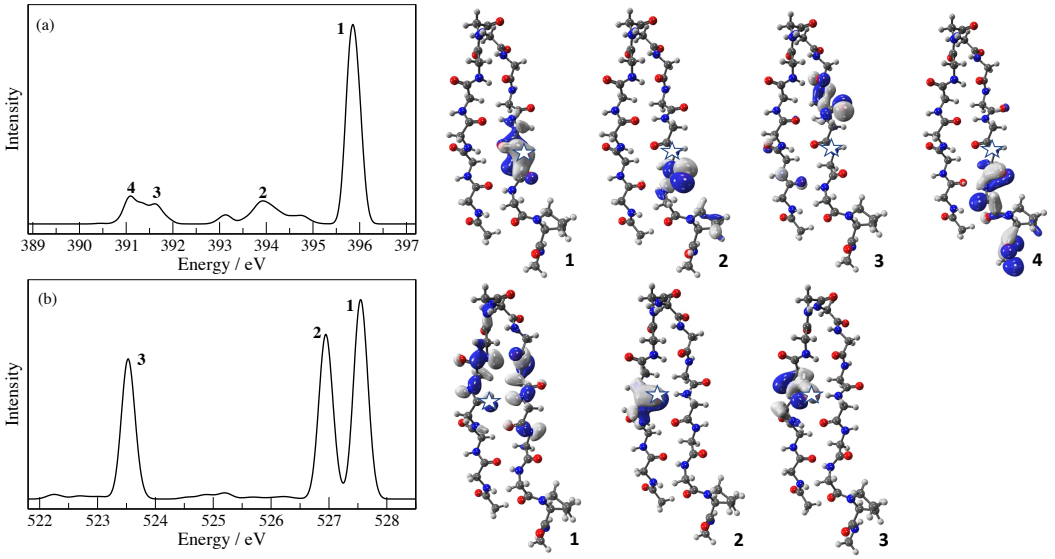


Figure 5.13: *Calculated non-resonant X-ray emission spectra for a β-sheet at the (a) nitrogen K-edge and (b) oxygen K-edge. Representative molecular orbitals associated with the labelled peaks are shown, where the star indicates the site of the core-hole in the initial state. An energy shift of* −6.6 eV *for nitrogen and* −7.3 eV *for oxygen has been applied to the calculated spectra*

The nitrogen K-edge spectrum for the α-helix shows one intense band which corresponds to the transition from a π-orbital localised on the same residue as the core-ionised nitrogen atom. This transition is similar to the one observed for diglycine. This peak will contain analogous contributions from all of the residues, which may occur at slightly different energies in a real helix. This is illustrated in Figure 5.14 which shows the separate contributions to the calculated spectra from the core-hole located at the different nitrogen atoms. At lower energies are several weaker bands. The peak labelled 2 arises from a transition from the π orbital on a neighbouring residue, while the remaining bands arise from transitions from oxygen lone pair orbitals on the same residue or on hydrogen bonded oxygen atoms. A similar analysis can be applied to the oxygen K-edge spectrum. The intense peaks (1 and 2) correspond to transitions from lone pair and π-orbitals localised on the same residue as the site of the core ionisation (Figure 5.15). Again the weaker peaks that lie at lower energies arise from transitions from neighbouring residues, this includes π-orbitals and orbitals associated with the hydrogen bonding N-H group. The nitrogen K-edge spectrum for the β-sheet is qualitatively similar to the one for

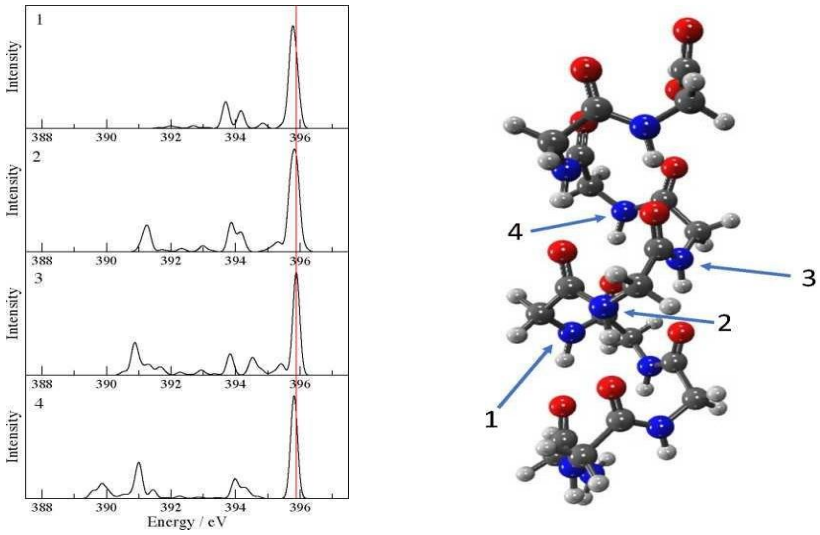


Figure 5.14: *Calculated nitrogen K-edge spectra for the initial core-hole located at different nitrogen atoms for the α-helix.*

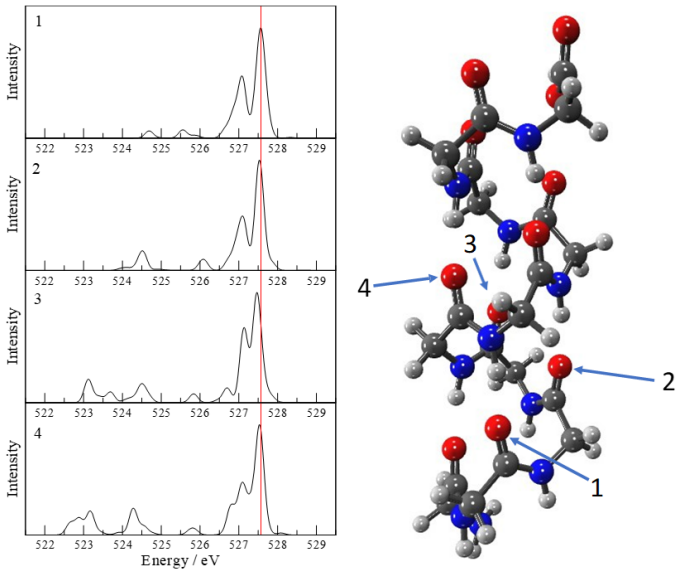


Figure 5.15: *Calculated oxygen K-edge spectra for the initial core-hole located at different oxygen atoms for the α-helix.*

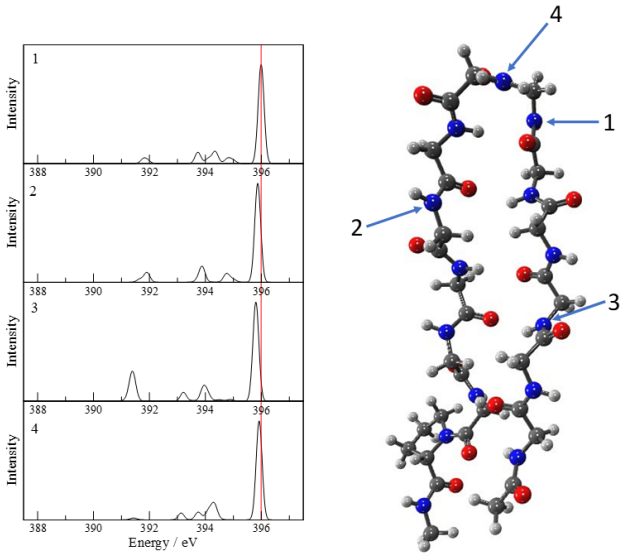


Figure 5.16: *Calculated nitrogen K-edge spectra for the initial core-hole located at different nitrogen atoms for the β-sheet.*

the α-helix. The intense peak arises from a transition from a π orbital localised on the residue which is the site of the core-ionisation and the weaker peaks at higher energies are associated with transitions from orbitals on neighbouring residues. The separate contributions to the total spectrum from the core-hole localised on different atoms is shown in Figure 5.16.

The oxygen K-edge spectra for the β-sheet shows some notable differences compared with the α-helix, with the lower energy peaks having significantly greater intensity. For this structure, all of the transitions arise from orbitals on the residue that has been core-ionised (Figure 5.17). A direct comparison between the spectra for the α-helix and β-sheet is shown in Figure 5.18. This shows very little variation in the spectra a the nitrogen K-edge, but greater variation in the higher energy bands at the oxygen K-edge.

5.6 Conclusions

The X-ray emission spectra of amino acids, a dipeptide and model α-helix and β-sheet structures have been simulated using DFT-based approaches. Com-

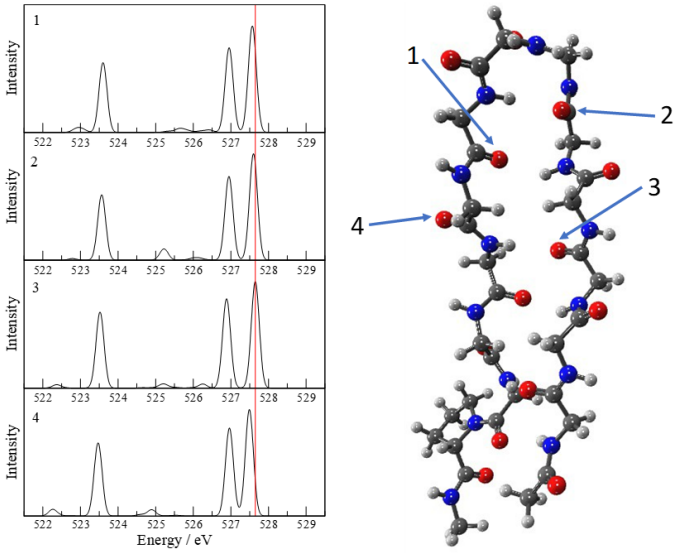


Figure 5.17: *Calculated oxygen K-edge spectra for the initial core-hole located at different oxygen atoms for the β-sheet.*

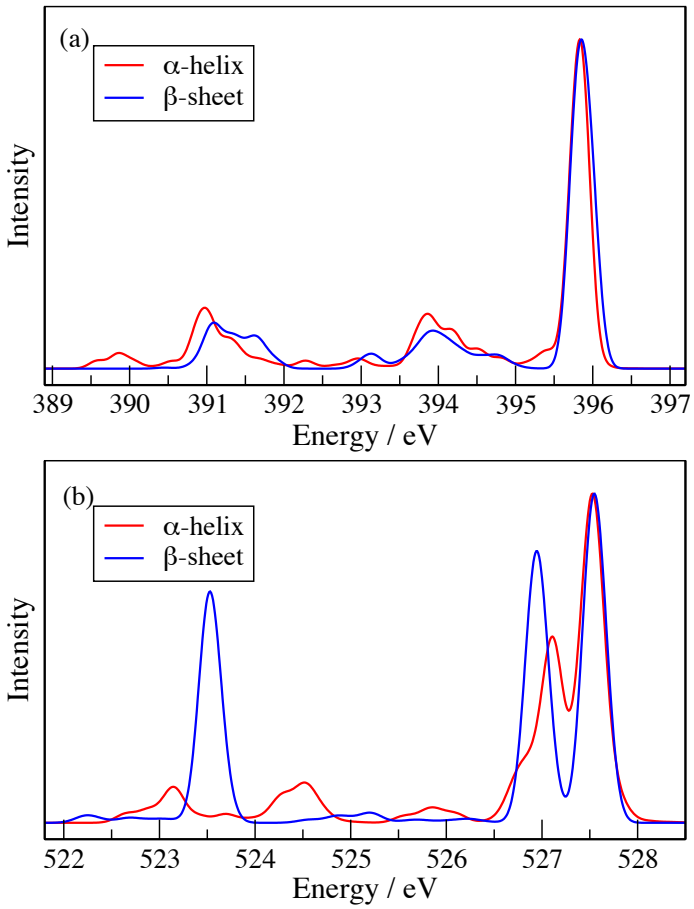


Figure 5.18: *Comparison of the calculated non-resonant X-ray emission spectra for the α-helix and β-sheet at the (a) nitrogen K-edge and (b) oxygen K-edge. An energy shift of −6.6 eV for nitrogen and −7.3 eV for oxygen has been applied to the calculated spectra*

parison with higher level calculations and experiment shows that TDDFT with the CAM-B3LYP exchange-correlation functional and (Z+1)6-311G* basis set provides the most accurate description of the spectra of the methods studied. This approach has been applied to study model α-helix and β-sheet structures in order to probe the sensitivity of the spectra to the geometric structure of the peptide bond. The calculations show that the spectra for the α-helix and β-sheet are dominated by intense bands arising from transitions from orbitals that are localised on the residue that is the site of the core-hole, and transitions from orbitals on neighbouring residues lead to weaker peaks at lower energies. At the nitrogen K-edge there is no significant variation between the calculated spectra for the α-helix and β-sheet structures, while at the oxygen K-edge there is some variation in the intensity of the bands at higher energies.

Chapter 6

Conclusions

This research has shown that using quantum chemical calculations, it is possible to characterise spectroscopic properties and to investigate absorption and emission spectra for a range of larger systems. Theoretical methods were employed to characterize the properties of QDs (up to 400 atoms) and investigate how quantum chemical calculations can lead to the in silico design of fluorescence sensors. This was explored in the context of QDs for the fluorescence sensing of dopamine based upon density functional theory DFT and time-dependent density functional theory TDDFT calculations. Analysis of the molecular orbital diagrams for the isolated molecules and calculations of the excited states of the dopamine-functionalized quantum dots (Si, Ge, and C) established the possibility of a photoinduced electron-transfer process by determining the relative energies of the electronic states formed from a local excitation on the QD and the lowest QD $\rightarrow$ dopamine electron-transfer state. The results suggested that among a wide range of studied QDs the $Si_{165}H_{100}$ and $Ge_{84}H_{64}$ QDs have the potential to act as fluorescent markers that could distinguish between the oxidized and reduced forms of dopamine, where the fluorescence would be quenched for the oxidized form. The results contribute to a better understanding of the optical and electronic behavior of QD-based

sensors and illustrate how quantum chemical calculations can be used to inform the design of QDs for specific fluorescent sensing applications.

The DFT-based approaches were also employed to investigate superatom molecular orbitals (SAMOs) of hydrogenated endohedral fullerenes to provide insights into the potential for design of novel advanced materials for molecular electronics. Using DFT and TDDFT calculations the electronic structures and energies of SAMO states of endohedral C_{60} and their dependence on the encapsulated atom type (Li and Ca) and the presence of hydrogen atoms on the fullerene surface were investigated. The DFT calculations showed that the presence of metal atoms lowers the LUMO-(s, p, d)-SAMO gaps of C_{60} and $C_{60}H_{60}$. While the presence of hydrogen atoms on the surface of the carbon cage lowers further the LUMO-d-SAMO gap, and more profoundly for $Ca@C_{60}H_{60}$. TDDFT calculations confirmed that the properties of the SAMOs in terms of shape and energy are quite sensitive to the type of atom and the presence of hydrogen on the surface of C_{60}. It was shown that the presence of hydrogen atoms on the surface of C_{60} lowers the excitation energy of SAMO states. In addition, it was observed that the HOMO of both $Li@C_{60}H_{60}$ and $Ca@C_{60}H_{60}$ adopted the characteristic s-SAMO shape. This property is important for designing fullerene-based devices for molecular electronics applications.

Using quantum chemical calculations X-ray absorption and X-ray emission spectra of two specific compounds was simulated. TDDFT with the B3LYP hybrid functional and 6-31++G** basis set was found to be the most accurate method for simulation of vibrationally resolved X-ray emission spectra of the N_2 molecule in gas phase and this was then applied to study N_2 encapsulated in C_{60}. The sensitivity of the spectra to the presence of the C_{60} cage was demonstrated. The results of the calculations highlighted that the spectra for $N_2@C_{60}$ are dominated by the bands arising from transitions from σ orbitals that are localised on the N_2 molecule to the π^* orbitals that are localised

predominantly on N_2 but also in small percentage on the C_{60} cage. This interaction between N_2 and C_{60} resulted in the shift of two peaks at higher energies for the $0(0) \rightarrow 1(2v0)$ and $0(0) \rightarrow 1(3v0)$ vibronic transitions. The result also showed that the presence of C_{60} cage reduces the difference in the frequency between ground and excited state of N_2 when encapsulated in C_{60}. This could indicate that in the presence of the cage less energy is required for the vibronic transition of N_2. Also, the force constant difference between ground and excited state of encapsulated N_2 was reduced, suggesting that the interaction of two nitrogen atoms when encapsulated in the cage are weaker when compared to the gas phase. However, the calculated spectra for $N_2@C_{60}$ differ slightly from the experimental results. This discrepancy is thought to be due to the harmonic approximation used in the calculations. Including anharmonicity in the calculations could potentially improve the accuracy of the results.

DFT-based techniques were used to examine the sensitivity of X-ray emission spectroscopy (XES) to structure of the peptide bond. The work focused on finding out whether XES can be used to distinguish between different elements of protein secondary structures. The non-resonant X-ray emission spectroscopy of amino acids and a dipeptide was studied using TDDFT calculations at the nitrogen and oxygen K-edges. Comparison with higher level calculations and experimental data showed that TDDFT with the CAM-B3LYP exchange–correlation functional and (Z+1)6-311G* basis set provides an accurate description of the spectra. Calculations for model α-helix and β-sheet structures showed the spectra to be relatively insensitive to the structure of peptide bond, with the greatest variation observed at the oxygen K-edge. Therefore, the sensitivity of the XES spectra to the geometric structure of the peptide bond was confirmed.

Overall, the work in this thesis contributes to a better understanding of the optical and electronic behavior of larger chemical systems and illustrates how

quantum chemical calculations can be used to inform the design of materials for different applications. It also highlights the important role the calculations can play enabling the understanding and interpretation of experimental spectroscopic data by examining the accuracy of DFT-based methods for the simulation of X-ray emission spectra, and vibrationally resolved X-ray absorption spectra of large systems.

Looking ahead, computational molecular spectroscopy has already been shown to play an important role in the prediction and interpretation of spectra of various compounds, as well as in guiding materials development for various applications and pioneering innovations. Constant development of spectroscopic techniques and the search for novel materials with better properties will provide new challenges for simulation, especially for bigger and more complex compounds. The findings in this work serve as good foundation for the further development of both spectroscopic methods and new materials. The extension of the work is to try to push the capabilities of computational molecular spectroscopy to include bigger systems and, in the case of vibrationally resolved X-ray absorption spectroscopy, to include the anharmonic approximation in the calculations to accurately simulate the spectra. The search is therefore towards methods development that will enable the scientific community to support the prediction and interpretation of the spectra and lead new materials discoveries without significant increase in computational cost.

References

1. Barone, V. *et al.* Computational molecular spectroscopy. *Nature Reviews Methods Primers* **1,** 2662–8449 (2021).

2. Shen, S., Appendino, G. & Guo, Y. Pitfalls in the structural elucidation of small molecules. A critical analysis of a decade of structural misassignments of marine natural products. *Natural Product Reports* **39,** 1803–1832 (2022).

3. J., H., Bousquet, B., Canioni, L. & Mounaix, P. Review in terahertz spectral analysis. *TrAC Trends in Analytical Chemistry* **44,** 98–105 (2013).

4. Mino, L. *et al.* in *Characterization of Nanoparticles* (eds Hodoroaba, V.-D., Unger, W. E. & Shard, A. G.) 457–480 (Elsevier, 2020).

5. Van Eerdenbrugh, B. & Taylor, L. S. Application of mid-IR spectroscopy for the characterization of pharmaceutical systems. *International Journal of Pharmaceutics* **417,** 3–16 (2011).

6. Wang, F. Use of simulated infrared spectra to test N2-Ar pair potentials and dipole moment surfaces. *Molecular Physics* **88,** 821–840 (1996).

7. Wang, F., McCourt, F. R. W. & Le Roy, R. J. Dipole moment surfaces and the mid- and far-IR spectra of N2-Ar. *The Journal of Chemical Physics* **113,** 98–106 (2000).

8. Ng, L. M. & Simmons, R. Infrared Spectroscopy. *Analytical Chemistry* **71,** 343–350 (1999).

9. Verma, G. & Mishra, M. Development and optimization of UV-Vis spectroscopy-a review. *World Journal of Pharmaceutical Research* **7,** 1170–1180 (2018).

10. Myneni, S. C. Soft X-ray spectroscopy and spectromicroscopy studies of organic molecules in the environment. *Reviews in Mineralogy and Geochemistry* **49,** 485–579 (2002).

11. Bokarev, S. I. & Kühn, O. Theoretical X-ray spectroscopy of transition metal compounds. *Wiley Interdisciplinary Reviews: Computational Molecular Science* **10,** e1433 (2020).

12. Carlson, T. A. Photoelectron spectroscopy. *Annual Review of Physical Chemistry* **26,** 211–234 (1975).

13. Fadley, C. S. X-ray photoelectron spectroscopy: Progress and perspectives. *Journal of Electron Spectroscopy and Related Phenomena* **178,** 2–32 (2010).

14. Picollo, M., Aceto, M. & Vitorino, T. UV-Vis spectroscopy. *Physical sciences reviews* **4,** 20180008 (2018).

15. Mumit, M. A. *et al.* DFT studies on vibrational and electronic spectra, HOMO–LUMO, MEP, HOMA, NBO and molecular docking analysis of benzyl-3-N-(2, 4, 5-trimethoxyphenylmethylene) hydrazinecarbodithioate. *Journal of molecular structure* **1220,** 128715 (2020).

16. Schlaf, R., Parkinson, B., Lee, P., Nebesny, K. & Armstrong, N. R. HOMO/LUMO alignment at PTCDA/ZnPc and PTCDA/ClInPc heterointerfaces determined by combined UPS and XPS measurements. *The Journal of Physical Chemistry B* **103,** 2984–2992 (1999).

17. Delesma, F. A. *et al.* A Chemical View on X-ray Photoelectron Spectroscopy: the ESCA Molecule and Surface-to-Bulk XPS Shifts. *ChemPhysChem* **19,** 169–174 (2018).

18. Gupta, V., Ganegoda, H., Engelhard, M. H., Terry, J. & Linford, M. R. Assigning oxidation states to organic compounds via predictions from X-ray photoelectron spectroscopy: a discussion of approaches and recommended improvements. *Journal of Chemical Education* **91,** 232–238 (2014).

19. Abdolkarimi-Mahabadi, M., Bayat, A. & Mohammadi, A. Use of UV-Vis Spectrophotometry for Characterization of Carbon Nanostructures: a Review. *Theoretical and Experimental Chemistry* **57,** 191–198 (2021).

20. Atkins, P. & de Paula J. *Physical Chemistry* (Oxford University Press, Oxford, New York, 2006).

21. Nilsson, A. *et al.* Local probing of the surface chemical bond using X-ray emission spectroscopy. *Applied Physics A* **65,** 147–154 (1997).

22. Norman, P. & Dreuw, A. Simulating X-ray spectroscopies and calculating core-excited states of molecules. *Chemical Reviews* **118,** 7208–7248 (2018).

23. Prince, K. C., Richter, R., de Simone, M., Alagia, M. & Coreno, M. Near Edge X-ray Absorption Spectra of Some Small Polyatomic Molecules. *The Journal of Physical Chemistry A* **107,** 1955–1963 (2003).

24. Henderson, G. S., De Groot, F. M. & Moulton, B. J. X-ray absorption near-edge structure (XANES) spectroscopy. *Reviews in Mineralogy and Geochemistry* **78,** 75–138 (2014).

25. Frenkel, A. I. Applications of extended X-ray absorption fine-structure spectroscopy to studies of bimetallic nanoparticle catalysts. *Chemical Society Reviews* **41,** 8163–8178 (24 2012).

26. Bunker, G. *Introduction to XAFS: a practical guide to X-ray absorption fine structure spectroscopy* (Cambridge University Press, 2010).

27. Sampath, S. *et al.* X-ray diffraction study of nanocrystalline and amorphous structure within major and minor ampullate dragline spider silks. *Soft Matter* **25,** 6713–6722 (2012).

28. Lee, P., Citrin, P., Eisenberger, P. t. & Kincaid, B. Extended X-ray absorption fine structure—its strengths and limitations as a structural tool. *Reviews of Modern Physics* **53,** 769 (1981).

29. Iglesias-Juez, A., Chiarello, G. L., Patience, G. S. & Guerrero-Pérez, M. O. Experimental methods in chemical engineering: X-ray absorption spectroscopy—XAS, XANES, EXAFS. *The Canadian Journal of Chemical Engineering* **100,** 3–22 (2022).

30. Fransson, T. *et al.* X-ray and Electron Spectroscopy of Water. *Chemical Reviews* **116,** 7551–7569 (2016).

31. Nilsson, A. & Pettersson, L. G. M. Chemical bonding on surfaces probed by X-ray emission spectroscopy and density functional theory. *Surface Science Reports* **55,** 49–167 (2004).

32. Triguero, L., Pettersson, L. & Ågren, H. Calculations of X-ray emission spectra of molecules and surface adsorbates by means of density functional theory. *The Journal of Physical Chemistry A* **102,** 10599–10607 (1998).

33. Zhovtobriukh, I., Besley, N. A., Fransson, T., Nilsson, A. & Pettersson, L. G. M. Relationship between X-ray emission and absorption spectroscopy and the local H-bond environment in water. *The Journal of Chemical Physics* **148,** 144507 (2018).

34. Broglie, L. XXXV. A tentative theory of light quanta. *The London, Edinburgh, and Dublin Philosophical Magazine and Journal of Science* **47,** 446–458 (1924).

35. Born, M. Statistical interpretation of quantum mechanics. *Science* **122,** 675–679 (1955).

36. Schrödinger, E. An undulatory theory of the mechanics of atoms and molecules. *Physical Review* **28,** 1049–1070 (1926).

37. Born, M. & Oppenheimer, R. Quantum theory of molecules. *Annalen der Physik* **389,** 457–484 (1927).

38. Hartree, D. R. The Wave Mechanics of an Atom with a Non-Coulomb Central Field. Part I. Theory and Methods. *Mathematical Proceedings of the Cambridge Philosophical Society* **24,** 89–110 (1928).

39. Fock, V. Approximation method for the solution of the quantum mechanical multibody problems. *Zeitschrift fur Physik* **61,** 126–148 (1930).

40. Slater, J. C. A Simplification of the Hartree-Fock Method. *Physical Review* **81,** 385–390 (3 1951).

41. Szabo, A., Szabó, A. & Ostlund, N. *Modern Quantum Chemistry: Introduction to Advanced Electronic Structure Theory* (1982).

42. Roothaan, C. C. J. New Developments in Molecular Orbital Theory. *Reviews of Modern Physics* **23,** 69–89 (2 1951).

43. Hall, G. G. & Lennard-Jones, J. E. The molecular orbital theory of chemical valency VIII. A method of calculating ionization potentials. *Proceedings of the Royal Society of London. Series A. Mathematical and Physical Sciences* **205,** 541–552 (1951).

44. Cramer, C. J. *Essentials of Computational Chemistry: Theories and Models, 2nd Edition* (Wiley, 2004).

45. Binkley, J. S., Pople, J. A. & Hehre, W. J. Self-consistent molecular orbital methods. 21. Small split-valence basis sets for first-row elements. *Journal of the American Chemical Society* **102,** 939–947 (1980).

46. Dunning, T. Gaussian basis sets for use in correlated molecular calculations. I. The atoms boron through neon and hydrogen. *The Journal of Chemical Physics* **90,** 1007–1023 (1989).

47. Martin, J. M. & Sundermann, A. Correlation consistent valence basis sets for use with the Stuttgart–Dresden–Bonn relativistic effective core potentials: The atoms Ga–Kr and In–Xe. *The Journal of Chemical Physics* **114,** 3408–3420 (2001).

48. Hohenberg, P. & Kohn, W. Inhomogeneous Electron Gas. *Physical Review* **136,** B864–B871 (3B 1964).

49. Kohn, W. & Sham, L. J. Self-Consistent Equations Including Exchange and Correlation Effects. *Physical Review* **140,** A1133–A1138 (4A 1965).

50. Negele, J. W. Structure of finite nuclei in the local-density approximation. *Physical review C* **1,** 1260 (1970).

51. Becke, A. D. A new mixing of Hartree–Fock and local density-functional theories. *The Journal of Chemical Physics* **98,** 1372–1377 (1993).

52. Yanai, T., Tew, D. P. & Handy, N. C. A new hybrid exchange-correlation functional using the Coulomb-attenuating method (CAM-B3LYP). *Chemical Physics Letters* **393,** 51–57 (2004).

53. Besley, N. A., Peach, M. J. G. & Tozer, D. J. Time-dependent density functional theory calculations of near-edge X-ray absorption fine structure with short-range corrected functionals. *Physical Chemistry Chemical Physics* **11,** 10350–10358 (44 2009).

54. Besley, N. A. & Asmuruf, F. A. Time-dependent density functional theory calculations of the spectroscopy of core electrons. *Physical Chemistry Chemical Physics* **12,** 12024–12039 (38 2010).

55. Besley, N. & Asmuruf, F. A. Time-dependent density functional theory calculations of the spectroscopy of core electrons. *Physical Chemistry Chemical Physics* (2010).

56. Besley, N. A., Peach, M. J. & Tozer, D. J. Time-dependent density functional theory calculations of near-edge X-ray absorption fine struc-

ture with short-range corrected functionals. *Physical Chemistry Chemical Physics* **11,** 10350–10358 (2009).

57. Runge, E. & Gross, E. K. U. Density-Functional Theory for Time-Dependent Systems. *Physical Review Letters* **52,** 997–1000 (1984).

58. Casida, M. E. in *Recent Advances In Density Functional Methods: (Part I)* 155–192 (World Scientific, 1995).

59. Hirata, S. & Head-Gordon, M. Time-dependent density functional theory within the Tamm-Dancoff approximation. *Chemical Physics Letters* **314,** 291–299 (1999).

60. Gilbert, A. T. B., Besley, N. A. & Gill, P. M. W. Self-consistent field calculations of excited states using the maximum overlap method (MOM). *The Journal of Physical Chemistry A* **112,** 13164–13171 (2008).

61. Wales, D. *Energy Landscapes: Applications to Clusters, Biomolecules and Glasses* (Cambridge University Press, 2004).

62. Franck, J. & Dymond, E. G. Elementary processes of photochemical reactions. *Transactions of the Faraday Society* **21,** 536–542 (1926).

63. Coolidge, A. S., James, H. M. & Present, R. D. A Study of the Franck-Condon Principle. *The Journal of Chemical Physics* **4,** 193–211 (2004).

64. Bray, F., Jemal, A., Grey, N., Ferlay, J. & Forman, D. Global cancer transitions according to the Human Development Index (2008–2030): a population-based study. *The Lancet Oncology* **13,** 790–801 (2012).

65. Winter, J. M., Yeo, C. J. & Brody, J. R. Diagnostic, prognostic, and predictive biomarkers in pancreatic cancer. *Journal of Surgical Oncology* **107,** 15–22 (2013).

66. Estrela, P., Damborský, P., Švitel, J. & Katrlík, J. Optical biosensors. *Essays in Biochemistry* **60,** 91–100 (2016).

67. Yoon, J., Shin, M., Lee, T. & Choi, J.-W. Highly Sensitive Biosensors Based on Biomolecules and Functional Nanomaterials Depending on the Types of Nanomaterials: A Perspective Review. *Materials* **13** (2020).

68. Chen, C. & Wang, J. Optical biosensors: an exhaustive and comprehensive review. *Analyst* **145,** 1605–1628 (5 2020).

69. Ulrich, G., Ziessel, R. & Harriman, A. The Chemistry of Fluorescent Bodipy Dyes: Versatility Unsurpassed. *Angewandte Chemie International Edition* **47,** 1184–1201.

70. Boens, N., Leen, V. & Dehaen, W. Fluorescent indicators based on BODIPY. *Chemical Society Reviews* **41,** 1130–1172 (3 2012).

71. Bruchez, M., Moronne, M., Gin, P., Weiss, S. & Alivisatos, A. P. Semiconductor Nanocrystals as Fluorescent Biological Labels. *Science* **281,** 2013–2016 (1998).

72. Michalet, X. *et al.* Quantum Dots for Live Cells, in Vivo Imaging, and Diagnostics. *Science* **307,** 538–544 (2005).

73. Wolfbeis, O. S. An overview of nanoparticles commonly used in fluorescent bioimaging. *Chemical Society Reviews* **44,** 4743–4768 (14 2015).

74. Chalfie, M., Tu, Y., Euskirchen, G., Ward, W. W. & Prasher, D. C. Green Fluorescent Protein as a Marker for Gene Expression. *Science* **263,** 802–805 (1994).

75. Tsien, R. Y. The Green Fluorescence Protein. *Annual Review of Biochemistry* **67,** 509–544 (1998).

76. Resch-Genger, U., Grabolle, M., Cavaliere-Jaricot, S., Nitschke, R. & Nann, T. Quantum dots versus organic dyes as fluorescent labels. *Nature Methods* **5,** 763–775 (2008).

77. Frecker, T., Bailey, D., Arzeta-Ferrer, X., McBride, J. & Rosenthal, S. J. Review—Quantum Dots and Their Application in Lighting, Displays, and Biology. *ECS Journal of Solid State Science and Technology* **5,** R3019–R3031 (2015).

78. Brus, L. E. Electron–electron and electron-hole interactions in small semiconductor crystallites: The size dependence of the lowest excited electronic state. *The Journal of Chemical Physics* **80,** 4403–4409 (1984).

79. Burda, C., Chen, X., Narayanan, R. & El-Sayed, M. A. Chemistry and Properties of Nanocrystals of Different Shapes. *Chemical Reviews* **105,** 1025–1102 (2005).

80. Zhou, J., Liu, Y., Tang, J. & Tang, W. Surface ligands engineering of semiconductor quantum dots for chemosensory and biological applications. *Materials Today* **20,** 360–376 (2017).

81. Zhang, F., Ali, Z., Amin, F., Riedinger, A. & Parak, W. J. In vitro and intracellular sensing by using the photoluminescence of quantum dots. *Analytical and bioanalytical chemistry* **397,** 935–942 (2010).

82. Abha, K. *et al.* Photoluminescence sensing of bilirubin in human serum using l-cysteine tailored manganese doped zinc sulphide quantum dots. *Sensors and Actuators B: Chemical* **282,** 300–308 (2019).

83. Tajarrod, N., Rofouei, M. K., Masteri-Farahani, M. & Zadmard, R. A quantum dot-based fluorescence sensor for sensitive and enzymeless detection of creatinine. *Analytical Methods* (2016).

84. Zhang, W.-H., Ma, W. & Long, Y.-T. Redox-Mediated Indirect Fluorescence Immunoassay for the Detection of Disease Biomarkers Using Dopamine-Functionalized Quantum Dots. *Analytical Chemistry* **88,** 5131–5136 (2016).

85. Zhu, H., Yang, Y., Wu, K. & Lian, T. Charge Transfer Dynamics from Photoexcited Semiconductor Quantum Dots. *Annual Review of Physical Chemistry* **67,** 259–281 (2016).

86. Ren, J. *et al.* Influence of surface chemistry on optical, chemical and electronic properties of blue luminescent carbon dots. *Nanoscale* **11,** 2056–2064 (4 2019).

87. Hines, D. A. & Kamat, P. V. Recent Advances in Quantum Dot Surface Chemistry. *ACS Applied Materials & Interfaces* **6,** 3041–3057 (2014).

88. Hildebrandt, N. *et al.* Energy Transfer with Semiconductor Quantum Dot Bioconjugates: A Versatile Platform for Biosensing, Energy Harvesting, and Other Developing Applications. *Chemical Reviews* **117,** 536–711 (2017).

89. Chern, M., Kays, J. C., Bhuckory, S. & Dennis, A. M. Sensing with photoluminescent semiconductor quantum dots. *Methods and Applications in Fluorescence* **7,** 012005 (2019).

90. Van Bay, M. *et al.* Using calculations of the electronically excited states for investigation of fluorescent sensors: A review. *Vietnam Journal of Chemistry* **57,** 389–400.

91. Li, G.-Y. & Han, K.-L. The sensing mechanism studies of the fluorescent probes with electronically excited state calculations. *WIREs Computational Molecular Science* **8,** e1351.

92. Lehtonen, O., Sundholm, D. & Vänskä, T. Computational studies of semiconductor quantum dots. *Physical Chemistry Chemical Physics* **10,** 4535–4550 (31 2008).

93. Anas, M. M.-'. & Gopir, G. Electronic and Optical Properties of Small Hydrogenated Silicon Quantum Dots Using Time-Dependent Density Functional Theory. *Journal of Nanomaterials,* 9 (2008).

94. Feng, J. *et al.* Tuning the electronic and optical properties of graphene quantum dots by selective boronization. *Journal of Materials Chemistry C* **7,** 237–246 (2 2019).

95. Chen, S., Ullah, N., Wang, T. & Zhang, R. Tuning the optical properties of graphene quantum dots by selective oxidation: a theoretical perspective. *Journal of Materials Chemistry C* **6,** 6875–6883 (25 2018).

96. Zhao, M., Yang, F., Xue, Y., Xiao, D. & Guo, Y. A Time-Dependent DFT Study of the Absorption and Fluorescence Properties of Graphene Quantum Dots. *ChemPhysChem* **15,** 950–957.

97. Tamukong, P. K., Peiris, W. D. N. & Kilina, S. Computational insights into CdSe quantum dots' interactions with acetate ligands. *Physical Chemistry Chemical Physics* **18,** 20499–20510 (30 2016).

98. Chopra, S. & Rai, B. DFT/TDDFT study of electronic and optical properties of Surface-passivated Silicon nanocrystals, Sin (n = 20, 24, 26 and 28. *Journal of Nanostructure in Chemistry* **5,** 203 (2 2015).

99. Chen, X. *et al.* Fluorophore-Labeled S-Nitrosothiols. *The Journal of Organic Chemistry* **66,** 6064–6073 (2001).

100. Carano, M. *et al.* Synthesis of Heteroleptic Anthryl-Substituted β-Ketoenolates of Rhodium(III) and Iridium(III): Photophysical, Electrochemical, and EPR Study of the Fluorophore-Metal Interaction. *Inorganic Chemistry* **41,** 3396–3409 (2002).

101. Franzen, S., Ni, W. & Wang, B. Study of the Mechanism of Electron-Transfer Quenching by Boron-Nitrogen Adducts in Fluorescent Sensors. *The Journal of Physical Chemistry B* **107,** 12942–12948 (2003).

102. Salman, H. *et al.* Sensitive and Selective PET-Based Diimidazole Luminophore for ZnII Ions: A Structure-Activity Correlation. *Inorganic Chemistry* **45,** 5315–5320 (2006).

103. Bañuelos, J. *et al.* Photophysical Study of New Versatile Multichromophoric Diads and Triads with BODIPY and Polyphenylene Groups. *The Journal of Physical Chemistry A* **112,** 10816–10822 (2008).

104. Lu, H. *et al.* Experimentation and Theoretic Calculation of a BODIPY Sensor Based on Photoinduced Electron Transfer for Ions Detection. *The Journal of Physical Chemistry A* **113,** 14081–14086 (2009).

105. Briggs, E. A. & Besley, N. A. Density Functional Theory Based Analysis of Photoinduced Electron Transfer in a Triazacryptand Based K+ Sensor. *The Journal of Physical Chemistry A* **119,** 2902–2907 (2015).

106. Li, G.-Y., Zhao, G.-J., Liu, Y.-H., Han, K.-L. & He, G.-Z. TD-DFT study on the sensing mechanism of a fluorescent chemosensor for fluoride: Excited-state proton transfer. *Journal of Computational Chemistry* **31,** 1759–1765.

107. Basheer, S. M. & Sreekanth, A. TD-DFT study on the fluoride and copper ion sensing mechanism of pyrene N(4) phenyl thiosemicarbazone. *Computational and Theoretical Chemistry* **1085,** 31–39 (2016).

108. Spectroscopic and TD-DFT studies on the turn-off fluorescent chemosensor based on anthraldehyde N(4) cyclohexyl thiosemicarbazone for the selective recognition of fluoride and copper ions. *Polyhedron* **109,** 7–18 (2016).

109. Sun, M., Guo, J., Yang, Q., Xiao, N. & Li, Y. A new fluorescent and colorimetric sensor for hydrazine and its application in biological systems. *Journal of Materials Chemistry B* **2,** 1846–1851 (13 2014).

110. Jiao, L. *et al.* Unusual spectroscopic and photophysical properties of meso-tert-butylBODIPY in comparison to related alkylated BODIPY dyes. *RSC Advances* **5,** 89375–89388 (109 2015).

111. Sun, X.-F. *et al.* DFT/TD-DFT calculations on the sensing mechanism of a dual response near-infrared fluorescent chemosensor for superoxide anion and hydrogen polysulfides: photoinduced electron transfer. *RSC Advances* **6,** 104735–104741 (106 2016).

112. Berrones-Reyes, J. C. *et al.* Quantum chemical elucidation of the turn-on luminescence mechanism in two new Schiff bases as selective chemosensors of Zn^{2+}: synthesis, theory and bioimaging applications. *RSC Advances* **9,** 30778–30789 (53 2019).

113. Treto-Suárez, M. A. *et al.* New Sensitive and Selective Chemical Sensors for Ni^{2+} and Cu^{2+} Ions: Insights into the Sensing Mechanism through DFT Methods. *The Journal of Physical Chemistry A* **124,** 6493–6503 (2020).

114. Narsaria, A. K. *et al.* Performance of TDDFT Vertical Excitation Energies of Core-Substituted Naphthalene Diimides. *Journal of Computational Chemistry* **41,** 1448–1455 (2020).

115. Jain, K. *et al.* Density functional investigation and some optical experiments on dye-sensitized quantum dots. *Physical Chemistry Chemical Physics* **17,** 28683–28696 (43 2015).

116. Kilina, S., Cui, P., Fischer, S. A. & Tretiak, S. Conditions for Directional Charge Transfer in CdSe Quantum Dots Functionalized by Ru(II) Polypyridine Complexes. *The Journal of Physical Chemistry Letters* **5,** 3565–3576 (2014).

117. Del Ben, M., Havenith, R. W. A., Broer, R. & Stener, M. Density Functional Study on the Morphology and Photoabsorption of CdSe Nanoclusters. *The Journal of Physical Chemistry C* **115,** 16782–16796 (2011).

118. Inerbaev, T. M. *et al.* Quantum chemistry of quantum dots: Effects of ligands and oxidation. *The Journal of Chemical Physics* **131,** 044106 (2009).

119. Karttunen, A. J., Linnolahti, M. & Pakkanen, T. A. Structural and Electronic Characteristics of Diamondoid Analogues of Group 14 Elements. *The Journal of Physical Chemistry C* **112,** 16324–16330 (2008).

120. Shao, Y. *et al.* Advances in molecular quantum chemistry contained in the Q-Chem 4 program package. *Molecular Physics* **113,** 184–215 (2015).

121. Kocevski, V., Eriksson, O. & Rusz, J. Size dependence of the stability, electronic structure, and optical properties of silicon nanocrystals with various surface impurities. *Physical Review B* **91,** 125402 (12 2015).

122. Zhao, L.-Z. *et al.* Theoretical Prediction of Si2–Si33 Absorption Spectra. *The Journal of Physical Chemistry A* **121,** 6388–6397 (2017).

123. Ronchi, C., Soria, F. A., Ferraro, L., Botti, S. & Di Valentin, C. Absorption mechanism of dopamine/DOPAC-modified TiO2 nanoparticles by time-dependent density functional theory calculations. *Materials Today Energy* **19,** 100571 (2021).

124. Wang, Z. *et al.* Detection of IL-8 in human serum using surface-enhanced Raman scattering coupled with highly-branched gold nanoparticles and gold nanocages. *New Journal of Chemistry* **43,** 1733–1742 (4 2019).

125. Baskoutas, S. & Terzis, A. F. Size-dependent band gap of colloidal quantum dots. *Journal of Applied Physics* **99,** 013708 (2006).

126. Beriso, A. Determination of Size-Dependent Energy Bandgap of Germanium (Ge) nanostructure. *Advances in Physics Theories and Applications* (2019).

127. Dong, H., Hou, T., Sun, X., Li, Y. & Lee, S.-T. The structures and properties of Si/SiO2 core/shell quantum dots studied by density-functional tight-binding calculations. *Applied Physics Letters* **103,** 123115 (2013).

128. Garoufalis, C. S., Zdetsis, A. D. & Grimme, S. High Level Ab Initio Calculations of the Optical Gap of Small Silicon Quantum Dots. *Physical Review Letters* **87,** 276402 (27 2001).

129. Takai, K., Ikeda, M., Yamasaki, T. & Kaneta, C. Size and temperature dependence of the energy gaps in Si, SiC and C quantum dots based on tight-binding molecular dynamics simulations. *Journal of Physics Communications* **1,** 045010 (2017).

130. Shechtman, D., Blech, I., Gratias, D. & Cahn, J. W. Metallic Phase with Long-Range Orientational Order and No Translational Symmetry. *Physical Review Letters* **53,** 1951–1953 (20 1984).

131. Zhao, Y., Kim, Y.-H., Du, M.-H. & Zhang, S. B. First-Principles Prediction of Icosahedral Quantum Dots for Tetravalent Semiconductors. *Physical Review Letters* **93,** 015502 (1 2004).

132. Zhou, G., Lu, G. & Prezhdo, O. V. Modeling Auger Processes with Nonadiabatic Molecular Dynamics. *Nano Letters* **21,** 756–761 (2021).

133. Fossé, I., Lal, S., Hossaini, A. N., Infante, I. & Houtepen, A. J. Effect of Ligands and Solvents on the Stability of Electron Charged CdSe Colloidal Quantum Dots. *The Journal of Physical Chemistry C* **125,** 23968–23975 (2021).

134. Liu, H. *et al.* A hybrid quantum-classical model of electrostatics in multiply charged quantum dots. *The Journal of Physical Chemistry C* **121,** 26086–26095 (2017).

135. Kroto, H., Heath, J., Brien, S., Curl, R. & Smalley, E. C_{60}: Buckminsterfullerene. *Nature* **318,** 162–163 (1985).

136. Hebard, A. *et al.* Superconductivity at 18 K in potassium-doped C_{60}. *Nature* **350,** 600–601 (1991).

137. Bethune, D. S., Johnson, R. D., Salem, J. R., de Vries, M. S. & Yannoni, C. S. Atoms in carbon cages: the structure and properties of endohedral fullerenes. *Nature* **366,** 123–128 (1993).

138. Li, J. L. & Yang, G. W. Iron Endohedral-Doped Boron Fullerene: A Potential Single Molecular Device with Tunable Electronic and Magnetic Properties. *The Journal of Physical Chemistry C* **113,** 18292–18295 (2009).

139. Burlingame, Q. *et al.* Centimetre-scale electron diffusion in photoactive organic heterostructures. *Nature* **554,** 77–80 (2018).

140. Ju, C., Suter, D. & Du, J. An endohedral fullerene-based nuclear spin quantum computer. *Physics Letters A* **375,** 1441–1444 (2011).

141. Shetti, N. P., Mishra, A., Basu, S. & Aminabhavi, T. M. Versatile fullerenes as sensor materials. *Materials Today Chemistry* **20,** 100454 (2021).

142. R, B., Vallant, R. & Najam-ul-Haq, M. Medicinal applications of fullerenes. *International Journal of Nanomedicine* (2007).

143. Feng, M., Zhao, J. & Petek, H. Atom-like, Hollow-Core-Bound Molecular Orbitals of C_{60}. *Science* **320,** 359–362 (2008).

144. Zhao, J., Feng, M., Yang, J. & Petek, H. The Superatom States of Fullerenes and Their Hybridization into the Nearly Free Electron Bands of Fullerites. *ACS Nano* **3,** 853–864 (2009).

145. Dutton, G., Dougherty, D., Jin, W., Reutt-Robey, J. & Robey, S. Superatom Orbitals of C_{60} on Ag(111): Two Photon Photoemission and Scanning Tunneling Spectroscopy. *Physical Review B* (2011).

146. Shibuta, M., Yamamoto, K., Guo, H., Zhao, J. & Nakajima, A. Highly Dispersive Nearly Free Electron Bands at a 2D-Assembled C_{60} Monolayer. *The Journal of Physical Chemistry C* **124,** 734–741 (2020).

147. Kuklin, A. V., Suresh, R., Shimizu, K., Yamada, Y. & Ågren, H. Superatom Molecular Orbitals of Li@C_{60}: Effects of the Li Position and the Substrate. *The Journal of Physical Chemistry C* **126,** 15891–15898 (2022).

148. Boyle, M. *et al.* Excitation of Rydberg Series in C_{60}. *Physical Review Letters* **87,** 273401 (27 2001).

149. Ibrahim, M., El-Haes, H. b. & Jalbout, A. F. Semiempirical molecular modelling study of C_{60} doped with silicon, germanium, and aluminium. *Chinese Journal of Physics* **44,** 432–439 (2006).

150. Raghavachari, K. & Sosa, C. Fullerene derivatives. Comparative theoretical study of C_{60} and $C_{60}CH_2$. *Chemical Physics Letters* **209,** 223–228 (1993).

151. Misra, N., Dwivedi, A. & Pandey, A. Geometrical electronic, and vibrational properties of fullerene rings doped with transition metals. *Chinese Journal of Physics* **50,** 64–72 (2012).

152. Suzuki, S. *et al.* Formation and stability of small metallocarbon clusters: what is the specificity for the formation of stable metallofullerenes? *International Journal of Mass Spectrometry and Ion Processes* **138,** 297–306 (1994).

153. Lu, J., Zhou, Y., Zhang, S., Zhang, X. & Zhao, X. Structural and electronic properties of endohedral and exohedral complexes of silicon with C_{60}. *Chemical Physics Letters* **343,** 39–43 (2002).

154. Esrafili, M. D. & Sadeghi, S. A DFT investigation into the possibility of using noble gas encapsulated fullerenes for Li storage. *Chemical Physics Letters* **787,** 139236 (2022).

155. He, T., Gao, G., Kou, L., Will, G. & Du, A. Endohedral metallofullerenes (M@C_{60}) as efficient catalysts for highly active hydrogen evolution reaction. *Journal of Catalysis* **354,** 231–235 (2017).

156. Raggi, G., Stace, A. J. & Bichoutskaia, E. Polarisation charge switching through the motion of metal atoms trapped in fullerene cages. *Physical Chemistry Chemical Physics* **16,** 23869–23873 (43 2014).

157. Bernshtein, V. & Oref, I. Surface migrations of endohedral Li on the inner wall of C_{60}. *Physical Review A* **62,** 033201 (2000).

158. Varganov, S., Avramov, P. & Ovchinnikov, S. Ab initio calculations of endo-and exohedral C_{60} fullerene complexes with Li^+ ion and the endohedral C_{60} fullerene complex with Li_2 dimer. *Physics of the Solid State* **42,** 388–392 (2000).

159. Slanina, Z., Uhlík, F., Lee, S.-L., Adamowicz, L. & Nagase, S. MPWB1K calculations of stepwise encapsulations: Lix@C_{60}. *Chemical Physics Letters* **463,** 121–123 (2008).

160. Cioslowski, J. & Fleischmann, E. D. Endohedral complexes: Atoms and ions inside the C_{60} cage. *The Journal of Chemical Physics* **94,** 3730–3734 (1991).

161. Cioslowski, J. & Nanayakkara, A. Endohedral fullerites: A new class of ferroelectric materials. *Physical Review Letters,* 2871–2873 (1992).

162. Cioslowski, J. & Lin, Q. Guest discrimination in complexes of alkali metal cations with the $C_{36}H_{36}$ spheriphane: an ab initio electronic structure study. *Journal of the American Chemical Society* **117,** 2553–2556 (1995).

163. Murry, R. L. & Scuseria, G. E. Theoretical Evidence for a C_{60} "Window" Mechanism. *Science* **263,** 791–793 (1994).

164. Darzynkiewicz, R. B. & Scuseria, G. E. Noble Gas Endohedral Complexes of C_{60} Buckminsterfullerene. *The Journal of Physical Chemistry A* **101,** 7141–7144 (1997).

165. Buehl, M. *et al.* Helium and lithium NMR chemical shifts of endohedral fullerene compounds: An ab initio study. *Journal of the American Chemical Society* **116,** 6005–6006 (1994).

166. Bühl, M. & Thiel, W. Ab initio helium NMR chemical shifts of endohedral fullerene compounds He@C_n n = 32to180. *Chemical Physics Letters* **233,** 585–589 (1995).

167. Patchkovskii, S. & Thiel, W. How Does Helium Get into Buckminsterfullerene? *Journal of the American Chemical Society* **118,** 7164–7172 (1996).

168. Patchkovski, S. & Thiel, W. C_{60} dimers A Route to Endohedral Fullerene Compounds? *Journal of the Americal Chemical Society* **3,** 556–563 (1998).

169. Pavlyukh, Y. & Berakdar, J. Communication: Superatom molecular orbitals: New types of long-lived electronic states. *The Journal of Chemical Physics* **135,** 201103 (2011).

170. Johansson, J. O., Henderson, G. G., Remacle, F. & Campbell, E. E. B. Angular-resolved Photoelectron Spectroscopy of Superatom Orbitals of Fullerenes. *Physical Review Letters* **108** (2012).

171. Johansson, O., Bohl, E. & Campbell, E. E. Super-atom molecular orbital excited states of fullerenes. *Philosophical Transactions of the Royal Society A* (2016).

172. Mignolet, B., Johansson, J. O., Campbell, E. E. B. & Remacle, F. Probing Rapidly-Ionizing Super-Atom Molecular Orbitals in C_{60}: A Computational and Femtosecond Photoelectron Spectroscopy Study. *ChemPhysChem* **14,** 3332–3340 (2013).

173. Li, J. *et al.* Au_{20}: a tetrahedral cluster. *Science* **299,** 864–867 (2003).

174. Wang, X.-B., Ding, C.-F. & Wang, L.-S. High resolution photoelectron spectroscopy of C_{60}. *The Journal of chemical physics* **110,** 8217–8220 (1999).

175. Takahashi, T. *et al.* Pseudo-gap at the Fermi level in K_3C_{60} observed by photoemission and inverse photoemission. *Physical Review Letters* **68,** 1232–1235 (8 1992).

176. Benning, P. J., Martins, J. L., Weaver, J. H., Chibante, L. P. F. & Smalley, R. E. Electronic States of K_xC_{60}: Insulating, Metallic, and Superconducting Character. *Science* **252,** 1417–1419 (1991).

177. Lof, R. W., van Veenendaal, M. A., Koopmans, B., Jonkman, H. T. & Sawatzky, G. A. Band gap, excitons, and Coulomb interaction in solid C_{60}. *Physical Review Letters* **68,** 3924–3927 (26 1992).

178. Wang, H., He, Y., Li, Y. & Su, H. Photophysical and Electronic Properties of Five PCBM-like C_{60} Derivatives: Spectral and Quantum Chemical View. *The Journal of Physical Chemistry A* **116,** 255–262 (2012).

179. Spataru, C. D., Ismail-Beigi, S., Benedict, L. X. & Louie, S. G. Excitonic Effects and Optical Spectra of Single-Walled Carbon Nanotubes. *Physical Review Letters* **92,** 077402 (7 2004).

180. Shu, Y. & Truhlar, D. G. Relationships between Orbital Energies, Optical and Fundamental Gaps, and Exciton Shifts in Approximate Density Functional Theory and Quasiparticle Theory. *Journal of Chemical Theory and Computation* **16,** 4337–4350 (2020).

181. Foster, M. E., Sohlberg, K., Allendorf, M. D. & Talin, A. A. Unraveling the Semiconducting/Metallic Discrepancy in Ni3(HITP)2. *The Journal of Physical Chemistry Letters* **9,** 481–486 (2018).

182. Teale, A. M. *et al.* DFT exchange: sharing perspectives on the workhorse of quantum chemistry and materials science. *Physical chemistry chemical physics* **24,** 28700–28781 (2022).

183. Chandler, H. J., Stefanou, M., Campbell, E. & Schaub, R. $Li@C_{60}$ as a multi-state molecular switch. *Nature Communications* **10,** 2283 (2019).

184. Copley, J., Neumann, D., Cappelletti, R. & Kamitakahara, W. Neutron scattering studies of C_{60} and its compounds. *Journal of Physics and Chemistry of Solids* **53,** 1353–1371 (1992).

185. Silien, C., Pradhan, N. A., Ho, W. & Thiry, P. A. Influence of adsorbate-substrate interaction on the local electronic structure of C_{60} studied by low-temperature STM. *Physical Review B* **69,** 115434 (11 2004).

186. Lu, X., Grobis, M., Khoo, K. H., Louie, S. G. & Crommie, M. F. Charge transfer and screening in individual C_{60} molecules on metal substrates: A scanning tunneling spectroscopy and theoretical study. *Physical Review B* **70,** 115418 (11 2004).

187. Lu, X., Grobis, M., Khoo, K. H., Louie, S. & Crommie, M. Spatially Mapping the Spectral Density of a Single C_{60} Molecule. *Physical Review Letters* **90,** 096802 (9 2003).

188. Johansson, J. O. & Campbell, E. E. B. Probing excited electronic states and ionisation mechanisms of fullerenes. *Chemical Society Reviews* **42,** 5661–5671 (13 2013).

189. Xiong, H. *et al.* The Role of Super-Atom Molecular Orbitals in Doped Fullerenes in a Femtosecond Intense Laser Field. *Scientific Reports* **7** (2017).

190. Murphy, A. *et al.* Observation of Atomlike Nitrogen in Nitrogen-Implanted Solid C_{60}. *Physical Review Letters* **77,** 1075–1078 (1996).

191. Knapp, C. *et al.* Electron paramagnetic resonance study of atomic phosphorus encapsulated in [60]fullerene. *Molecular Physics* **95,** 999–1004 (1998).

192. Rüttimann, M. *et al.* π-Electron Ring-Current Effects in Multiple Adducts of $^3He@C_{60}$ and $^3He@C_{70}$: A ^3He NMR Study. *Chemistry A European Journal* **3,** 1071–1076 (1997).

193. Saunders, M. *et al.* Incorporation of helium, neon, argon, krypton, and xenon into fullerenes using high pressure. *Journal of the American Chemical Society* **116,** 2193–2194 (1994).

194. Takeda, A. *et al.* Superconductivity of doped Ar@C_{60}. *Chemical Communications,* 912–914 (8 2006).

195. Yamamoto, K. *et al.* Isolation and Spectral Properties of Kr@C_{60}, a Stable van der Waals Molecule. *Journal of the American Chemical Society* **121,** 1591–1596 (1999).

196. Saunders, M., Jimenez, H. & Vazquez, R. Stable compounds of helium and neon: He@C_{60} and Ne@C_{60}. *Science* **259,** 1428–1430 (1993).

197. Saunders, M., Cross, R., Jimenez-Vazquez, H., Shimshi, R. & Khong, A. Noble Gas Atoms Inside Fullerenes. *Science* **271,** 1693 (1996).

198. Syamala, M. S., Cross, R. J. & Saunders, M. ^{129}Xe NMR Spectrum of Xenon Inside C_{60}. *Journal of the American Chemical Society* **124,** 6216–6219 (2002).

199. Cioslowski, J. & Raghavachari, K. Electrostatic potential, polarization, shielding, and charge transfer in endohedral complexes of the C_{60}, C_{70}, C_{76}, C_{78}, C_{82}, and C_{84} clusters. *The Journal of Chemical Physics* **98,** 8734–8741 (1993).

200. Pang, L. & Brisse, F. Endohedral energies and translation of fullerene-noble gas clusters G@C_n (G= helium, neon, argon, krypton and xenon; n= 60 and 70). *The Journal of Physical Chemistry* **97,** 8562–8563 (1993).

201. Shimshi, R., Khong, A., Jiménez-Vázquez, H., Cross, R. & Saunders, M. Release of noble gas atoms from inside fullerenes. *Tetrahedron* **52,** 5143–5148 (1996).

202. Sanville, E. & BelBruno, J. J. Computational Studies of Possible Transition Structures in the Insertion and Windowing Mechanisms for the

Formation of Endohedral Fullerenes. *The Journal of Physical Chemistry B* **107,** 8884–8889 (2003).

203. Bug, A. L., Wilson, A. & Voth, G. A. Nonlinear vibrational dynamics of a neon atom in fullerene (C_{60}). *The Journal of Physical Chemistry* **96,** 7864–7869 (1992).

204. Civiš, S. *et al.* Vibrational spectra of La@C_{60} and Ce@C_{60} endohedral fullerenes: Influence of spin state multiplicity. *Spectrochimica Acta Part A: Molecular and Biomolecular Spectroscopy* **254,** 119593 (2021).

205. Kempgens, B. *et al.* Vibrational excitation in C 1s and O 1s photoionization of CO. *Journal of Physics B: Atomic, Molecular and Optical Physics* **30,** L741 (1997).

206. Prince, K. C., Avaldi, L., Coreno, M., Camilloni, R. & de Simone, M. Vibrational structure of core to Rydberg state excitations of carbon dioxide and dinitrogen oxide. *Journal of Physics B: Atomic, Molecular and Optical Physics* **32,** 2551 (1999).

207. De Simone, M., Coreno, M., Alagia, M., Richter, R. & Prince, K. C. Inner shell excitation spectroscopy of the tetrahedral molecules CX_4 (X = H,F,Cl). *Journal of Physics B: Atomic, Molecular and Optical Physics* **35,** 61 (2001).

208. Hergenhahn, U. Vibrational structure in inner shell photoionization of molecules. *Journal of Physics B: Atomic, Molecular and Optical Physics* **37,** R89 (2004).

209. Ehara, M. & Ueda, K. Vibrational spectra and geometry relaxation in core-electronic processes of N_2O and CO_2. *Journal of Physics: Conference Series* **235,** 012020 (2010).

210. Ehara, M. *et al.* Theoretical spectroscopy of O 1s and N 1s excited states of N_2O. *Journal of Physics: Conference Series* **288,** 012024 (2011).

211. Trofimov, A., Moskovskaya, T., Gromov, E., Vitkovskaya, N. & Schirmer, J. Core-level electronic spectra in ADC(2) approximation for polarization propagator: Carbon monoxide and nitrogen molecules. *Journal of Structural Chemistry* **41,** 1573–8779 (2000).

212. Besley, N. A. Fast Time-Dependent Density Functional Theory Calculations of the X-ray Absorption Spectroscopy of Large Systems. *Journal of Chemical Theory and Computation* **12,** 5018–5025 (2016).

213. Besley, N. Modeling of the spectroscopy of core electrons with density functional theory. *WIREs Computational Molecular Science* **11,** e1527 (2021).

214. Konecny, L., Komorovsky, S., Vicha, J., Ruud, K. & Repisky, M. Exact Two-Component TDDFT with Simple Two-Electron Picture-Change Corrections: X-ray Absorption Spectra Near L- and M-Edges of Four-Component Quality at Two-Component Cost. *The Journal of Physical Chemistry A* **127,** 1360–1376 (2023).

215. Gozem, S. & Krylov, A. I. The ezSpectra suite: An easy-to-use toolkit for spectroscopy modeling. *WIREs Computational Molecular Science* **12,** e1546 (2022).

216. Wenzel, J., Wormit, M. & Dreuw, A. Calculating core-level excitations and X-ray absorption spectra of medium-sized closed-shell molecules with the algebraic-diagrammatic construction scheme for the polarization propagator. *Journal of Computational Chemistry* **35,** 1900–1915 (2014).

217. Fatehi, S., Schwartz, C. P., Saykally, R. J. & Prendergast, D. Nuclear quantum effects in the structure and lineshapes of the N_2 near-edge X-ray absorption fine structure spectrum. *The Journal of Chemical Physics* **132,** 094302 (2010).

218. Plekan, O. *et al.* An X-ray absorption study of glycine, methionine and proline. *Journal of Electron Spectroscopy and Related Phenomena* **155,** 47–53 (2007).

219. Coriani, S., Fransson, T., Christiansen, O. & Norman, P. Asymmetric-Lanczos-Chain-Driven Implementation of Electronic Resonance Convergent Coupled-Cluster Linear Response Theory. *Journal of Chemical Theory and Computation* **8,** 1616–1628 (2012).

220. He, L. *et al. Specific versus non-specific solvent interactions of a biomolecule in water* 2022. arXiv: 2205.08217 [physics.chem-ph].

221. Kelly, S. M., Jess, T. J. & Price, N. C. How to study proteins by circular dichroism. *BBA - Proteins and Proteomics* **1751,** 119–139 (2005).

222. Buck, M., Radford, S. E. & Dobson, C. M. A partially folded state of hen egg white lysozyme in trifluoroethanol: structural characterization and implications for protein folding. *Biochemistry* **32,** 669–678 (1993).

223. Nielsen, L. *et al.* Effect of Environmental Factors on the Kinetics of Insulin Fibril Formation: Elucidation of the Molecular Mechanism. *Biochemistry* **40,** 6036–6046 (2001).

224. Kaznacheyev, K. *et al.* Innershell Absorption Spectroscopy of Amino Acids. *The Journal of Physical Chemistry A* **106,** 3153–3168 (2002).

225. Gordon, M. L. *et al.* Inner-shell excitation spectroscopy of the peptide bond: Comparison of the C 1s, N 1s, and O 1s spectra of glycine, glycyl-glycine, and glycyl-glycyl-glycine. *The Journal of Physical Chemistry A* **107,** 6144–6159 (2003).

226. Feyer, V. *et al.* Photoemission and photoabsorption spectroscopy of glycyl-glycine in the gas phase. *The Journal of Physical Chemistry A* **113,** 10726–10733 (2009).

227. Schwartz, C. P., Saykally, R. J. & Prendergast, D. An analysis of the NEXAFS spectra of a molecular crystal: α-glycine. *The Journal of Chemical Physics* **133,** 044507 (2010).

228. Buckley, M. W. & Besley, N. A. A theoretical study of the near edge X-ray absorption fine structure of amino acids and proteins. *Chemical Physics Letters* **501,** 540–546 (2011).

229. Yang, L., Plashkevych, O., Vahtras, O., Carravetta, V. & Ågren, H. Near edge X-ray absorption and dichroism in amino acids. *Journal of Synchrotron Radiation* **6,** 708–710 (1999).

230. Jiemchooroj, A., Ekström, U. & Norman, P. Near-edge X-ray absorption and natural circular dichroism spectra of L-alanine: A theoretical study based on the complex polarization propagator approach. *The Journal of Chemical Physics* **127,** 165104 (2007).

231. Kimberg, V. & Kosugi, N. Calculation of K-edge circular dichroism of amino acids: Comparison of random phase approximation with other methods. *The Journal of Chemical Physics* **126,** 245101 (2007).

232. Villaume, S. & Norman, P. On circular dichroism and the separation between chromophore and chiral center: The near carbon K-edge X-ray absorption and circular dichroism spectra of noradrenaline and L-DOPA. *Chirality* **21,** E13–E19 (2009).

233. Takahashi, O., Kimoto, M. & Pettersson, L. G. Theoretical study of the X-ray natural circular dichroism of some crystalline amino acids. *Chemical Physics* **450-451,** 109–114 (2015).

234. Grasjo, J. *et al.* Local Electronic Structure of Functional Groups in Glycine As Anion, Zwitterion, and Cation in Aqueous Solution. *The Journal of Physical Chemistry B* **113,** 16002–16006 (2009).

235. Blum, M. *et al.* Ultrafast Proton Dynamics in Aqueous Amino Acid Solutions Studied by Resonant Inelastic Soft X-ray Scattering. *The Journal of Physical Chemistry B* **116,** 13757–13764 (2012).

236. Meyer, F. *et al.* Building Block Picture of the Electronic Structure of Aqueous Cysteine Derived from Resonant Inelastic Soft X-ray Scattering. *The Journal of Physical Chemistry B* **118,** 13142–13150 (2014).

237. Meyer, F. *et al.* Non-equivalent carbon atoms in the resonant inelastic soft X-ray scattering map of cysteine. *The Journal of Chemical Physics* **138,** 034306 (2013).

238. Meyer, F. *et al.* X-ray Emission Spectroscopy of Proteinogenic Amino Acids at All Relevant Absorption Edges. *The Journal of Physical Chemistry B* **121,** 6549–6556 (2017).

239. Weinhardt, L. *et al.* Local electronic structure of the peptide bond probed by resonant inelastic soft X-ray scattering. *Physical Chemistry Chemical Physics* **21,** 13207–13214 (2019).

240. Nilsson, A. *et al.* Probing chemical bonding in adsorbates using X-ray emission spectroscopy. *Journal of Electron Spectroscopy and Related Phenomena* **110-111,** 15–39 (2000).

241. Lee, N., Petrenko, T., Bergmann, U., Neese, F. & DeBeer, S. Probing valence orbital composition with iron Kβ X-ray emission spectroscopy. *Journal of the American Chemical Society* **132,** 9715–9727 (2010).

242. Hanson-Heine, M. W. D., George, M. W. & Besley, N. A. Kohn-Sham density functional theory calculations of non-resonant and resonant X-ray emission spectroscopy. *The Journal of Chemical Physics* **146,** 094106 (2017).

243. Hanson-Heine, M. W., George, M. W. & Besley, N. A. Density functional theory calculations of the non-resonant and resonant X-ray emis-

sion spectroscopy of carbon fullerenes and nanotubes. *Chemical Physics Letters* **696,** 119–124 (2018).

244. Ljungberg, M. P., Nilsson, A. & Pettersson, L. G. M. Semiclassical description of nuclear dynamics in X-ray emission of water. *Physical Review B* **82,** 245115 (24 2010).

245. Ljungberg, M. P., Zhovtobriukh, I., Takahashi, O. & Pettersson, L. G. M. Core-hole-induced dynamical effects in the X-ray emission spectrum of liquid methanol. *The Journal of Chemical Physics* **146,** 134506 (2017).

246. Takahashi, O., Ljungberg, M. P. & Pettersson, L. G. M. X-ray Emission Spectrum of Liquid Ethanol: Origin of Split Peaks. *The Journal of Physical Chemistry B* **121,** 11163–11168 (2017).

247. Faber, R. & Coriani, S. Resonant Inelastic X-ray Scattering and Nonesonant X-ray Emission Spectra from Coupled-Cluster (Damped) Response Theory. *Journal of Chemical Theory and Computation* **15,** 520–528 (2019).

248. Wadey, J. D. & Besley, N. A. Quantum chemical calculations of X-ray emission spectroscopy. *Journal of Chemical Theory and Computation* **10,** 4557–4564 (2014).

249. Zhang, Y., Mukamel, S., Khalil, M. & Govind, N. Simulating valence-to-core X-ray emission spectroscopy of transition metal complexes with time-dependent density functional theory. *Journal of Chemical Theory and Computation* **11,** 5804–5809 (2015).

250. Roper, I. P. & Besley, N. A. The effect of basis set and exchange-correlation functional on time-dependent density functional theory calculations within the Tamm-Dancoff approxi mation of the X-ray emission spectroscopy of transition metal complexes. *The Journal of Chemical Physics* **144,** 114104 (2016).

251. Mortensen, D. R. *et al.* Benchmark Results and Theoretical Treatments for Valence-to-Core X-ray Emission Spectroscopy in Transition Metal Compounds. *Physical Review B* **96,** 125136 (12 2017).

252. Clarke, C. J. *et al.* Zinc 1s valence-to-core X-ray emission spectroscopy of halozincate complexes. *The Journal of Physical Chemistry A* **123,** 9552–9559 (2019).

253. Fouda, A. E. A., Purnell, G. I. & Besley, N. A. Simulation of ultrafast dynamics effects in resonant inelastic X-ray scattering of gas-phase water. *Journal of Chemical Theory and Computation* **14,** 2586–2595 (2018).

254. Fransson, T. & Dreuw, A. Simulating X-ray emission spectroscopy with algebraic diagrammatic construction schemes for the polarization propagator. *Journal of Chemical Theory and Computation* **15,** 546–556 (2019).

255. Besley, N. A. Equation of motion coupled cluster theory calculations of the X-ray emission spectroscopy of water. *Chemical Physics Letters* **542,** 42–46 (2012).

256. Fouda, A. E. A. & Besley, N. A. Assessment of basis sets for density functional theory-based calculations of core-electron spectroscopies. *Theoretical Chemistry Accounts* **137,** 6 (2017).

257. Hanson-Heine, M. W., George, M. W. & Besley, N. A. Basis sets for the calculation of core-electron binding energies. *Chemical Physics Letters* **699,** 279–285 (2018).

258. Stephens, P. J., Devlin, F. J., Chabalowski, C. F. & Frisch, M. J. Ab Initio Calculation of Vibrational Absorption and Circular Dichroism Spectra Using Density Functional Force Fields. *The Journal of Physical Chemistry A* **98,** 11623–11627 (1994).

259. Tomasi, J., Mennucci, B. & Cammi, R. Quantum Mechanical Continuum Solvation Models. *Chemical Reviews* **105,** 2999–3094 (2005).

260. Lindgren, A. *et al.* Molecular alignment of ammonia studied by electron-ion-ion coincidence spectroscopy. *The Journal of Chemical Physics* **122,** 114306 (2005).

261. Fouda, A. E. A. & Besley, N. A. Improving the predictive quality of time-dependent density functional theory calculations of the X-ray emission spectroscopy of organic molecules. *Journal of Computational Chemistry* **41,** 1081–1090 (2020).